GAS MIGRATION THROUGH CRYSTAL-RICH MAFIC VOLCANIC SYSTEMS AND APPLICATION TO STROMBOLI VOLCANO, AEOLIAN ISLANDS, ITALY

by

ISOLDE LEO MARIA BEATRIJS BELIEN

A DISSERTATION

Presented to the Department of Geological Sciences
and the Graduate School of the University of Oregon
in partial fulfillment of the requirements
for the degree of
Doctor of Philosophy

September 2011

DISSERTATION APPROVAL PAGE

Student: Isolde L.M.B. Belien

Title: Gas Migration Through Crystal-Rich Mafic Volcanic Systems and Application to Stromboli Volcano, Aeolian Islands, Italy

This dissertation has been accepted and approved in partial fulfillment of the requirements for the Doctor of Philosophy degree in the Department of Geological Sciences by:

Katharine Cashman	Chairperson
Alan Rempel	Member
Mark Reed	Member
Raghuveer Parthasarathy	Outside Member

and

Kimberly Andrews Espy	Vice President for Research & Innovation/Dean of the Graduate School

Original approval signatures are on file with the University of Oregon Graduate School.

Degree awarded September 2011

DISSERTATION ABSTRACT

Isolde L.M.B. Belien

Doctor of Philosophy

Department of Geological Sciences

September 2011

Title: Gas Migration Through Crystal-Rich Mafic Volcanic Systems and Application to Stromboli Volcano, Aeolian Islands, Italy

Approved: _____
Katharine Cashman

Crystals influence the migration of gas through magma. At low concentrations, they increase the bulk fluid properties, especially viscosity. At concentrations close to maximum packing, crystals form a rigid framework and magma cannot erupt. However, erupted pyroclasts with crystal contents close to the packing concentration are common at mafic volcanoes that exhibit Strombolian behavior. In this dissertation, I study the influence of solid particles on gas migration. I apply my results to Stromboli volcano, Italy, type locality of the normal Strombolian eruptive style, where gas moves through an essentially stagnant magma with crystallinity ~50%. Specifically, I investigate the effect of crystals on flow regime, gas content (Chapter II), bubble concentration (number densities), bubble shapes, bubble sizes (Chapter III), and bubble rise velocities (gas flux) (Chapter IV). I find that gas-liquid flow regimes are not applicable at high particle concentrations and should be replaced by new, three-phase (gas-liquid-solid) regimes and that degassing efficiency increases with particle concentration (Chapter II). In Chapter III, I show that crystals modify bubble populations by trapping small bubbles and causing large

bubbles to split into smaller ones and by modifying bubble shapes. In Chapter IV, I model Stromboli's crystal-rich magma as a network of capillary tubes and show that bubble rise velocities are significantly slower than free rise velocities in the absence of particles. In each chapter, I use analogue experiments to study the effect of different liquid and solid properties on gas migration in viscous liquids. I then apply my analogue results to magmatic conditions using simple parameterizations and/or numerical modeling or by comparing the results directly to observations made on crystal-rich volcanic rocks. Chapter V proposes a mechanism for Strombolian eruptions and gas migration through the crystal-rich magma in which the effect of crystals is included. This model replaces the current two-phase "slug" model, which cannot account for the high crystallinity observed at Stromboli. There are three appendices in this dissertation: a preliminary study of the influence of particles on gas expansion, image analysis methods, and the numerical code developed in Chapter IV.

This dissertation includes previously published and unpublished co-authored material.

CURRICULUM VITAE

NAME OF AUTHOR: Isolde L.M.B. Belien

GRADUATE AND UNDERGRADUATE SCHOOLS ATTENDED:

University of Oregon, Eugene
Ghent University, Belgium

DEGREES AWARDED:

Doctor of Philosophy, Geological Sciences, 2011, University of Oregon
Licentiaat, Geology, 2006, Ghent University

AREAS OF SPECIAL INTEREST:

Volcanology
Fluid Dynamics

PROFESSIONAL EXPERIENCE:

Student intern, ExxonMobil Upstream Research Company,
June 2010-September 2010

GRANTS, AWARDS, AND HONORS:

Good Citizen Award, Geology, University of Oregon, 2009

Student Research Grant, GSA, 2009

Staples Fellowship, Geology, University of Oregon, 2008

Kleinman Grant for Volcano Research, USGS, 2008 (shared)

Thayer Scholarship, Geology, University of Oregon, 2007

Fellow, Francqui Foundation, 2006

Fellow, Belgian American Educational Foundation (BAEF), 2006

Joint Francqui and BAEF scholarship for study in the United States, 2006-2007

Valère Billiet Prize for outstanding Geology graduate, Ghent University, 2006

PUBLICATIONS:

Belien, I.B., Cashman, K.V. and Rempel, A.W. (2010). Gas accumulation in particle-rich suspensions and implications for bubble populations in crystal-rich magma. Earth and Planetary Science Letters 297, 133-140.

To my family

TABLE OF CONTENTS

Chapter Page

I. INTRODUCTION 1

1. Introduction to Stromboli Volcano 4

2. Dissertation Overview 6

II. THE EFFECT OF SOLID PARTICLES ON FLOW REGIME AND IMPLICATIONS FOR DEGASSING AT CRYSTAL-RICH MAFIC VOLCANOES 11

1. Introduction 11

2. Background 13

2.1. Two-Phase Flow Regimes in Volcanology 14

2.2. The Normal Strombolian Eruption Mechanism 17

3. Methods 18

4. Experimental Results 20

4.1. The Effect of Viscosity on Flow Regime 21

4.2. The Effect of Particles on Flow Regime 25

5. Application to Volcanic Systems 31

6. Conclusions 37

7. Bridge 38

III. GAS ACCUMULATION IN PARTICLE-RICH SUSPENSIONS AND IMPLICATIONS FOR BUBBLE POPULATIONS IN CRYSTAL-RICH MAGMA 39

1. Introduction 39

2. Experiments and Observations 41

2.1. Individual Bubbles 42

Chapter Page

2.2. Splitting Probabilities 46

2.3. Bubble Populations 48

2.4. Summary of Experimental Observations 50

3. Bubble Populations in Tephra from Stromboli 53

4. Comparison of Experimental and Volcanic Conditions 58

5. The Role of Gas in Strombolian Eruptions 61

5.1. Gas Migration Through Magma 61

5.2. Bubble Populations as a Proxy for Gas Flux 63

6. Conclusions 66

7. Bridge 67

IV. THE RISE SPEED OF A BUBBLE THROUGH A VISCOUS LIQUID IN A NARROW TUBE AND APPLICATION TO BUBBLE PERCOLATION THROUGH CRYSTAL-RICH MAGMA AT STROMBOLI 69

1. Introduction 69

2. Background 72

3. Experimental Methods 76

4. Experimental Results 80

4.1. Partially Submerged Tubes 80

4.2. Fully Submerged Tubes 86

4.3. Comparison with Porous Media 91

5. Predicting Bubble Velocities in Fully Submerged Tubes 93

5.1. Theory 94

5.2. An Empirical Prediction 99

Chapter Page

6. A Numerical Model for Bubble Percolation Through Porous Media 102

6.1. Model Geometry 103

7. Application to Bubble Percolation at Stromboli Volcano 105

7.1. Modeling Parameters 105

7.2. Model Results 109

7.3. Implications for Stromboli's Shallow Plumbing System 112

8. Conclusions 114

9. Bridge 115

V. SUMMARY: A NEW MODEL FOR GAS MIGRATION AT STROMBOLI VOLCANO AND THE NORMAL STROMBOLIAN ERUPTION MECHANISM 117

1. A New Model for Normal Strombolian Eruptions 117

2. Gas Accumulation Rates 121

3. Eruptive Intensity 123

4. Conclusions 126

VI. CONCLUSIONS 129

APPENDICES 133

A. PRELIMINARY EXPERIMENTS ON THE INFLUENCE OF PARTICLES ON GAS EXPANSION IN A VISCOUS LIQUID 133

1. Motivation 133

2. Methods 135

3. Experimental Results 140

4. Future Work 143

Chapter Page

B. IMAGE ANALYSIS TECHNIQUES..... 145

1. Bubble and Crystal Size Distributions..... 146

2. Crystal Spacing..... 147

3. MATLAB® Code 150

C. MATLAB® MODEL FOR BUBBLE RISE THROUGH POROUS MEDIA 157

REFERENCES CITED 161

LIST OF FIGURES

Figure		Page
1.1.	Map of Stromboli volcano, Italy	5
1.2.	Pictures illustrating normal Strombolian activity at Stromboli volcano	7
2.1.	Flow regimes in a vertical pipe	14
2.2.	Two phase interpretations of the mafic eruption styles	16
2.3.	Experimental setup	19
2.4.	Flow regimes observed in our experiments	21
2.5.	Flow regimes in two-phase systems with different viscosities in a vertical tube	22
2.6.	Flow regimes in water (bottom panel) and light Karo corn syrup (top panel) at different particle concentrations and air flow rates	29
2.7.	Gas content expressed as % of liquid entrained in the liquid (+ particle) column at each flow rate, at varying particle concentrations in water	30
2.8.	A thin section image from crystal-rich tephra erupted at Stromboli	33
2.9.	Simple two-phase and three-phase models for flow regimes occurring in a volcanic conduit	34
2.10.	Crystal-free vesicularity as a function of crystallinity for representative areas of thin section scans from crystal-rich tephra erupted at Stromboli	36
3.1.	Schematic of setups used to study a) styles of interaction between a single bubble and particles in suspension, b) occurrence frequency of different interaction styles between a single bubble and a single particle, and c) the effect of a particle suspension on bubble size distributions	43
3.2.	Styles of interaction between a bubble and particles suspended in a viscous fluid	45
3.3.	Occurrence frequencies of interaction styles between a single particle and a single bubble injected directly underneath for different particle orientations	47

Figure Page

3.4. Evolution of bubble size distribution through time in a particle suspension fluxed through with 0.1 ml bubbles (equivalent diameter 5.8 mm; ψ=0.8) ... 49

3.5. Steady-state size distributions of bubbles inside a particle suspension resulting from through-flux of bubbles of a single size ... 51

3.6. Experimentally measured bubble rise velocity versus bubble size ... 53

3.7. Bubble and crystal size distributions (normalized to total area of melt+crystals+bubbles) in a thin section scan (a) and on 39x magnification SEM images from the same thin section (b) ... 55

3.8. SEM (scanning electron microscope) images of tephra from Stromboli volcano ... 57

3.9. SEM (scanning electron microscope) images of tephra from Stromboli volcano ... 57

4.1. Experimental setup used to measure bubble rise velocities in a partially submerged tube (A) and a fully submerged tube (B) ... 77

4.2. Typical examples of (A) a sub-spherical bubble with $R_{eq}/R < 1$, (B) a transitional bubble with $1 < R_{eq}/R < 1.5$ and (C) a Taylor bubble with $R_{eq}/R > 1.5$ ... 78

4.3. Distortion of a 0.5 mm diameter cylindrical rod in a tube with 2/8 inch internal diameter due to light refraction in Karo syrup (left) and glycerin (right) ... 79

4.4. Top: experimental bubble velocities in partially submerged tubes in light Karo corn syrup as a function of bubble equivalent radius / tube radius. Bottom: values for the 2/8 inch tube on a larger scale ... 83

4.5. Variation of measured dimensionless film thickness x with bubble size relative to tube size in partially submerged tubes of different width in corn syrup ... 84

4.6. Comparison of measured bubble rise velocities in partially submerged tubes in Karo syrup with literature predictions for bubbles in sealed tubes ... 86

4.7. Top: experimental bubble velocities in vertical tubes fully submerged in light Karo corn syrup versus R_{eq}/R. Bottom: bubble velocities normalized to the Stokes free rise velocity for viscous liquids in absence of a tube ... 89

Figure Page

4.8. Dimensionless film thickness x as a function of normalized bubble size for bubbles rising in fully submerged tubes with different widths in light Karo corn syrup 91

4.9. Comparison of measured bubble velocities in Karo syrup in fully and partially submerged tubes to velocities measured in a suspension of plastic particles in corn syrup 93

4.10. Simplified schematic of a bubble rising in a fully submerged tube showing parameters and notation used in the derivation of the equation for bubble rise velocity 95

4.11. Variation in bubble rise velocity in a fully submerged tube with position of the bubble in the tube 97

4.12. Comparison of experimental bubble velocities in light Karo syrup in fully submerged tubes with predictions 98

4.13. Measured velocities in fully submerged tubes in Karo syrup and glycerin normalized to the corresponding velocity in a sealed tube 102

4.14. Distributions of (left to right) crystal long axis lengths (tube lengths), bubble area equivalent radii (bubble radii), and half of the intercrystal distances (pore radii) at Stromboli volcano 107

4.15. Bubbles (light gray) and crystals (dark gray) in two of the thin section images from crystal-rich tephra from Stromboli volcano 108

4.16. Comparison of Stokes free rise velocities and velocities through Stromboli's crystal-rich magma obtained from our model for the range of bubble sizes observed in thin sections 110

4.17. Distribution of modeled average gas velocities through Stromboli's upper magma in 100 model runs, in the presence of crystals (left) and assuming no crystals are present (right, only Stokes rise) 112

5.1. The increase of total crystallinity and plagioclase content with decreasing pressure (decreasing depth below the free magma surface) in the magma at Stromboli 120

5.2. Schematic showing gas accumulation and pressure buildup underneath a crystalline plug as a mechanism for Strombolian eruptions 121

Figure Page

5.3. Bubble number density and vesicularity in tephra samples from normal and major Strombolian erupions 125

5.4. Summary schematic comparing the slug model and the plug model for the normal Strombolian eruption mechanism..... 128

A.1. Schematic (left) and photo (right) of the experimental setup 136

A.2. Most of our experiments follow a straight line on a plot of V_{total} versus $P_{initial}/P$. Examples are shown for experiments 1 and 40 139

A.3. $PV_{gas}/P_{initial}V_{gas,initial}$ versus time for three experiments showing constant amount of gas, gas loss and gas gain..... 141

A.4. Variation of $PV_{gas}/ P_{initial}V_{gas,initial}$ at the end of the experiments in Table A.1 with pressure drop, initial vesicularity, and initial crystallinity 142

B.1. Extracting bubble and crystal populations from a thin section scan 146

B.2. Figure illustrating how crystal spacings are extracted..... 149

LIST OF TABLES

Table		Page
2.1.	Fluid properties of the liquids used in this study	19
3.1.	Properties of materials used in this study compared to natural systems	44
3.2.	Comparison of dimensionless parameters for our analogue system and Stromboli magma	60
4.1.	Bubble rise velocities in partially submerged narrow tubes in light Karo corn syrup	81
4.2.	Measurements of film thickness expressed as a fraction x of the tube radius in Karo syrup in partially submerged tubes	82
4.3.	Bubble rise velocities in fully submerged narrow tubes in light Karo corn syrup	88
4.4.	Measurements of film thickness expressed as a fraction x of the tube radius in light Karo corn syrup in fully submerged tubes	90
4.5.	Fluid properties for Stromboli magma used in our numerical model	105
A.1.	Summary of experimental conditions	137

CHAPTER I

INTRODUCTION

An important factor controlling the explosivity of volcanic eruptions is the ease of gas escape from the magma (Sparks, 2003; Edmonds, 2008). At high pressures (large depths) within the earth, volatile species such as H_2O and CO_2 are dissolved in the molten rock that is magma. As magma rises and pressure decreases, these volatiles come out of solution and form gas bubbles (Wallace and Anderson, 2000). Exsolution and gas expansion progress as pressure continues to decrease. If the magma viscosity is low, bubbles will form to balance the change in volatile solubility caused by the pressure decrease. In such systems eruptions are typically mild, giving rise to small explosions or lava flows. If the magma has a high viscosity or if its rise speed is too fast to allow equilibration, bubble nucleation is delayed and growth is impeded to an extent that overpressure will build up inside the gas bubbles, leading to more violent eruptions.

In addition to bubble formation, crystallization also occurs as the magma rises and cools, and as volatile exsolution causes the melt composition to change. Crystals are typically assumed to influence the bulk fluid properties, especially the bulk viscosity of the magma. Multiple equations exist in the literature to calculate the viscosity increase caused by an increase in crystallinity (e.g. Roscoe, 1952; Krieger and Dougherty, 1959; Ji, 2004; Costa, 2005). Direct measurements of the bulk viscosity on natural and synthetic magmas are also abundant (e.g. Lejeune and Richet, 1995; Caricchi et al., 2007; Ishibashi and Sato, 2007; Champallier et al., 2008; Vetere et al. 2010; Vona et al., 2011). In these studies, the melt + crystal suspension is treated as a single fluid with bulk fluid properties

instead of the properties of the pure melt. When crystals are present in such abundance that the maximum packing concentration is reached, the magma should become rheologically locked (Marsh, 1981). Marsh (1981) suggested that magmas with crystal concentrations above this threshold are uneruptible and will cool at depth to form a pluton, although nearly holocrystalline (mostly silicic) magmas do extrude as lava domes or spines (e.g. the 2004-2008 spine extrusions at Mt. St. Helens, Mastin et al., 2008). At any rate, magmas at high crystal concentrations develop a yield strength (e.g. Caricchi et al., 2007), which is a threshold value of stress below which deformation is not permanent and flow cannot occur. The yield strength can be thought of as the stress below which the magma viscosity is infinite, so that gas migration in such systems should be significantly impeded. The critical crystal concentration at which magma rheology changes from approximately Newtonian to non-Newtonian (with an appreciable yield strength) has been estimated around or above 40-60% by volume (Lejeune and Richet, 1995; Caricchi et al., 2007).

Volcanic clasts with crystallinities close to the critical concentration are erupted at several low-viscosity (mafic) volcanoes exhibiting a mildly explosive eruptive style called “normal Strombolian” (e.g. Stromboli, Etna (Polacci et al., 2006b) and Villarrica (Gurioli et al., 2008)). At Stromboli volcano, Italy, the type locality for this eruptive style, extensive and continuous passive degassing occurs from a magma with 45-55 vol.% crystals (Métrich et al., 2001; Landi et al., 2004), implying that gas must somehow percolate through the crystal-rich magma without building up the overpressure that would be expected if the crystals simply increased the bulk viscosity of the system. Large amounts of gas are also released with only minor magma expulsion during the normal

Strombolian eruptions themselves. The current model for the normal Strombolian eruption mechanism, which originated with Blackburn et al. (1976), is based on the rise and coalescence of bubbles in the volcanic conduit and does not take the effect of crystals into account. In this model, bubbles coalesce to form a conduit-filling gas bubble ("slug"), the bursting of which at the free magma surface produces the Strombolian explosion. Several questions arise:

- How do crystals influence gas migration in low-viscosity magmas, where gas can rise independently through the melt? What is the significance of the critical crystal concentration with respect to rising gas bubbles? What fluid properties do the bubbles "feel" as they percolate through the crystal-rich system?
- What are the physical mechanisms of gas percolation through the crystal-rich magma at Stromboli? What is the effect of crystals on the degassing efficiency?
- What is the effect of crystals on bubble populations? Do crystals aid or inhibit coalescence?
- How do crystals in high concentrations influence the eruptive style? How does this relate to the current model for the normal Strombolian eruption mechanism? How would large gas slugs migrate through a magma with ~50 vol.% crystals?

In this dissertation, I address these questions to study the effect of crystals on gas migration in low-viscosity magmas. I focus my work on Stromboli volcano, Italy, the

type locality for the normal Strombolian eruptive style. I first provide a brief overview of the activity at Stromboli before summarizing the work presented in this dissertation.

1. Introduction to Stromboli volcano

Stromboli volcano is part of the Aeolian Archipelago in the Tyrrhenian Sea off the north coast of Sicily, Italy (Figure 1.1.). Activity is focused at three vent areas (SW, central and NE) in the crater terrace. The vents are connected, as activity shifts freely from one to the other (e.g. Harris and Ripepe, 2007) so that the shallow plumbing system must span at least the entire crater terrace area. Petrological data show that two types of magma reside in Stromboli's plumbing system. Both have similar, high-potassium/ shoshonitic basaltic bulk compositions but differ strongly in crystal content (Francalanci et al., 1999; Métrich et al., 2001; Bertagnini et al., 2008). In the upper part of the plumbing system, a high-porphyritic (HP) magma, with 45-55 vol.% phenocrysts (e.g. Métrich et al., 2001; Landi et al., 2004), overlies a crystal-poor, low-porphyritic magma with < 10 vol.% crystals (e.g. Métrich et al., 2001).

Volcanic activity at Stromboli is dominated by gas, with only 10% of total gas expelled accompanied by eruption of volcanic rocks (Harris and Ripepe, 2007). This indicates that gas moves independently through the crystal-rich system, making this volcano an ideal case study for research on the physical processes that control gas migration through volcanic systems. Normal Strombolian activity consists mainly of intermittent mildly explosive eruptions that occur at regular intervals and are accompanied by extensive degassing. The eruptions consist of small eruption columns

that eject tephra and ash to heights of a few 100 m and recur every ~15 minutes (Figure 1.2.). Volcanic clasts (tephra) erupted during normal Strombolian activity consist mainly of HP magma, although small amounts of LP magma are erupted as well (D'Oriano et al., 2010). LP magma is mostly erupted as golden pumice during larger "paroxysmal" eruptions, which occur less frequently and find their source in the deeper plumbing system (e.g. Métrich et al., 2001, Bertagnini et al., 2003; Armienti et al., 2007). We are not concerned with these paroxysms in the present work.

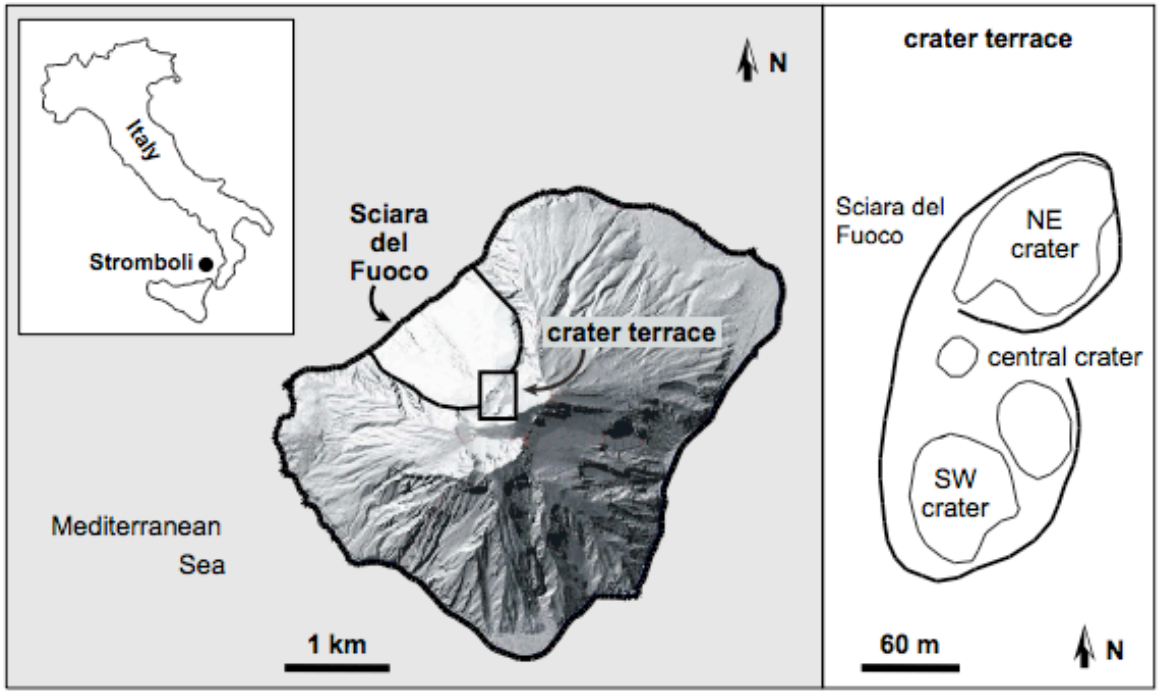

Figure 1.1. Map of Stromboli volcano, Italy, with shaded relief adapted from Fornaciai et al. (2010). The crater terrace and a prominent sector collapse (the Sciara del Fuoco) are marked. The configuration of the crater terrace in June 1999 is shown, after Ripepe et al. (2002).

Although normal Strombolian eruptions are dominated by gas, 90% of the degassing at Stromboli occurs independently of these eruptions through active (45%) and passive degassing (45%) (Harris and Ripepe, 2007). Active degassing, or "puffing", consists of overpressurized gas bursts occurring every ~2 s, mainly from the central vent, without significant magma ejection, and is attributed to bubby gas flow in the conduit (Ripepe et al., 2002; Ripepe et al., 2007), with gas bursting as small slugs (conduit-filling bubbles) at the surface (Harris and Ripepe, 2007). In contrast, normal Strombolian eruptions are attributed to the rise of large gas slugs from depth, which expel clots of magma as they burst (e.g. Vergniolle and Mangan, 2000). The conceptual models for both puffing activity and Strombolian eruptions are based on engineering models of gas-liquid flow in pipes. These models consist only of two phases: the gas bubble(s) and the bulk liquid + crystal phase, and do not explicitly include the effect of the crystals.

2. Dissertation overview

In the four body chapters of this dissertation I explore the influence of solid particles on various aspects of gas migration through magma. First, in Chapter II, I explore the effect of increasing particle concentration on flow regime and gas holdup. I show that the traditional two-phase gas-liquid flow regimes no longer exist once the particle concentration reaches a threshold at which the particles are so close together that they hinder each other's movement. The effect of particle concentration below the threshold is similar to that of increasing fluid viscosity and density.

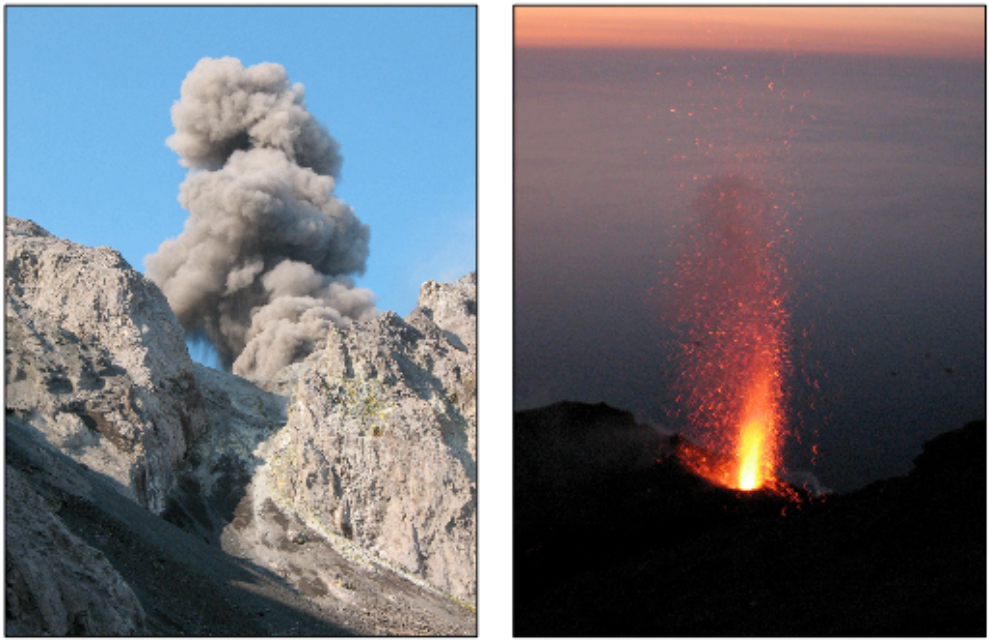

Figure 1.2. Pictures illustrating normal Strombolian activity at Stromboli volcano. Left: an ash-rich eruptive plume from a large Strombolian explosion rising above the Sciara del Fuoco rim. Right: a typical Strombolian shower of incandescent magma expelled when overpressurized gas is released at the vent.

Above the threshold, two-phase flow regimes are increasingly modified by the presence of the crystals, until, at the "packing concentration" of the particles (where the particles form a touching framework), different, three-phase flow regimes occur. This shows that two-phase models are not adequate to explain gas-driven eruptive activity in systems such as Stromboli, where crystals approach the critical concentration. A new model, replacing the current two-phase slug model, will have to account for the effect of the crystals. I also show that gas holdup, a measure of the gas volume entrained in the system, decreases with particle concentration at constant flow rate, implying that degassing efficiency increases, and more crystal-rich volcanic rock samples should have lower vesicularities. I use image analysis on thin sections from crystal-rich tephra erupted

at Stromboli to test this hypothesis, and discuss implications for eruptive activity at Stromboli, where bubble number densities in tephra have been linked to eruptive intensity (Colò et al., 2010).

In Chapter III, I investigate the influence of particles on bubble shapes and sizes, and show that bubble size distributions become skewed towards bubbles smaller than the crystal size because larger bubbles can split around particles while small bubbles are trapped beneath the particles, thereby becoming enriched in the particle suspension. This study shows that caution is required when using bubble size distributions in crystal-rich tephra to extract information on degassing history and timing of bubble nucleation, as is done for crystal-poor systems (e.g. Toramaru, 1989 and 1990; Blower et al., 2001) and for lava flows (Cashman et al., 1994; Cashman and Kauahikaua, 1997). The crystals play a complicated role in modifying bubble populations, which deserves further investigation. I also show that bubble populations in tephra may be modified to a large extent by syn-eruptive expansion of the volatiles, highlighting the need to correct for this effect before using bubble populations in tephra as proxies for pre-eruptive populations in any system, crystal rich or crystal poor.

In Chapter IV, I draw an analogy with sedimentary systems (petroleum reservoirs and aquifers), and treat crystal-rich basaltic systems as porous media, where gas moves through a liquid (magma) in a rigid network of solid particles (crystals). Following reservoir modeling studies, I model the porous medium as a network of capillary tubes through which the bubbles rise. I show, however, that the theory usually used in these situations, which describes bubble rise in a capillary sealed at one end (e.g. Viana et al., 2003, and references therein), is not a good descriptor of bubble rise through porous

media. I replace this model with a situation where the tube is open on both ends, allowing return flow of the liquid from the top to the base around the outside of the tube. This finding has implications for studies of bubble rise in any porous medium, not limited to volcanic systems. I use bubble rise velocities in such open tubes to model gas flux at Stromboli volcano. I combine this model with field measurements of the passive degassing flux at Stromboli and show that the gas flux is dominated by bubbles larger than the dominant bubble size observed in tephra. This confirms the result from Chapter III that observed bubble populations are skewed towards smaller sizes. I also show that rise velocities of small bubbles through Stromboli's crystal-rich magma are orders of magnitude lower than their free rise velocities in the absence of crystals. Taking the latter as the rise velocities through the deeper, crystal-poor magma, this implies that gas likely accumulates at the interface between the two magma bodies.

In Chapter V, I combine the key findings from the previous chapters to formulate a new model for gas migration through crystal-rich magma and the Strombolian eruption mechanism. I interpret petrological and geophysical measurements made at Stromboli in light of this new model and show that these data are equally well or better explained by the new model than by the two-phase slug model.

In addition to the four body chapters, this dissertation has three appendices. Appendix A contains preliminary results for a work in progress, in which I investigate the influence of crystal-inhibited bubble expansion, rather than pure bubble rise, on gas escape. Appendix B contains detailed information on image analysis techniques used to obtain the characteristics of bubble and crystal populations in Stromboli tephra in this

dissertation. Appendix C contains the numerical code used to model bubble rise velocities through Stromboli's crystal-rich magma in Chapter IV.

All chapters in this dissertation are co-authored by my advisor Dr. Katharine Cashman, who provided guidance for all the work contained in this dissertation. Chapters III and IV are co-authored by committee member Dr. Alan Rempel, also in an advising role. Tina Wilson (work-study student at the University of Oregon) did part of the experiments in Chapter II. Dr. Jenny Suckale (previously at MIT, now at Harvard) did the stress-strain modeling in Chapter V. The preliminary work described in Appendix A is co-authored by Drs. Alison Rust and Jeremy Phillips at the University of Bristol (UK), who provided guidance for it. I would like to acknowledge Marco Pistolesi (University of Pisa, Italy) and Livia Colò (University of Florence, Italy) for sending me tephra samples and for helpful discussions. Chapter III is published, with reference: Belien IB, Cashman KV and Rempel AW (2010). Gas accumulation in particle-rich suspensions and implications for bubble populations in crystal-rich magma. Earth and Planetary Science Letters 297, 133-140. Chapters II and IV are being prepared for submission.

CHAPTER II

THE EFFECT OF SOLID PARTICLES ON FLOW REGIME AND IMPLICATIONS FOR DEGASSING AT CRYSTAL-RICH MAFIC VOLCANOES

Part of the flow regime experiments for this work were done by work-study student Tina Wilson at the University of Oregon under my guidance. The initial 12 sets of experiments on flow regimes as well as all the data analysis and interpretation were done by me. Dr. Katharine Cashman was the advisor on this project.

1. Introduction

Strombolian explosions are a common form of activity in small mafic volcanic systems. They are attributed to a conduit-filling gas bubble that rises and bursts at the free magma surface, expelling magma as it bursts. This flow regime, called slug flow, has been identified for two-phase systems in which gas flows through a liquid. However, at many volcanoes that exhibit the Strombolian eruption style, the crystallinity of the magma can be quite large (~50% at Stromboli volcano), which raises questions about the relevance of two-phase flow models.

It is generally assumed that the primary effect of adding particles to a fluid is to increase the bulk viscosity and density, so that the particles and liquid can still be treated as a single fluid phase, but with different properties than the pure liquid. Theoretical corrections are abundant in the literature (e.g. Roscoe, 1952; Krieger and Dougherty, 1959; Ji, 2004; Costa, 2005), and depend on particle shape and size distribution. At high

crystal concentrations, however, porous media flow has been proposed to occur (Costa et al., 2006; Walsh and Saar, 2008) and the two-phase gas-liquid approach to gas migration through magmas might be insufficient. The effects of crystals in high concentrations on flow regime and on the mechanism of gas migration in general are not known. Towards this end we have performed a set of analogue experiments in which air rises at different flow rates through a cylindrical tube filled with a mixture of corn syrup (magma) and various proportions of solid particles (crystals). We compare the results to experiments in which we use a water-particle mixture to explore the effect of viscosity on flow regime. We keep track of the flow regimes that occur at each air flow rate and particle concentration, and measure the height of the liquid-particle mixture to determine the amount of gas that is contained within the system in each experiment. We observe that low particle concentrations do, indeed, have the same effect on flow regimes as a change in liquid viscosity and density, justifying the concept that the presence of particles in low concentrations can be modeled by modifying the bulk fluid properties. At particle contents near the concentration at which the particles start to touch, however, particles have a large influence on gas migration, and the two-phase gas-liquid flow regimes are replaced by new, three-phase regimes. This has important implications for the interpretation of eruption mechanisms at volcanic systems such as Stromboli, where the crystal concentration approaches the theoretical concentration at which the particles are fully interlocking (maximum packing concentration as identified by Marsh, 1981). We find that another effect of increasing particle concentration is to decrease the gas holdup (i.e. the volume of gas entrained in the liquid). This is verified for crystal-rich tephra samples from Stromboli, in which we find an inverse relationship between vesicularity

and crystallinity. This finding may contribute to our understanding of the mechanism of normal activity at Stromboli, where Colò et al. (2010) found an inverse relationship between bubble number density and intensity of the eruptions.

2. Background

Gas-liquid flow regimes occur in a number of industrial situations and have been studied extensively with application to fluid transport in pipelines in the petroleum industry (e.g. Eaton, 1967; Bendiksen et al., 1991; Angeli and Hewitt, 2000) and bubble column reactors in chemical engineering (e.g. Krishna et al., 1999; Sanyal et al., 1999) for example. Figure 2.1. from Oddie and Pearson (2004) shows flow regimes in vertical pipes. As the gas flow rate increases relative to the rate of liquid flow, the flow regime changes from bubbly to slug to annular flow. Regime transitions also occur at constant flow rate in long tubes when bubbles coalesce during rise (Lucas et al., 2005). Bubbly flow is characterized by relatively small, isolated bubbles moving independently through the liquid. At high flow rates, the distribution of these bubbles becomes heterogeneous, causing large-scale gravitational flow in the pipe and eventual coalescence of the bubbles to form slugs (Mudde, 2005). In slug flow, large pipe-filling gas bubbles (slugs or Taylor bubbles) rise periodically, with liquid and dispersed smaller bubbles between slugs. In annular flow, the gas moves through the center of the pipe in its own open pathway, while the liquid moves along the sides. Churn flow is an unstable transition between slug flow and annular flow. At extremely high gas flow rates, the flow regime may transform to droplet flow, in which the liquid is transported as droplets in a gas column.

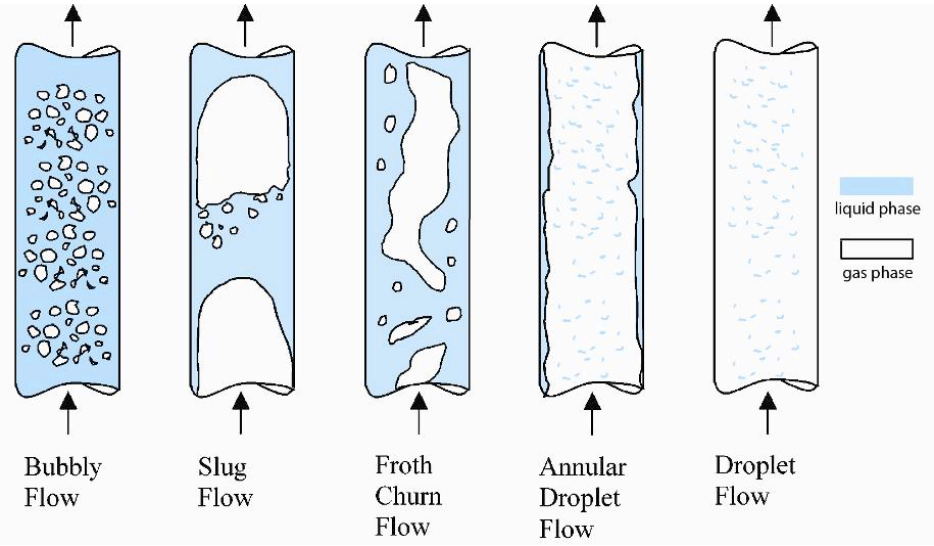

Figure 2.1. Flow regimes in a vertical pipe, from Oddie and Pearson (2004). Flow regimes change from bubbly to droplet with increasing gas flow rate relative to liquid flow.

To avoid confusion we should point out here that the term "slug" is used in several different ways. In engineering terminology, the slug is the liquid parcel that rises between Taylor bubbles in the slug flow regime. In volcanology, however, "slug" is used to indicate the Taylor bubble itself. The latter, volcanological, terminology is used throughout this text.

2.1. Two-phase flow regimes in volcanology

Gas-liquid flow regimes have been used to interpret flow dynamics of magma where the liquid is of sufficiently low viscosity that gas bubbles can rise independently. In volcanic systems characterized by high viscosity magma, or by high magma rise speeds, gas bubbles are entrained with the magma and the whole magma-bubble mixture

can be considered as a single fluid. In this study, we focus on low-viscosity systems where gas and magma are segregated. The three main eruption styles dominating low-viscosity (mafic) systems are the Hawaiian (fire fountaining), normal Strombolian and violent Strombolian eruption style, which differ in how much magma and gas is expelled during the eruptions (Figure 2.2.). In Hawaiian eruptions, the mass eruption rate is around 10^5-10^6 kg/s with gas fluxes on the order of 10^3 kg/s (Vergniolle and Mangan, 2000; Houghton and Gonnermann, 2008). Hawaiian eruptions are thought to result from bubbly magma with rise speeds fast enough that the bubbles do not have time to coalesce, but are entrained with the magma (e.g. Parfitt and Wilson, 1995). Annular flow has also been suggested for certain fire fountaining events (e.g. Vergniolle and Mangan, 2000), although it is unclear to what depth in the conduit the annulus extends. See Houghton and Gonnermann (2008) for a comparison of these two models.

Normal Strombolian eruptions are characterized by a lower magma flux, 10^0-10^4 kg/s, but a high gas/solid mass ratio (Chouet et al., 1974; Houghton and Gonnermann, 2008). Eruptive gas fluxes are on the order of 24-30 kg/s (Chouet et al., 1974; Allard et al., 1994), with ~360-960 kg/explosion (Mori and Burton, 2009). At Stromboli, gas emission occurs during Strombolian eruptions (Allard et al., 1994; Harris and Ripepe, 2007) as well as through passive degassing and puffing, during which limited or no magma is expelled. Normal Strombolian activity is widely attributed to slug flow in the conduit, a concept first developed by Blackburn et al. (1976) and adopted by many later workers. Individual explosions are then the result of a slug bursting at the magma free surface. Smaller and more frequent puffing activity at Stromboli has been attributed to bubbly flow in the conduit (Ripepe et al., 2002; Ripepe et al., 2007).

Violent Strombolian activity is the more explosive counterpart of the normal Strombolian eruption style, with higher mass eruption rates (~10^3 -10^6 kg/s) and gas fluxes on the order of 10^3-10^4 tons/day (~10-100 kg/s) (Arrighi et al., 2001; Pioli et al., 2008; D'Oriano et al., 2010b). It has been attributed to churn flow or a transition between the slug and churn regimes (Pioli et al., 2008). Mass eruption rates for "ash-rich jet and plume" activity at Etna volcano, which may be similar to violent Strombolian eruptions, are on the order of 10^4 kg/s (Andronico et al., 2008 and 2009).

The interpreted two-phase flow regimes for these three eruptive styles do not follow the succession from bubbly to slug to churn with increasing gas flux / mass flux (Figure 2.2.). This could indicate that one or more of the interpretations are not appropriate, or that other factors beside gas and mass flux influence the regime transitions.

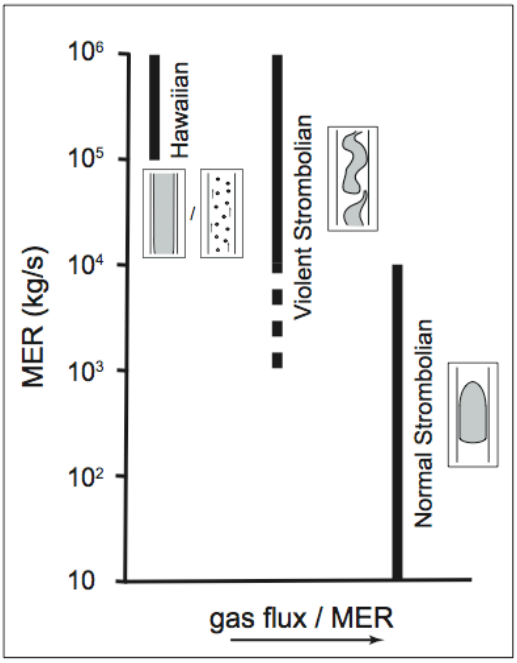

Figure 2.2. Two phase interpretations of the mafic eruption styles. Ranges of mass (magma) eruption rate (MER) and (volumetric) gas flux/MER (not to scale) are shown. See text for discussion.

2.2. The normal Strombolian eruption mechanism

Probably the most widely accepted application of two-phase flow regimes to volcanic systems is slug flow in the conduit as a mechanism to explain normal Strombolian activity. The high gas to magma ratio and periodicity of these eruptions are nicely explained by the periodic rise and bursting of large gas slugs at the magma free surface. There are two different views of how such large gas slugs form (see also Parfitt, 2004; Houghton and Gonnermann, 2008; Ripepe et al., 2008). In the collapsing foam model, introduced by Jaupart and Vergniolle (1988, 1989), slugs form by the accumulation and eventual coalescence of small bubbles on the roof of a magma chamber or some other geometrical obstruction. In the rise-speed dependent model, which originated with Parfitt and Wilson (1995), bubbles coalesce during rise if the bubble ascent velocity is fast compared to the magma rise speed.

Stromboli volcano is well monitored and there exists a huge body of literature that describes the nature of the activity, the petrological and geochemical details of the ejected magma, and geophysical data recorded at this volcano. Some of these data are hard to reconcile with the slug model. For example, Harris and Ripepe, 2007b observe time delays between seismic and infrasonic signals, thought to represent the formation of a slug at depth and its bursting at the surface respectively, which require unreasonably high slug ascent velocities (10-70 m/s). Potentially the largest problem, however, is that the slug model does not account for the high crystallinity of Stromboli's upper magma. Since the slug model was developed, multiple petrological studies have shown that a magma body with a crystallinity of ~50% (erupted as crystal-rich tephra during normal

Strombolian explosions) exists in the upper part of Stromboli's plumbing system (e.g. Métrich et al., 2001; Landi et al., 2004). Even though slugs may exist in the deeper, less crystalline magma, two-phase flow models may not be applicable in this upper magma, where the crystallinity approaches the maximum packing concentration (Marsh, 1981). We here investigate the influence of solid particles on the traditional two-phase flow regimes and on the efficiency of gas escape in an analogue system, and evaluate the applicability of two-phase models such as the slug model to crystal-rich volcanic systems.

3. Methods

We performed analogue experiments to investigate the effect of solid particles on flow regimes. Our setup consists of a vertical cylindrical Plexiglas tube with a 1.5 inch (3.81 cm) internal diameter (Figure 2.3.). Compressed air flows into the bottom through a perforated brass disc with holes that are < 0.5 mm in diameter. We vary the gas flow rate from 1 to 12 l/min in steps of 1 l/min. The tube is filled to 20 cm above the brass plate with liquid and varying concentrations of disc-shaped plastic particles. We use water and two types of corn syrup (light Karo® syrup and Globe® corn syrup) as the liquids. Fluid properties are listed in Table 2.1. The plastic beads have a density similar to that of the Karo syrup, and are approximately 3 mm in diameter. Particle concentrations range between 0 (pure liquid) and the packing concentration of the particles (~68.5% by volume), and were varied systematically in water and in Karo syrup to map out regime

diagrams for the different liquids. These experiments were not done in the denser Globe syrup since the particles float in this liquid.

	Water	Light Karo corn syrup	Globe corn syrup
Density (kg/m^3)	1000	1320	1420
Viscosity (Pa s)	0.001	4	20
Interfacial tension (N/m)	0.07	0.08	0.08

Table 2.1. Fluid properties of the liquids used in this study.

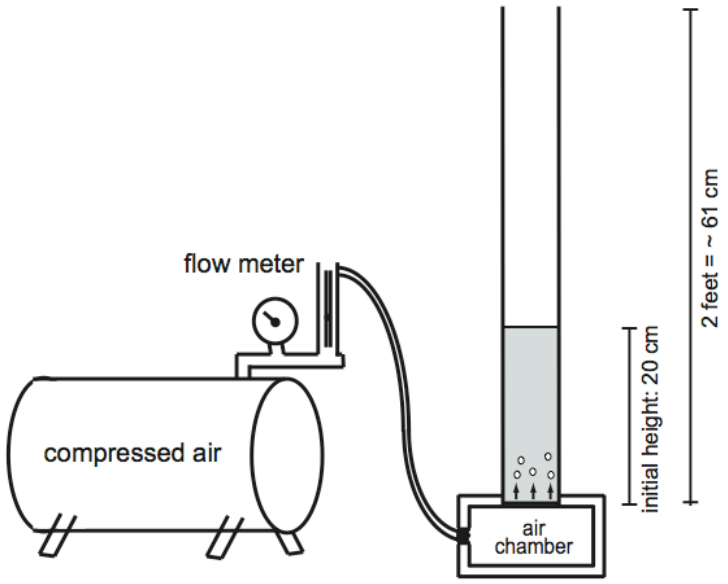

Figure 2.3. Experimental setup used to study flow regimes. Compressed air is injected as small bubbles into the base of a tube filled with liquid and solid particles. Air flow rates, particle concentrations and liquid viscosities are varied.

4. Experimental results

Our experiments exhibit three of the two-phase (gas-liquid) flow regimes: bubbly, slug and churn/annular flow. In addition, we observe two three-phase (gas-liquid-solid) regimes at high particle concentrations (Figure 2.4.). Two-phase bubbly flow is observed at low particle concentrations in water. The bubbly flow becomes more frothy with increasing air flow rate, and towards the top of the column as the bubbles grow during rise (which could occur both by expansion and coalescence). At higher flow rates, the bubbly regime transitions to slug flow. Slug flow is also observed at low flow rates and low particle concentrations in the corn syrups. With increasing flow rate, slug flow transitions to annular flow (corn syrups) or to a churn-like unsteady flow (water). In our experiments, the central open air pipe in annular flow periodically collapses as liquid on the tube walls flows down and covers the brass disc. This indicates that the air flow rate is never really high enough to keep the air pipe open, and our annular flow regime is probably more akin to slug flow in which the slugs are longer than the liquid height.

At high particle concentrations, two different regimes exist in water and in corn syrup (Karo). In water, a three-phase bubbly flow regime occurs, in which small bubbles rise through the pore space between the particles. The bubble pathways, velocities and shapes are controlled by the particles. In syrup, a modification of annular flow occurs, in which the central gas pipe becomes increasingly tortuous as the particle concentration increases. Cross-sections through this air pathway at different heights in the column vary widely in shape and width and can range from narrow “mouths” to sections in which the whole tube is filled by air, lifting the liquid-particle mixture above it and separating it

from the mixture underneath. When the air pipe collapses and closes up, air pressure needs to build up until it is high enough to "crack" its way through to the top of the liquid-particle mixture and form a new open channel.

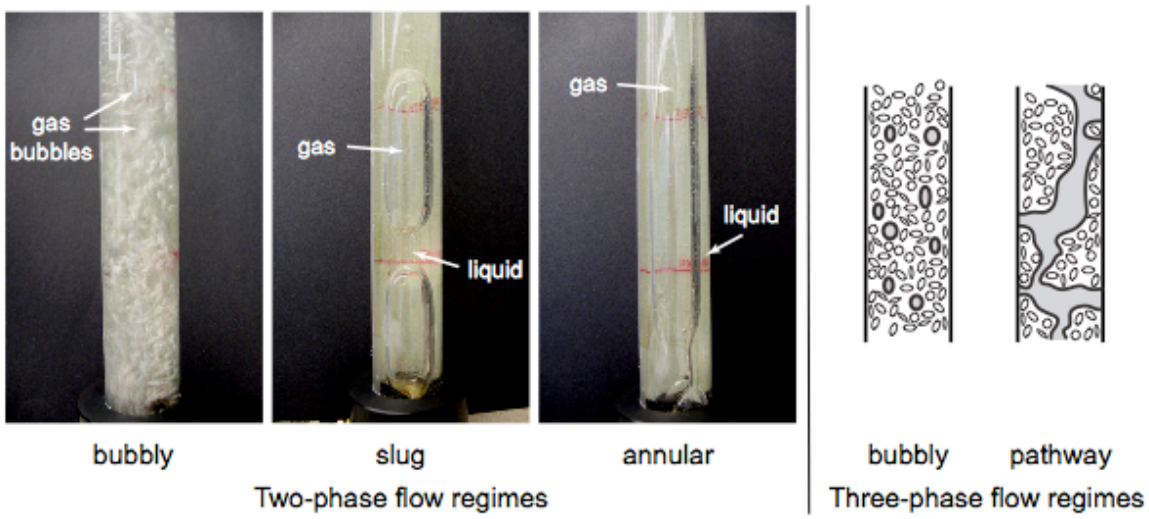

Figure 2.4. Flow regimes observed in our experiments. Two-phase regimes are shown in particle-free liquids. Due to the high particle concentrations associated with the three-phase regimes, these flow regimes could not be captured on photo and are illustrated schematically.

4.1. The effect of viscosity on flow regime

To examine the effect of viscosity on flow regime, we performed two-phase (gas-liquid) experiments at the same gas flow rates in three different liquids (Figure 2.5.). Transitions between regimes occur at lower flow rates in the higher viscosity liquids. At constant gas flow rate, increasing the liquid viscosity causes the flow regime to change

from bubbly to slug to annular, even though the size of the bubbles entering the liquid from the brass disc in our experiments is similar. Although our analogue liquids have different densities as well as viscosities, the difference in viscosity between the liquids is more dramatic (orders of magnitude; Table 2.1.) than the density difference, so that the observed changes in flow regime are likely controlled by the viscosity effect.

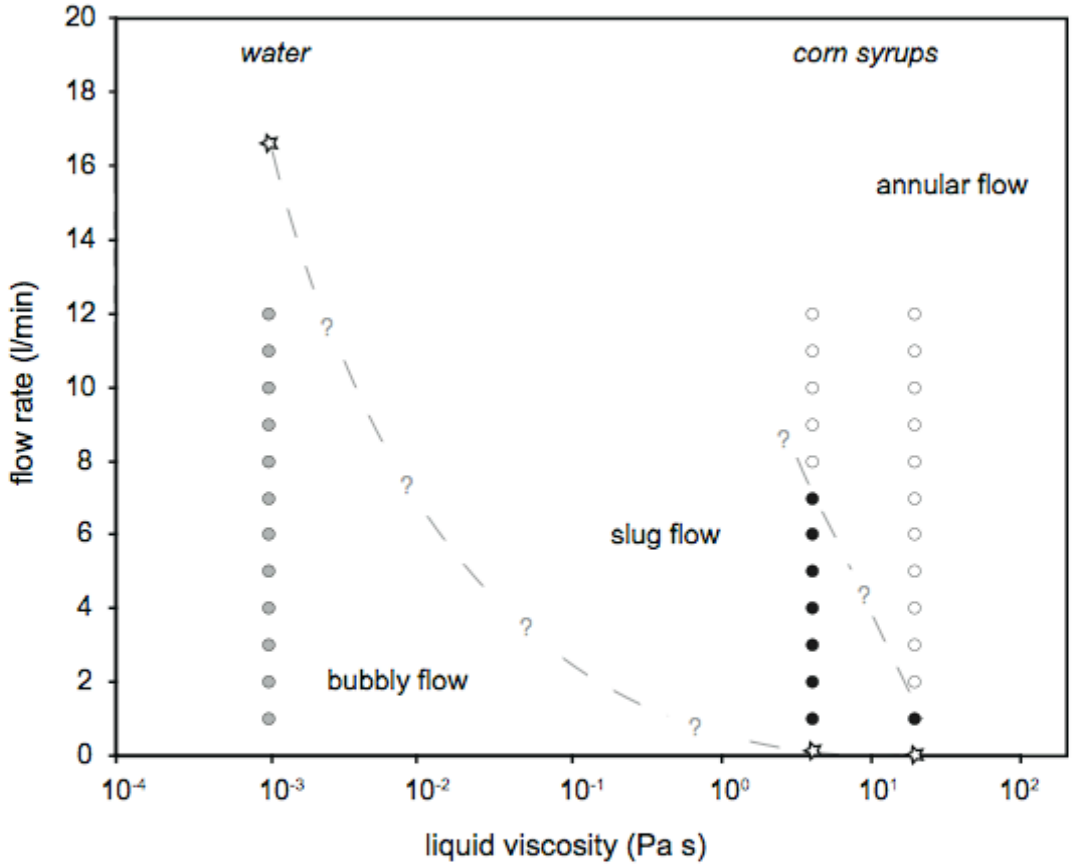

Figure 2.5. Flow regimes in two-phase systems with different viscosities in a vertical tube. Gray circles: bubbly flow; black circles: slug flow; open circles: annular flow. Stars show the calculated transition between bubbly flow and slug flow based on the rise velocity of individual small bubbles relative to the gas flow rate (see text for method). Gray dashed lines show the inferred regime transitions based on the calculated values (bubbly-slug) and experimental observations (slug-annular).

The influence of liquid viscosity (and density) on the transition between bubbly and slug flow in our experiments can be understood if we consider the rise velocity of the bubbles entering the liquid relative to the overall gas flow rate. If the bubbles that enter the liquid rise more slowly than the total gas flow rate, they will not be able to rise very far before new bubbles enter from the holes in the brass disc, and the chance of bubble coalescence directly above the disc increases. Fritz (1935, in Oguz and Prosperetti, 1993) provide an equation for the minimum radius R_{min} of a bubble exiting from a needle into a liquid with density ρ, viscosity μ, and bubble-liquid surface tension σ in terms of the needle's aperture radius R_a:

$$R_{min} = \left(\frac{3\sigma R_a}{2\rho g} \right)^{1/3}. \qquad (2.1)$$

R_{min} can then be inserted into Stokes' law (for viscous liquids)

$$U_{bubble} = \frac{R_{min}{}^2 \Delta\rho g}{3\mu} \qquad (2.2)$$

to calculate the rise velocity U_{bubble} of these individual bubbles in the corn syrups. The density contrast $\Delta\rho \approx \rho$ since the gas density is small relative to the liquid density. In the case of water, the bubbles in our experiments rise in the ellipsoidal sub-regime of bubbly flow described by Clift et al. (1978), and we use their equation describing the rise of individual bubbles in this sub-regime to calculate the bubble velocity:

$$U_{bubble} = \frac{\mu}{2R_{min}\rho} M^{-0.149}(J - 0.857), \qquad (2.3)$$

where M is the Morton number ($M = \frac{g\mu^4\Delta\rho}{\rho^2\sigma^3}$) and J is an empirical parameter that depends on fluid properties and bubble size. This equation is valid if wall effects are negligible (bubble radius << tube radius) and $M < 10^{-3}$, the Eötvös number

($Eo = \frac{g\Delta\rho(2R)^2}{\sigma}$) < 40, and the Reynolds number ($Re = \frac{2R\rho U_{bubble}}{\mu}$) > 0.1, which is the case in water in our experiments ($M \approx 3*10^{-11}$; $Eo \approx 1$; $Re \approx 674$). The velocities found in this way can be compared to the linear gas velocity calculated from the volumetric gas flow rate Q and the cross-sectional area A of the tube:

$$U_{linear} = Q/A. \qquad (2.4)$$

If $U_{bubble} \geq U_{linear}$, bubbles will rise before new ones are formed and we can expect that the flow regime will be bubbly. If $U_{bubble} < U_{linear}$, bubbles will collect in the liquid directly above the disc, leading to an increased chance of coalescence, which would give rise to slug flow. Note that in this case the transition depends on the bubble velocity rather than the bubble distribution; this mechanism is thus different from that described by Mudde (2005, see section 2), although in both situations the ultimate cause of the transition is bubble coalescence.

In our experiments, the holes in the brass disc have diameter < 0.5 mm. If we take aperture radius R = 0.25 mm, we get an estimated bubble radius according to Equation 2.1 and with the fluid properties listed in Table 2.1., of R_{min} = 1.39 mm in water, R_{min} = 1.32 mm in Karo syrup, and R_{min} = 1.29 mm in Globe corn syrup. The rise velocities of bubbles with this size, calculated from Equations 2.2 and 2.3, are 243 mm/s in water, 1.8 mm/s in Karo syrup and 0.4 mm/s in Globe corn syrup. The regime transition (U_{bubble} = U_{linear}) predicted with this method occurs at 16.6 l/min in water, 0.13 l/min in Karo syrup and 0.03 l/min in Globe corn syrup (stars on Figure 2.5.). Consistent with our experiments, the transition is predicted to occur at a higher flow rate than our experimental ones in water, and at lower flow rates than our experimental ones in the

corn syrups, so that our water data are completely in the bubbly flow regime and our syrup data start off in slug flow.

It is worth noting here that according to this simple line of reasoning, all slow bubbles will coalesce and give rise to slug flow. Fluid properties are not the only factors that determine whether gas flow will occur in the bubbly or the slug regime. It is conceivable that bubbles rising in the bubbly flow regime can be delayed, e.g. at an interface between fluids with different viscosities or at a geometrical obstruction, and cause a regime transition. Such a transition could occur deeper down in the tube and at smaller bubble volumes than a transition due to bubble coalescence during transport.

4.2. The effect of particles on flow regime

Flow regime maps for liquid-particle mixtures are shown in Figure 2.6. At low particle concentrations (below about ~45-50%), the effect of increasing particle content is similar to that of increasing liquid viscosity (Figure 2.5.). At high particle concentrations, however, the two-phase flow regimes transition into three-phase regimes, in which the solid phase actively influences the rise of gas through the system.

Our experiments in water (Figure 2.6., bottom panel) cover the bubbly, slug and churn flow regimes. The transition between regimes occurs at lower flow rates as the particle concentration is increased. Since the effect of particles in low concentrations seems to be similar to that of increasing viscosity, we can use the method described in section 4.1. to predict the bubbly-slug transition. To calculate the bulk viscosity of the

liquid+particle mixure, we use the modified Roscoe-Einstein equation (Krieger and Dougherty, 1959; Jeffrey and Acrivos, 1976):

$$\mu_{suspension} = \mu_{liquid}\left(1 - \frac{\phi}{\phi_{max}}\right)^{-2.5\phi_{max}},$$

where ϕ is the volume fraction of particles and ϕ_{max} is the packing fraction at which the particles are fully interacting (i.e. prevent each other's movement). The flow rates at which the transition is predicted to occur are shown on Figure 2.6. by the dotted lines, using $\phi_{max} = 0.685$ (measured packing concentration in our experiments), 0.45 (fraction at which the transition from two-phase to three-phase flow regimes starts to occur) and 0.22 (~ value at which particles start to touch according to Saar et al., 2001). This simple method confirms the decrease in flow rate of the transition with increasing viscosity (here determined by particle concentration), but does not predict the correct transition. This could be due to the limitations of the Roscoe-Einstein equation, which is valid for spheres, but may also indicate the importance of particle-particle interactions in controlling flow regime transitions, especially since the predicted flow rates decrease with the packing fraction at which these interactions are assumed to develop (lower ϕ_{max}). The slug flow regime disappears when the space-limiting effect of the particles becomes such that bubbles cannot fill the entire width of the tube. It transitions into an unsteady flow in which the liquid-particle mixture is vigorously mixed by the rise of large bubbles, the top and bottom ends of which frequently coalesce during rise. The transition between bubbly flow and this unsteady churn-like flow initially decreases, but reaches a constant gas flow rate between 50 vol.% and the packing concentration of the particles (68.5 vol.%). Once the packing concentration is reached, the churn flow regime disappears and

flow in all our experiments is bubbly, with bubbles rising through the space between the particles ("porous media flow"). At this concentration, particles are so closely spaced that they prevent each other from being entrained with the liquid, and mixing of the liquid-particle mixture only occurs near the very top of the column.

Our experiments in Karo syrup cover the slug and annular two-phase flow regimes. Bubbly flow is not observed in this liquid. The flow rate at which the transition between slug and annular flow occurs, decreases with increasing particle concentration up to ~40 vol.%. At this concentration, particles become so abundant that the annular pathway becomes contorted and the annular flow regime gradually transitions into the three-phase pathway regime. The tortuosity of the pathway increases and its width becomes more variable with increasing particle concentration.

At 40 vol.% particles, just below the amount where pathway flow comes into play, the transition between slug and annular flow occurs at our very lowest flow rate, so that we cannot tell from our experiments how slug flow would be influenced by the particles in the liquid. However, if we consider that our annular flow regime resembles slug flow in which the slugs are longer than the liquid height, we can speculate that slug flow will transition into a similar regime. In this case, the pathway might close up more frequently since the gas flow rate keeping it open is smaller, and a longer time might be needed to build up enough pressure to open a new pathway. At very low flow rates in Karo syrup, where the two-phase regime would be bubbly, we can hypothesize (following the reasoning used to predict the bubbly-slug transition in section 4.1.) that the high-crystallinity regime will be pathway-like if the particles slow bubble rise enough to

allow coalescence, and bubbly (similar to what we see in water) if bubbles can rise through the liquid in the pore space faster than the bubble input rate.

As the air flow rate increases for any one particle concentration, the amount of air in the liquid, and the height of the liquid (+ particles) + gas column in the tube, increases (Figure 2.7.). Gas content is expressed as a percentage of the initial liquid height, so that 100% means half the column is occupied by gas, and the total column height is double the initial height (note that this parameter is related to the concept of gas holdup used in chemical engineering (e.g. Sanyal et al., 1999; Angeli and Hewitt, 2000; Mena et al., 2005). At constant flow rate, the amount of air contained in the system decreases as particle concentration increases. This is similar to the results found by Mena et al. (2005) and many other workers (see references in ibid.) for the effect of particles in bubble column reactors (although the opposite effect is also observed in some cases), and is attributed to particle-induced bubble coalescence, which allows larger and thus faster bubbles to form. Other explanations could be the formation of permeable pathways at high particle concentrations, through which gas can escape passively (similar to the pathway formation observed in our Karo syrup experiments), or the formation of a rigid particle network, which allows small bubbles to percolate through (porous media flow, cf. our water experiments).

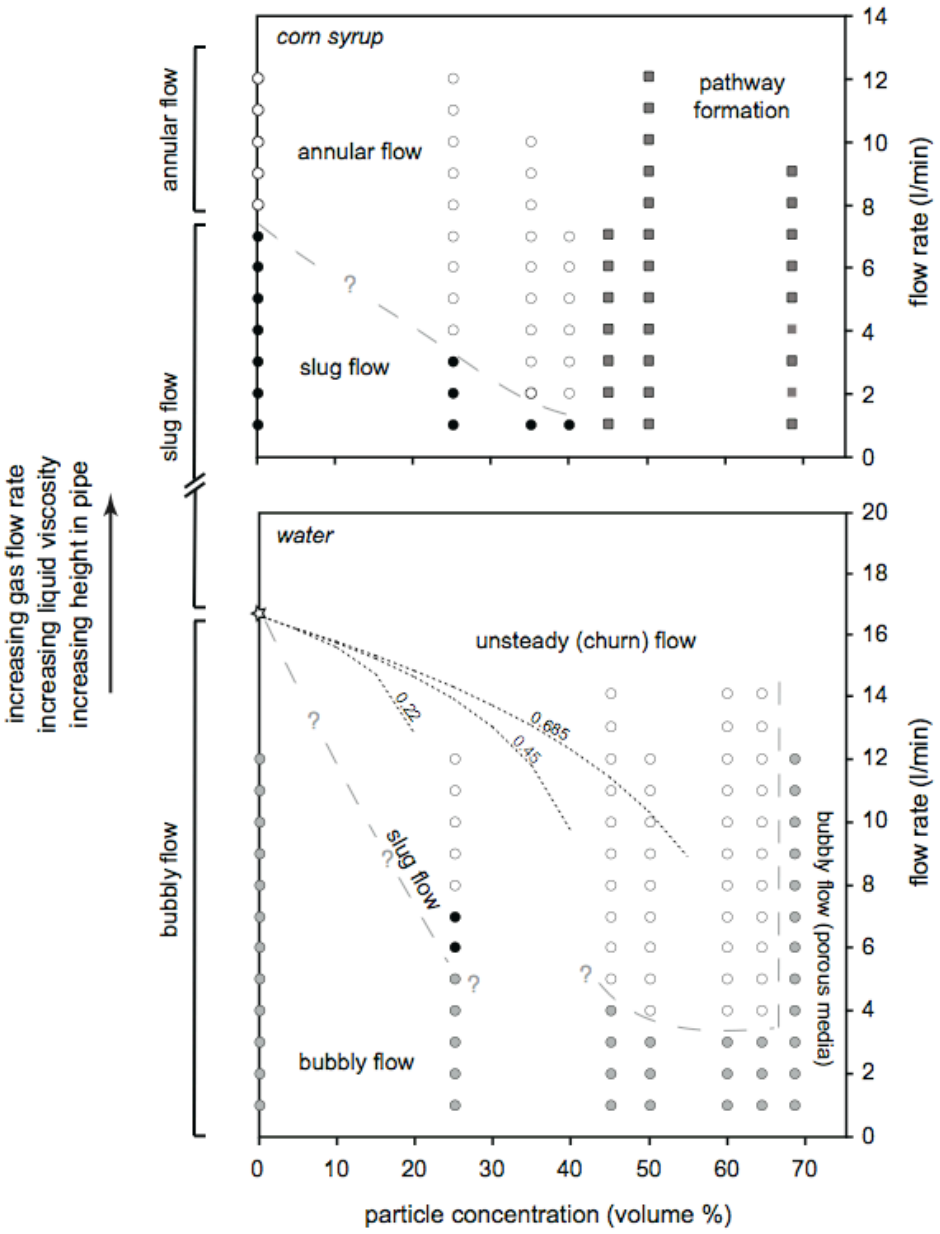

Figure 2.6. Flow regimes in water (bottom panel) and light Karo corn syrup (top panel) at different particle concentrations and air flow rates. Gray circles: bubbly flow; black circles: slug flow; open circles: churn/annular flow; squares: tortuous annular ("pathway") flow. The star shows the calculated transition between bubbly flow and slug flow at 0% particles in water (see text and Figure 2.5.). The dotted lines shows the calculated transitions by the same method, using the modified Roscoe-Einstein viscosity of the suspension ($\mu_{suspension} = \mu_{liquid}\left(1 - \frac{\phi}{\phi_{max}}\right)^{-2.5\phi_{max}}$;Krieger and Dougherty, 1959; Jeffrey and Acrivos, 1976) at different particle concentrations with ϕ_{max} = 0.685, 0.45 and 0.22 respectively (see text for discussion). Gray dashed lines show the transition between flow regimes inferred from experimental observations.

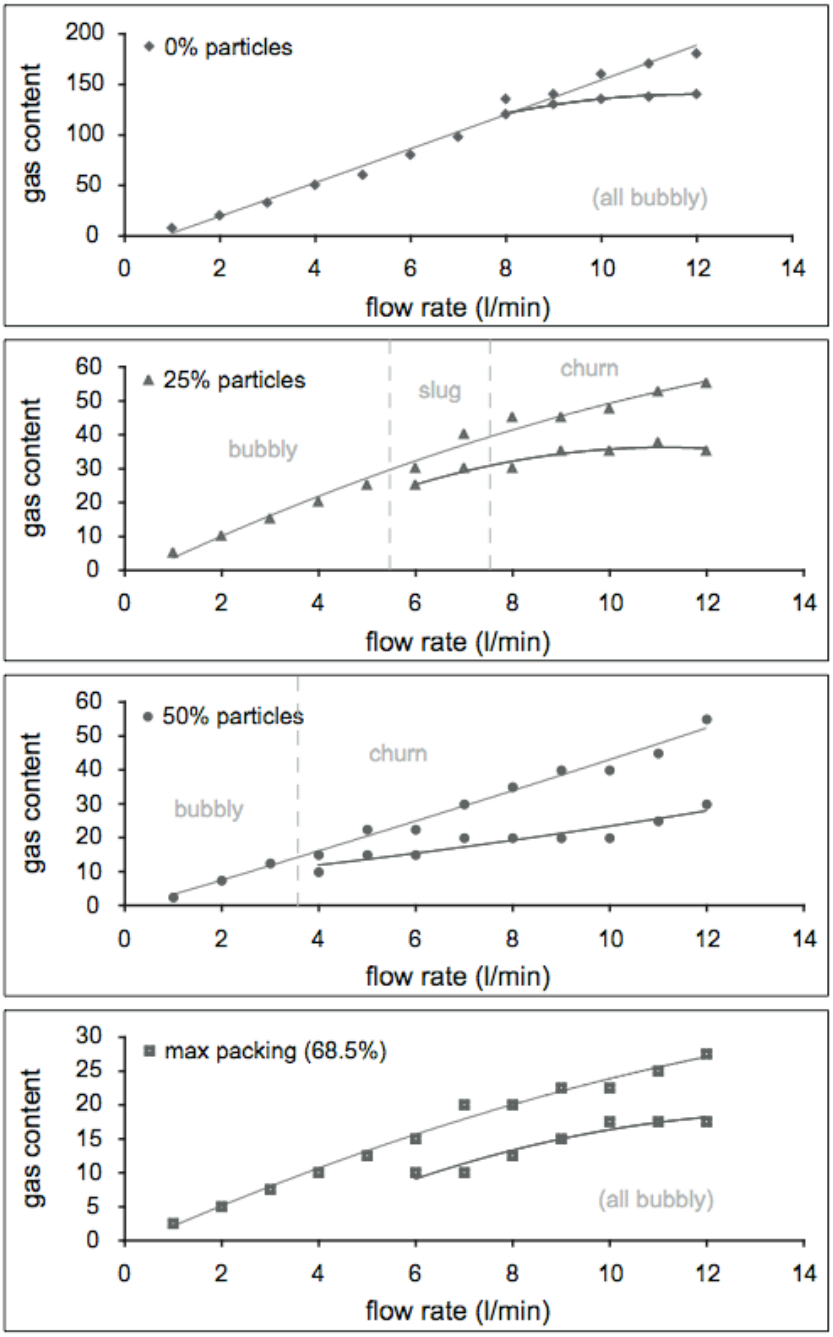

Figure 2.7. Gas content expressed as % of liquid entrained in the liquid (+ particle) column at each flow rate, at varying particle concentrations in water. Note the difference in y axis scale. At high flow rates, where flow is pulsatory or where the liquid level drops dramatically every time a large bubble bursts, two lines are shown, corresponding to the maximum (top curve) and minimum (bottom curve) column height.

5. Application to volcanic systems

Although we do not observe bubbly, slug and churn/annular flow in the same liquid in our experiments, we can use our results to develop a complete picture of the flow regimes that could occur in crystal-rich magma in a volcanic conduit. We have shown that regime transitions can be induced by increasing the gas flow rate and by increasing the liquid viscosity (Figure 2.5.). In addition, transitions can occur with increasing height in long tubes (Lucas et al., 2005). In magma in the absence of particles, we might expect a transition from bubbly to slug flow, as is argued for in the slug model for the normal Strombolian eruption mechanism (see section 2.2.). The rise speed dependent model (Parfitt and Wilson, 1995) and the collapsing foam model (Jaupart and Vergniolle, 1988 and 1989) for slug formation correspond to Lucas et al.'s (2005) bubble coalescence during rise and our bubble retardation model (section 4.1.) respectively. In Stromboli's upper magma, however, the crystallinity approaches the maximum packing concentration (cf. Marsh, 1981), in which case our experiments show that the three-phase flow regimes apply rather than the two-phase regimes. In this case, we expect a transition from bubble percolation through the crystal network to pathway formation with increasing height in the conduit. Bubble percolation occurs throughout the crystal-rich magma body at Stromboli, as shown by the multitude of bubbles trapped in crystal-rich tephra ejected during normal Strombolian eruptions (Figure 2.8.). Most of the degassing at Stromboli is non-eruptive; half of this gas is emitted through passive (quiescent) degassing (Harris and Ripepe, 2007), which occurs continuously from the vent and surrounding areas. We postulate that this passive degassing represents the arrival of the

percolating bubbles at the surface. The remainder of the non-eruptive degassing occurs through active degassing (puffing) (ibid.), which consists of the periodic arrival of overpressurized gas bursts at the vent, approximately every 2s. In light of our results, this behavior could relate to periodically collapsing and reopening pathways near the top of the magma body, perhaps due to increased viscosity of the uppermost part of the magma due to cooling at the surface. Permeable pathways have been proposed as a migration mechanism for passive degassing (Burton et al., 2007; Polacci et al., 2008), but the physical mechanism of pathway formation is not explained in these studies. Our three-phase model for gas migration through Stromboli's crystal-rich magma is schematically illustrated and compared to the two-phase situation in Figure 2.9.

Flow regimes similar to our three-phase regimes have recently been observed in a two-phase system in which the liquid is non-Newtonian (Divoux et al., 2011). In this case, the regime is purely bubbly if the flow rate is lower than a critical flow rate Q_{crit}; if $Q > Q_{crit}$, the regime alternates between bubbly flow and a gas pathway that spans the liquid column. Divoux et al. (2011) interpret the bubbly regime, which in their case consists of a single bubble train, as giving rise to explosion-generating gas bursts, while the pathway regime could correspond either to passive degassing or Hawaiian fire fountaining (assumed to correspond to annular flow in the conventional Newtonian two-phase interpretation). In our current model, bubble percolation, with potential pathway formation near the surface, is proposed as a non-eruptive degassing mechanism, independent of the Strombolian eruption mechanism (which is discussed in Chapter V). In addition to directly taking crystals into account, our model thus more closely

corresponds to the situation at Stromboli where passive and active degassing (puffing) continue uninterrupted during Strombolian eruptions.

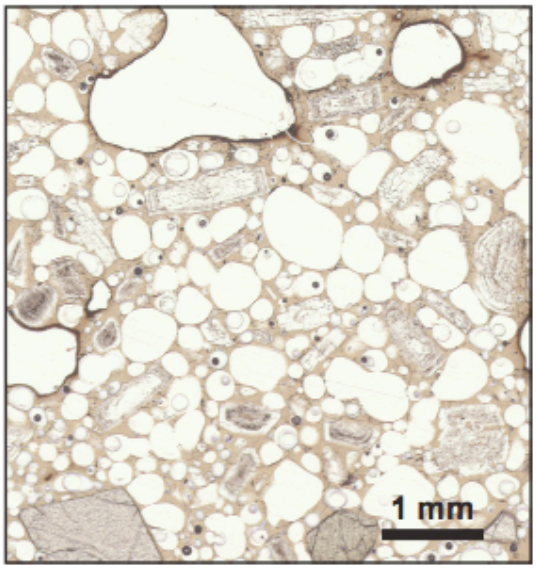

Figure 2.8. A thin section image from crystal-rich tephra erupted at Stromboli, showing a multitude of small bubbles (white) present between the crystals (various shades of gray and white; uniform browns are matrix glass).

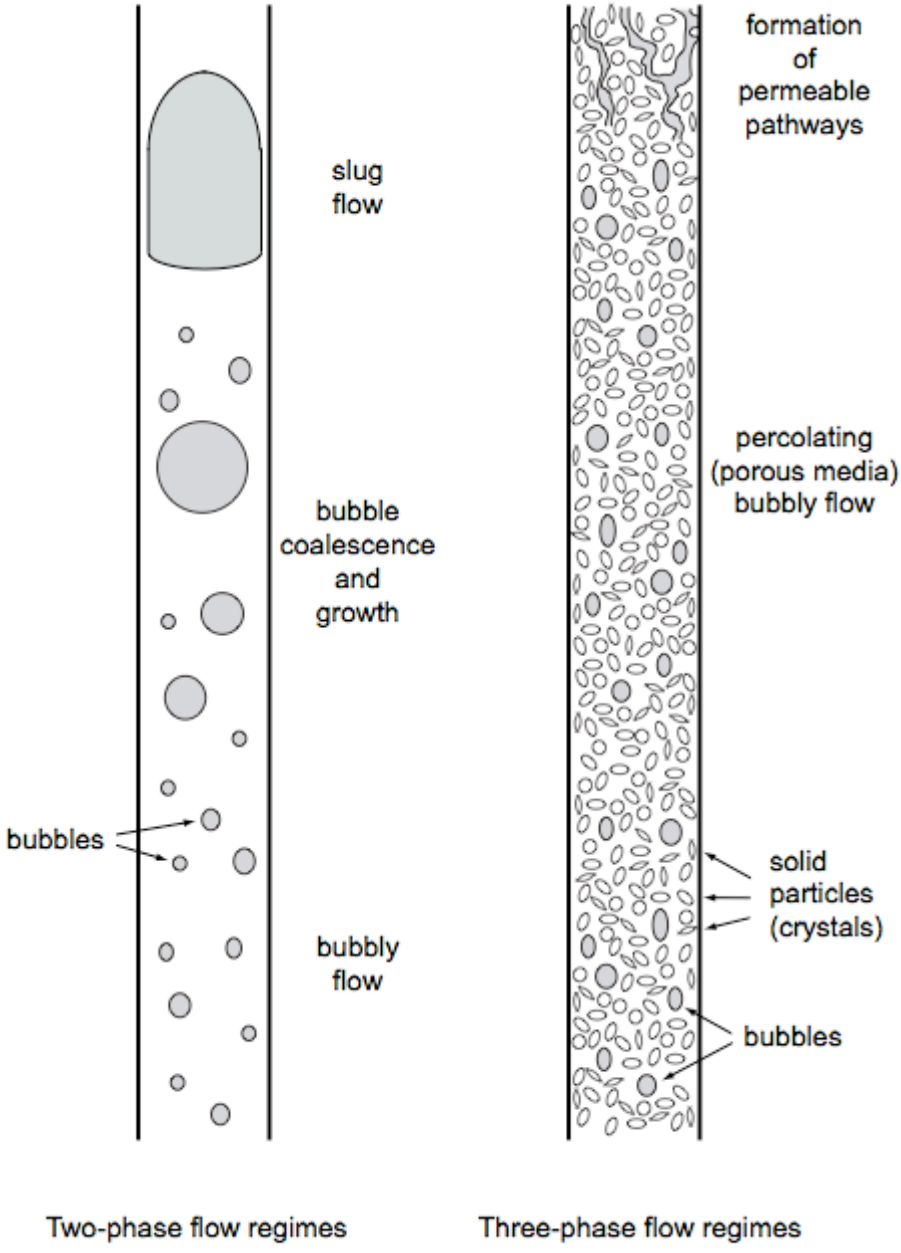

Figure 2.9. Simple two-phase and three-phase models for flow regimes occurring in a volcanic conduit.

For bubbly flow in water, we have shown that the amount of gas per volume liquid is lower when there are more solid particles present (Figure 2.7.). Applied to bubbly flow in the crystal-rich magma at Stromboli volcano, this means that we should expect to see less vesicularity in more crystalline rock samples. This has indeed been observed in silicic magma, where it is explained by simultaneous crystal settling and bubble rise (Gualda et al., 2004). To test if this applies to crystal-rich basaltic systems such as Stromboli, we analyzed 21 representative areas of thin section scans from tephra erupted during normal Strombolian explosions. These areas come from 7 tephra samples representing a range in intensity of the eruptive activity during 2007, 2008 and 2009. We measured vesicularities, defined as the area taken up by gas relative to the crystal-free (gas+liquid) area, and crystallinities, defined as the area taken up by crystals relative to the total (gas+liquid+crystals) area for each image. Bubbles and crystals were highlighted in Photoshop®, and their areas were extracted in MATLAB®. A detailed discussion of the methodology as well as the MATLAB® code programmed for the analysis can be found in Appendix B. Our samples indeed show a negative correlation between crystallinity and vesicularity during normal levels of activity (Figure 2.10., circles). Our analysis includes some samples erupted during so-called "major explosions" (diamonds on Figure 2.10.), which are larger than usual Strombolian eruptions and have higher infrasonic pressures and exit velocities. Samples erupted during major explosions have anomalously high vesicularities compared to the trend of the normal eruptions, but also show a decrease in vesicularity with increasing crystallinity. These results imply that changes in vesicularity observed in tephra may be locally influenced by heterogeneities in the crystallinity of the crystal-rich magma body. Changes in bubble number density (the number of bubbles

present per unit area) in tephra from Stromboli have been shown to correlate inversely with changes in eruptive degassing (Colò et al., 2010). Lower bubble number densities, which occur during periods of heightened eruptive activity, are attributed to an increase in gas content in the magma leading to more efficient coalescence and fewer, larger bubbles. Since Stromboli's crystal-rich magma is considered very stable through time (Armienti et al., 2007), we do not expect significant changes in crystallinity to occur that would cause changes in degassing efficiency on a system-wide scale. The changes in eruptive intensity seen by Colò et al. (2010) are thus likely caused by a process originating in the deeper plumbing system (e.g. a change in gas flux, cf. Ripepe et al., 2008), of which the change in bubble number density is another expression.

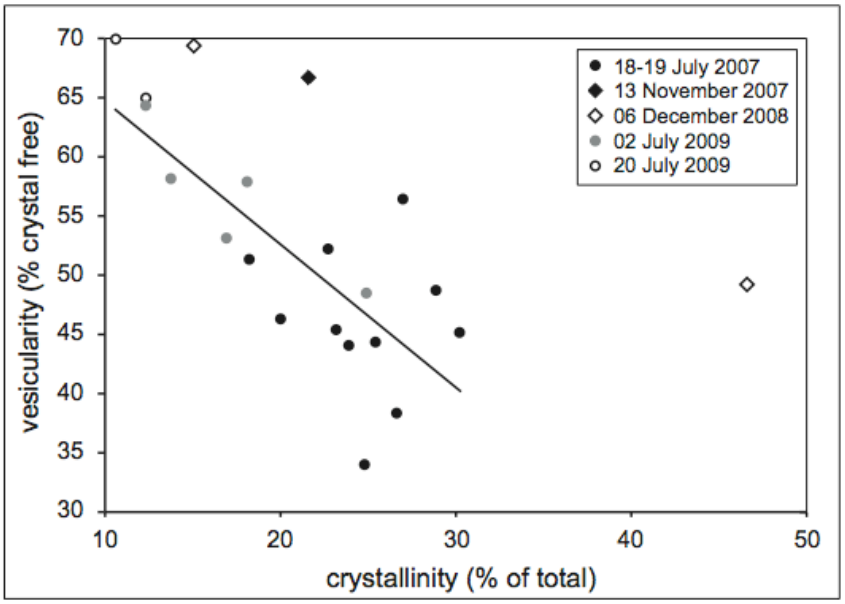

Figure 2.10. Crystal-free vesicularity as function of crystallinity for representative areas of thin section scans from crystal-rich tephra erupted at Stromboli (eruption dates in legend). Circles represent samples erupted during normal levels of Strombolian activity; diamonds represent samples from major explosions (Strombolian eruptions of large amplitude). The line is the linear regression through the circles.

6. Conclusions

We have performed analogue experiments to investigate the effect of solid particles on flow regimes in a vertical pipe. We find that at low concentrations, the particles have the same effect as increasing liquid viscosity, and the two-phase gas-liquid flow regimes still occur. With increasing particle concentration or viscosity, the flow rates at which the transitions between bubbly and slug flow and between slug and annular flow occur become progressively lower. This can be understood if we compare the rise rate of the bubbles formed at the base of the pipe to the linear gas flow rate. If bubbles rise more slowly than the linear flow rate, they will coalesce at the base of the pipe to form slugs, whereas if the bubble velocity is faster, bubbles will rise before new bubbles form and the flow regime will be bubbly. At high particle concentrations, the two-phase flow regimes transition into three-phase, gas-liquid-solid regimes. Bubbly flow transitions into a bubbly "porous media" flow, in which bubbles move through the liquid in the pore space between the particles. Annular flow and, we infer, slug flow, transition into a "pathway flow", in which an irregular open air pathway forms through which gas passively escapes. At high concentrations, particles increase the degassing efficiency, and lead to a lowered gas fraction in the system as a whole.

Applied to Stromboli volcano in Italy, where a magma with ~ 50 vol% crystals resides in the upper plumbing system, these results show that the widespread model of slug flow as an eruption mechanism is unlikely. We propose that bubbly flow in the pore space between the crystals predominates in the upper plumbing system, with formation of permeable pathways near the top of the magma body. We relate these two three-phase

flow regimes to passive degassing and puffing behavior at Stromboli. Explosive degassing and changes in the intensity of the normal Strombolian eruptions at this volcano are likely related to a process originating in the deeper plumbing system (e.g. changes in gas flux).

7. Bridge

In the previous chapter, I have investigated the influence of solid particles on flow regimes and on degassing efficiency. I have shown that slug flow is unlikely in Stromboli's crystal-rich magma, and that bubbly flow through the pore space predominates with the possible formation of permeable pathways near the top of the magma column. I have related these three-phase flow regimes to passive and active non-eruptive degassing, and shown that eruptive degassing is likely controlled by a deepseated change in e.g. gas flux, which independently influences both the intensity of the eruptive activity and the bubble number densities observed in tephra. In the following chapter, I take a closer look at the influence of crystals on small bubble populations seen in tephra, including bubble shapes and size distributions, and discuss the potential influence of a change in gas flux on these bubble populations. This latter discussion (Chapter III, section 5.2.) was written before the investigation of vesicularity versus crystallinity in tephra in Chapter II, section 5 was done; both discussions are complementary and should be viewed together.

CHAPTER III

GAS ACCUMULATION IN PARTICLE-RICH SUSPENSIONS AND IMPLICATIONS FOR BUBBLE POPULATIONS IN CRYSTAL-RICH MAGMA

This chapter was published in Earth and Planetary Science Letters (2010), (Belien IB, Cashman KV and Rempel AW (2010). Gas accumulation in particle-rich suspensions and implications for bubble populations in crystal-rich magma. Earth and Planetary Science Letters 297, 133-140) with co-authors Katharine Cashman and Alan Rempel. All the work was done by myself, with help in the lab from NSF UCORE summer students Christine Strand and Tina Wilson. Drs. Cashman and Rempel provided guidance for this project. Funding was provided by NSF grant EAR0810231 to Drs. Cashman and Rempel, and GSA student research grant # 9090-09 to myself. Thanks to reviewers Maurizio Ripepe and Margaret Mangan for helpful comments on the manuscript.

1. Introduction

Mafic eruptions are commonly interpreted using results of two-phase flow experiments (e.g. Vergniolle and Mangan, 2000). However, many volcanic systems include three phases (solid, liquid, gas), where the crystals present in suspension may influence the rise of gas bubbles. If the crystal concentration is low, the crystal-liquid mixture can be treated as a fluid with higher effective density and viscosity than the liquid phase alone, slowing bubble rise. If the crystal concentration is high, however, crystals might not be able to move freely, and the effect of solids on gas bubbles could be

more complicated. In this study, we use analogue experiments to investigate the influence of particles on bubble populations in low Reynolds number (viscous) systems with high particle concentrations (~50% by volume). We focus on the dynamics of small bubbles in viscous suspensions, and examine what this can tell us about gas flux. We apply our results to Stromboli volcano, Italy, where the crystallinity is similar to the particle concentrations in our experiments, and gas rises through a mostly stagnant magma.

Experiments similar to ours have been done in high Reynolds number systems in chemical engineering. In these systems, the local percentage of gas in the system (termed gas holdup) generally decreases with increasing solids concentration because of an increase in particle-aided bubble coalescence. However, these studies demonstrate that the effect of particles on gas holdup is complicated and depends on both particle size and concentration (see Mena et al., 2005, for an overview). Here, we focus on the low Reynolds number equivalent, where inertia is negligible.

We compare the results of our experiments to bubble and crystal populations observed in tephra from Stromboli volcano. At Stromboli, gas migration through a shallow crystal-rich magma produces ~13 megatons of gas per day, of which only 10% is accompanied by eruption of volcanic rocks (Harris and Ripepe, 2007). These Strombolian eruptions occur every 10-15 minutes and eject tephra and ash to heights of a few hundred meters. Non-eruptive active degassing episodes (puffing) account for another 45% of the gas (Harris and Ripepe, 2007). These events are frequent (~ every 2 seconds) and produce pressure pulses of ~10^3 Pa at the vent (Ripepe et al., 2007). The remaining ~45% of degassing is completely passive. This shows that the overall gas flux at Stromboli far outstrips the magma flux.

At Stromboli, two magmas are inferred to exist at depth. They have similar, high potassium-basaltic compositions but differ in crystal content. Tephra erupted during normal Strombolian activity derives from magma with a crystallinity of approximately 50%. This (shallow) magma resides above a more volatile-rich and crystal-poor magma that is erupted as pumice during infrequent paroxysms (e.g. Bertagnini et al., 2003; Landi et al., 2004).

To investigate the mechanisms of small bubble migration through a crystal-rich, essentially stagnant magma such as at Stromboli, we perform analogue experiments using solid particles (plastic beads), gas (air bubbles) and a viscous fluid (corn syrup). We use different experimental setups to study 1) the influence of solid particles on the rise of a single bubble and 2) the influence of solid particles on bubble populations. In what follows, we first discuss our analogue experiments. We then use our experimental results to interpret bubble populations in crystal-rich tephra from Stromboli. We discuss the applicability of our experiments to Stromboli through a comparison of dimensionless parameters in both systems. We then combine our experimental results with data from the literature to speculate on the effect of gas flux on bubble populations at Stromboli.

2. Experiments and observations

We examine the rise of small bubbles through a viscous suspension using analogue experiments. The physical properties of the materials used in these experiments are listed in Table 1. Below, we first describe the setup and then the observations for three different sets of experiments. The first two examine how a single rising bubble

interacts with particles. The third experiment examines the interactions of a stream of bubbles with particles.

2.1. Individual bubbles

The setup for the first set of experiments consists of a Plexiglas tank with a syringe and needle connected to the bottom (Figure 3.1.a). The tank is 15 cm wide, 25 cm tall and narrow (1.5 cm) in the third dimension (a Hele-Shaw cell) to ensure visibility through the particle layer. A randomly packed layer of plastic cubes with 7 mm sides was suspended on the interface between two types of corn syrup with different densities and viscosities (Table 3.1.). The particle concentration in the suspension was approximately 50% by volume. The thickness of the particle layer was varied between 1 and 10 cm. Air injected into the system from below produced bubble sizes of 0.1 to 1 ml (bubble:particle width ratio ψ between 0.8 and 1.8). Measured wetting angles indicate that, in common with magmatic systems, the liquid phase preferentially wets the solid particles.

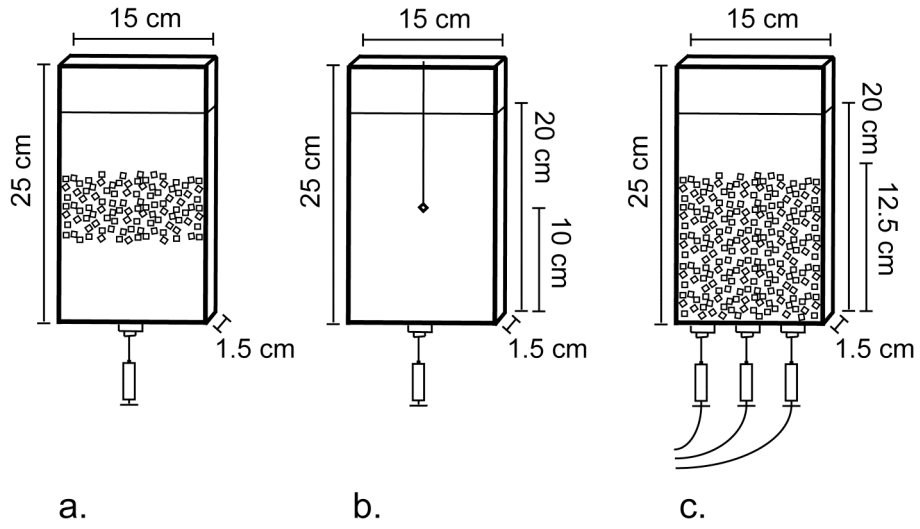

Figure 3.1. Schematic of setups used to study a) styles of interaction between a single bubble and particles in suspension, b) occurrence frequency of different interaction styles between a single bubble and a single particle, and c) the effect of a particle suspension on bubble size distributions.

Increasing the bubble size relative to the particle size causes the interaction style to change (Figure 3.2.). When the bubble is much smaller than the pores in the suspension, it rises through the pores without displacing the particles and undergoes only minimal deformation (Figure 3.2.a). The speed of bubble rise varies along its contorted pathway around the particles. Very small bubbles sometimes stall completely beneath a particle, so that they are effectively trapped within the suspension. When the bubble is large and the particle layer is thin, the bubble can displace the particles in such a way that the bubble deformation remains small relative to the deformation of the suspension layer (Figure 3.2.d). When the particle layer is thick and the bubble is too large to move between particles without deforming, it can either elongate to move through the pores (Figure 3.2.b), or flatten underneath an individual particle.

		This study	Mafic magma Stromboli [b]	Mafic magma	Silicic magma	Sea-water
liquid	ρ (kg/m^3)	light syrup: 1320 dense syrup: 1421	2690	2500-2700 [c]	2350-2450 [c]	1000
	η (Pa s)	light syrup: 4.12 dense syrup: 20	330	10^1-10^3 [c]	10^5-10^{10} [c]	0.0018
gas	V_b (ml)	0.1-1				
	d (mm)	5.8-12.4	0.1-0.3			
liquid + gas	σ (N/m)	0.071 [a]	0.1-0.4	0.09-0.4 [d]	0.042-0.3 [e]	0.072
solid	w (mm)	7	0.1-0.3			
liquid + gas + solid	α (^{o})	10-30	0			

Table 3.1. Properties of materials used in this study compared to natural systems. ρ: density, η: viscosity, V_b: bubble volume, d: bubble equivalent diameter, σ: surface tension, w: particle width, α: gas-solid wetting angle. Liquid properties for this study are measured at room temperature. [a] Value for the light syrup; the dense syrup was too sticky for the apparatus and its σ could not be measured. [b] Stromboli ρ: from Métrich et al. (2001) and Bertagnini et al. (2003) from glass in melt inclusions in pumice, η: calculated from compositional data for glassy matrices in crystal-rich scoria in Landi et al. (2004) using the method of Shaw (1972) with 0.1 weight% H_2O and T = 1115 ^{o}C (Landi et al., 2008) (not corrected for the influence of crystals), σ: based on Khitarov et al. (1979), d and w: dominant bubble and crystal sizes from Figure 5a. Note that ρ and η are measured or calculated for glass and not corrected for the influence of crystals, and thus represent the density and viscosity of the melt phase alone and not the bulk magma. [c] Approximate volatile-free values at 1 bar, based on Spera (2000). [d] Basalt values from Khitarov et al. (1979). [e] Compositions ranging from dacite to synthetic haplogranite, from Bagdassarov et al. (2000) and Mangan and Sisson (2005). Wetting angles are measured on photos for experiments. SEM images for Stromboli show thin glass (melt) films between bubbles and crystals, indicating that the melt preferentially wets the crystals (0^o wetting angle).

After a bubble flattens, it may either move around the particle or split into two or more parts (Figure 3.2.c) to create new bubbles that are sufficiently small to move through available pores in the network. The specific response depends on particle orientation (flat

side down or edge down), position relative to the bubble (in the middle; towards the edge), and the bubble:particle size ratio ψ.

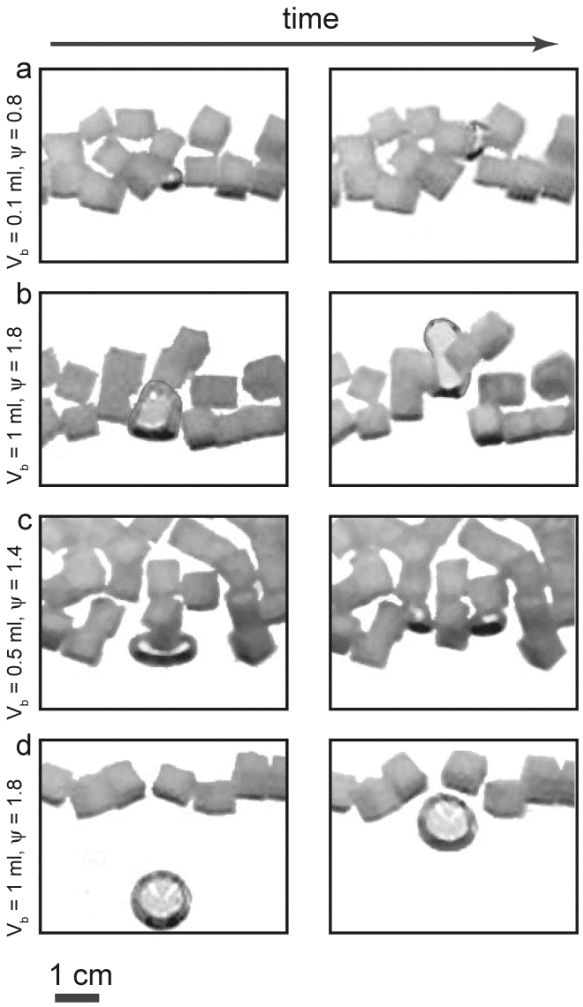

Figure 3.2. Styles of interaction between a bubble and particles suspended in a viscous fluid. Interaction style changes from a. to b./c. with increasing bubble volume. d. occurs when bubbles are large and particles can move freely. See text for details.

2.2. Splitting probabilities

We also determined probabilities of different interaction styles between a single bubble and a single particle in a setup in which a particle was suspended from a metal rod into the low viscosity syrup (Figure 3.1.b). We injected a single bubble into the syrup approximately 10 cm below the particle, and tracked, through repeat experiments, how often the bubble was stuck, split around the particle, or moved around the particle without splitting. A bubble was considered stuck when it remained trapped beneath the particle for more than 2 minutes (during which time our smallest (0.1 ml) bubbles could rise almost 70 cm if unhindered). A bubble was considered split when it broke into smaller bubbles as a result of interacting with the particle. If these smaller bubbles were similar in size to each other, they usually ascended on opposite sides of the particle. If one part was much larger than the other part, the smaller part remained close to the particle for long periods of time, moving slowly up its side (either the same or the opposite side as the large part of the bubble). Small bubbles from different splitting events accumulated close to the particle. A bubble was considered complete when it moved around the particle without splitting.

We varied bubble size between 0.1 and 1 ml ($0.8 \leq \psi \leq 1.8$) and performed these experiments with the particle orientation both flat side facing down and edge facing down, to examine how the frequency of occurrence of each interaction style changes with bubble volume and particle orientation. Each experiment was repeated 50 times to obtain statistically meaningful results, which are shown in Figure 3.3.

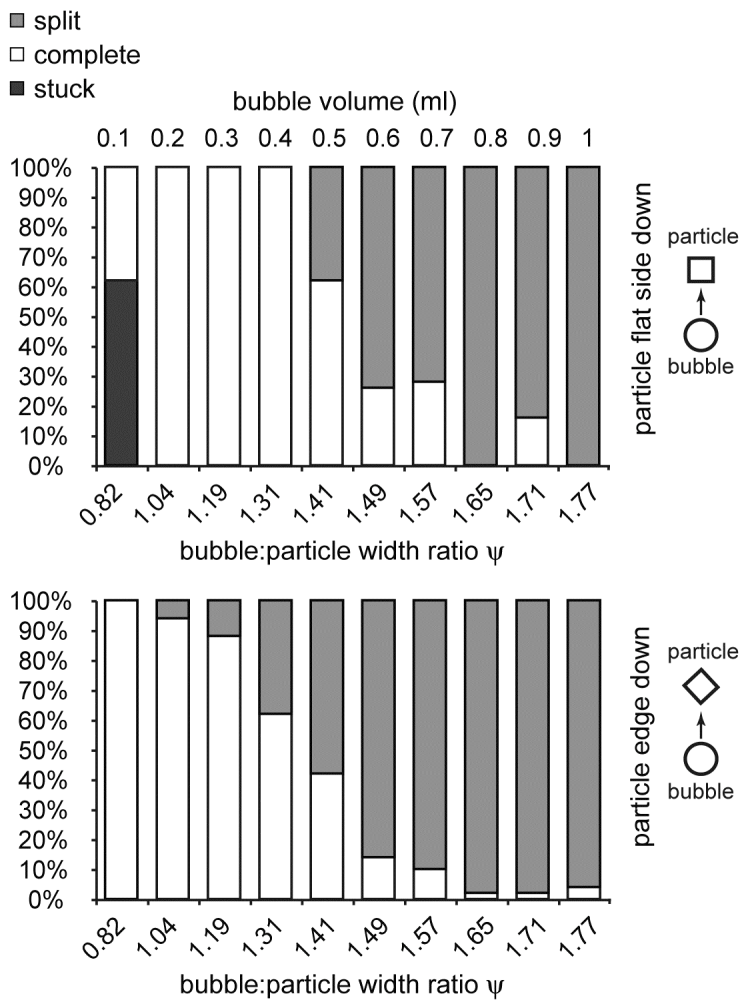

Figure 3.3. Occurrence frequencies of interaction styles between a single particle and a single bubble injected directly underneath for different particle orientations. Top: flat side down, bottom: edge down.

Our experiments show that the probability of the smallest bubbles getting stuck underneath the particle is approximately 60% when the particle is oriented flat side down. In experiments with a suspension this probability would be higher, since bubbles could also become trapped beneath clusters of particles (assuming these could not be pushed aside easily by the bubble). Bubbles did not stagnate beneath particles oriented with the

edge pointed down. The probability of stagnation decreases dramatically with bubble size, while the probability that a bubble will split around the particle increases with bubble size. Bubbles are more likely to split when the particle is oriented with an edge facing downward. Both the generation of small bubbles from large ones by splitting and the high probability of small bubbles remaining trapped beneath particles indicate that there should be a relative enrichment of small bubbles in high-crystallinity systems.

2.3. Bubble populations

To study the effect of solid particles on bubble populations in a system that is fluxed with gas, we used a similar setup to that used in the first set of experiments, except that it included three injection ports at the base of the tank (Figure 3.1.c). We injected bubbles from three nozzles simultaneously every 10 seconds. The experiments were videotaped and individual movie frames analyzed with the image analysis software ImageJ (Abramoff et al., 2004). The size distribution of bubbles present in the system was determined from movie frames extracted at set time intervals after the start of injection of the bubble stream. Only the low density, low viscosity syrup was used in these experiments to avoid mixing of the syrups by moving bubbles. The particles are more dense than the syrup and formed a randomly packed, 12.5 cm thick layer at the bottom of the tank. The particle concentration was approximately 50% by volume, which is comparable to the solids concentrations in high-crystallinity magmas.

At the start of each experiment, some bubbles trapped during creation of the suspension were present in the system. These were flushed out by repeated bubble

injections, as indicated by the measured bubble size distribution, which narrowed with time to a distribution around the input bubble size (see Figure 3.4. for an example).

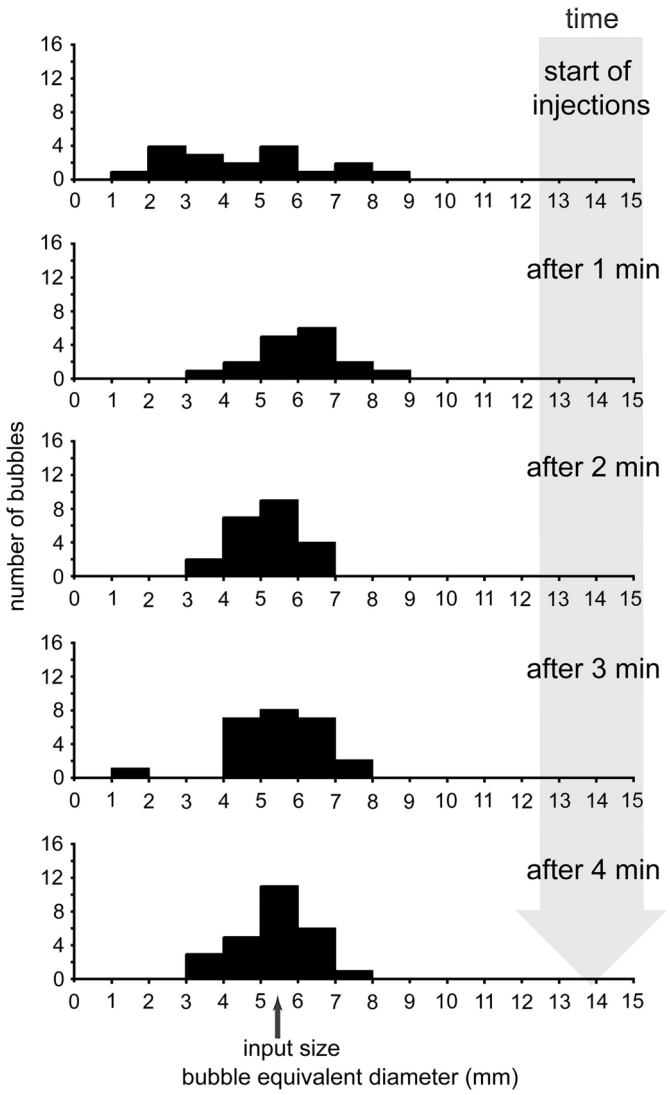

Figure 3.4. Evolution of bubble size distribution through time in a particle suspension fluxed through with 0.1 ml bubbles (equivalent diameter 5.8 mm; ψ=0.8). We did not observe bubble splitting or coalescence at this input size, so we infer that the steady-state spread in the distribution does not reflect a real change in bubble size in the system. Instead, the apparent spread is attributed to bubbles appearing smaller when they are partly hidden behind particles and larger when they are flattened between a particle and the front wall of the tank.

Figure 3.5. shows histograms from movie frames taken near the end of each experiment, when the spread is assumed to have reached its steady-state width. The gray area represents the spread expected in the absence of splitting or coalescence and is instead due to bubbles appearing smaller when they are partly hidden behind particles and larger when they are flattened between a particle and the front wall of the tank. This spread may be determined from the 0.1 ml experiment, where no splitting or coalescence was observed. Small bubbles become increasingly abundant as the input bubble size increases, indicating frequent bubble breakup. In contrast, bubble coalescence appears almost negligible. When coalescence was observed, it usually happened as bubbles were exiting the particle layer.

2.4. Summary of experimental observations

Our experiments show that bubbles interact with suspended particles in different ways (Section 2.1. and Figure 3.2.) depending on the size of the bubble relative to the pore size (which depends on particle size, shape and concentration). Small bubbles move through the pores without deforming, and can stagnate beneath particles. Bubbles that are wider than the pores may deform to move between particles. If the particles do not block each other's movement, they can be displaced to a limited extent by the rising bubble.

Particles can cause large bubbles ($\psi > 1$) to split into smaller ones. The frequency of breakup is highest for large bubble:particle width ratios (Section 2.2. and Figure 3.3.) and decreases rapidly with decreasing bubble size. Breakup occurs for all particle orientations, but is most pronounced when the particle is oriented edge down.

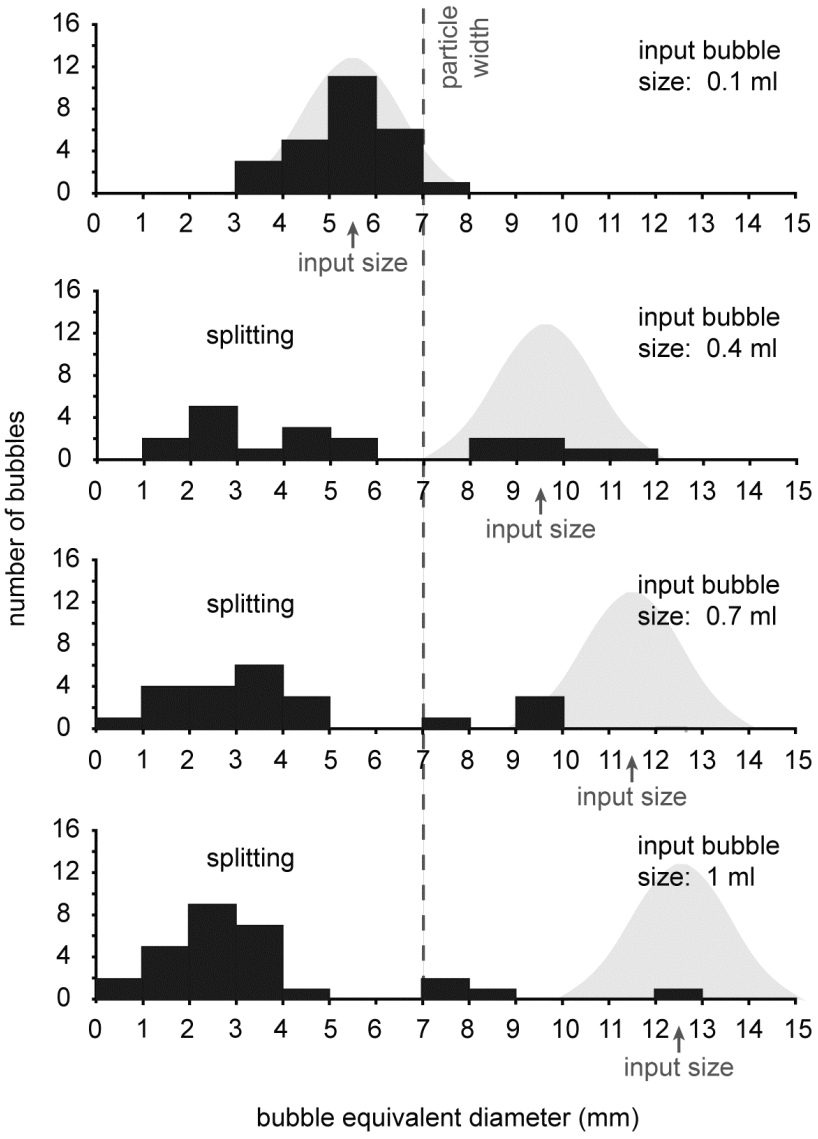

Figure 3.5. Steady-state size distributions of bubbles inside a particle suspension resulting from through-flux of bubbles of a single size, for bubble input sizes of 0.1, 0.4, 0.7 and 1 ml. The gray area represents the apparent distribution expected if the bubbles in the suspension are all the input size, based on the 0.1 ml experiment, in which no splitting or coalescence was observed. Bubbles to the left of the distribution are smaller than the input size. Bubbles to the right of the distribution are larger than the input size (not observed inside the suspension). Small bubbles form by splitting of larger bubbles around the particles. Splitting is more likely for larger bubbles, and the number of small bubbles in the suspension increases with bubble input size.

In our single-particle experiments, only bubbles that were smaller than the width of the particle could stagnate beneath it, and stagnation occurred only when the particle was oriented with its flat side down.

When multiple bubbles of the same starting size rise through a particle suspension (Section 2.3. and Figure 3.5.), the concentration of small bubbles generated by bubble breakup increases with increasing bubble input size. This observation lends support to our inference that breakup occurs more frequently for larger bubble:particle size ratios.

From these results we infer that in a particle-rich suspension, the combined effects of small bubble generation by breakup of large bubbles and stagnation of small bubbles beneath particles can produce enrichment of small bubbles relative to larger ones. Even in the absence of particles, the lower rise rates of small bubbles relative to larger ones can drive the relative enrichment of small bubbles in any given volume (e.g. Cashman et al., 1994). Bubbles of all sizes rise more slowly through a suspension than they would in the absence of particles. (See Figure 3.6. for rise rates with and without particles in our experimental setup.) However, only the smallest bubbles stagnate completely inside the suspension. We suggest that vesicle populations in mafic systems where gas flux greatly exceeds magma flux, such as Stromboli volcano, will record an integrated history of both primary vesiculation processes and modifications produced by gas movement relative to the magma.

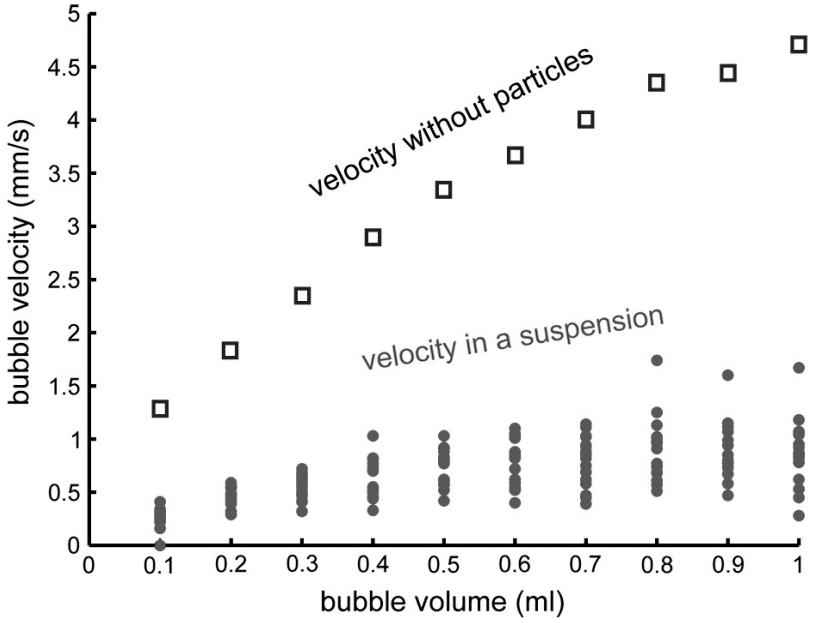

Figure 3.6. Experimentally measured bubble rise velocity versus bubble size. Open squares: average bubble rise velocity in the absence of particles. Gray circles: average rise velocity of bubbles through a ~50 vol% suspension of particles. Bubble velocities of 0 mm/s (some of the 0.1 ml bubbles) represent bubbles that have stagnated beneath particles. All velocities are measured in setup a of Figure 3.1. (see Section 2.1. for details). See Tables 3.1. and 3.2. for equivalent diameters and bubble:particle size ratios.

3. Bubble populations in tephra from Stromboli

To assess the applicability of our experiments to mafic volcanoes, we compare our experimental results to bubble populations within tephra from Stromboli volcano, where gas moves through magma with a crystallinity of ~50% (e.g. Armienti et al., 2007; Métrich et al., 2001), close to the particle concentration in our analogue system. We collected 3 samples from a single explosion during a series of ash-rich eruptions on 19 July 2007. These eruptions represented renewal of normal Strombolian activity after a pause in activity that followed a large eruption on 15 March 2007. At this time,

explosions from the northern crater generated 4-5 ash plumes per hour, with an average height of 100-150m above the vent (http://www.ct.ingv.it/stromboli2007/main.htm). Our samples have vesicle-free crystallinities of ~30-40% by area and crystal-free vesicularities of ~15-60%. Crystals range in size from approximately 50μm to 2mm. Bubbles range in size from approximately 10μm to 3mm, and have complex shapes.

Crystal and bubble size distributions of one sample are shown in Figure 3.7., as determined from binary images created from both digitized thin section and scanning electron microscope (SEM) images. Figure 3.7.a shows the number of bubbles and crystals of different sizes per unit area in the thin section scan. The size of the bubbles is expressed as equivalent diameter d, which is calculated from the area A_b of each bubble as $d = 2\sqrt{(A_b/\pi)}$. The size of the crystals is expressed as equivalent width w, which is calculated from the area A_c of each crystal as $w = \sqrt{(A_c)}$. Since the resolution of the thin section scans is not high enough to analyze the smallest bubbles and crystals, we used SEM images to characterize these. Figure 3.7.b shows analyses (stacked in the histogram) for SEM images of different regions of the thin section in Figure 3.7.a. Microlites are excluded from the crystal population in all these analyses, as they are interpreted to have crystallized rapidly on or immediately prior to eruption, and thus would not have been present in the magma to influence bubble migration.

The bubble and crystal size distributions in each image are similar, indicating that coexisting bubble and crystal populations are similar on both scales and across the range of different textures represented by the SEM images. Although the absolute bubble and crystal size ranges overlap, the bubble distribution in most cases has a broader peak, which is shifted to larger sizes relative to the peak in the crystal distribution and could

indicate modest bubble expansion on eruption. This is consistent with conclusions drawn from a comparison of dimensionless parameters in our experiments and in magma (Section 4), as well as with observations of bubble shapes.

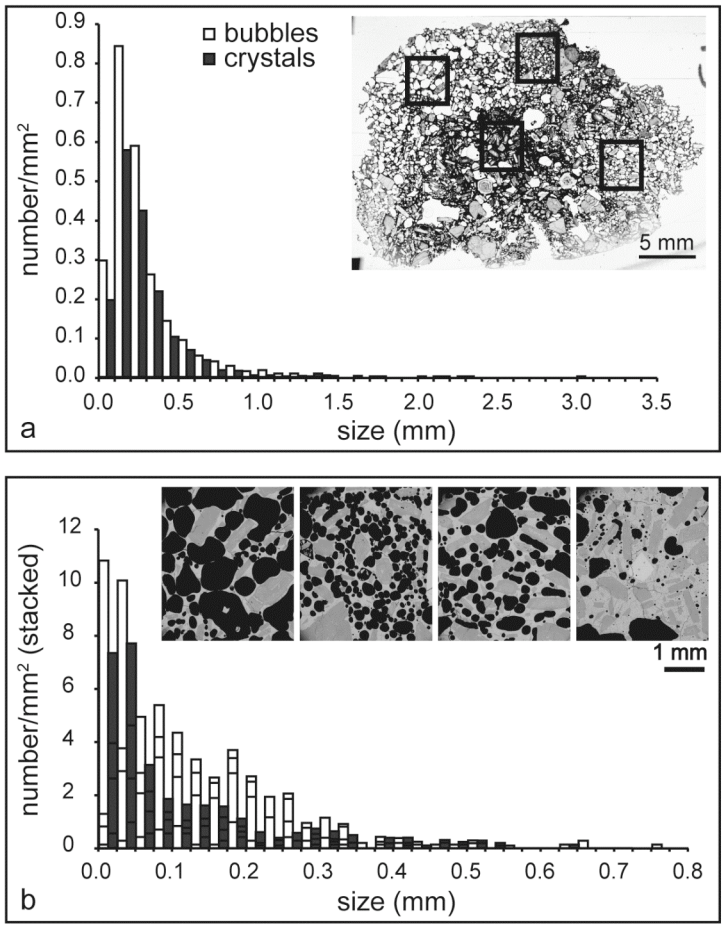

Figure 3.7. Bubble and crystal size distributions (normalized to total area of melt+crystals+bubbles) in a thin section scan (a) and on 39x magnification SEM images from the same thin section (b). The analyses for the SEM images are stacked in the histogram (b), with the analysis for the leftmost image on the bottom and the analysis for the righthand image on the top. The location of the SEM images in the thin section scan is shown by the black boxes. Bubble size is calculated from the area A_b as $d = 2\sqrt{(A_b/\pi)}$. Crystal size is calculated from the area A_c as $w = \sqrt{(A_c)}$. The y-axis indicates the number of bubbles or crystals of a certain size present per area unit of the analyzed image. The SEM images represent areas with different textures present within the thin section scan (locations shown by black boxes). Note that bubbles appear white on the thin section image and black on the SEM images.

Figure 3.8. shows SEM images of representative areas in our samples, illustrating the wide variety of bubble shapes and relationships of bubbles to crystals observed in these samples. Figure 3.8.a shows recently coalesced bubbles, which are readily identified by cusps that remain unretracted (white arrows). Since the bubble walls have not relaxed to a rounded shape, we assume that these bubbles coalesced upon eruption due to expansion, and the bubbles did not have time to relax before the sample quenched (that is, these bubbles were present as separate, un-coalesced, bubbles in the magma before eruption). Figure 3.8.b shows a bubble (marked by a gray x) that is deformed but does not have angular cusps and is not clearly bounded by crystals. Assuming its shape was not significantly modified on eruption, this bubble could have formed by coalescence of smaller bubbles in the volcanic conduit, leaving enough time for the cusps to retract but not enough time for the bubbles to relax completely back to spherical. Figures 3.8.c and d show bubbles (marked by a white x) that are deformed and fill the space between crystals (6c) or are bent around crystals (6d). In light of our experimental results, we interpret these as having deformed because of the crystals. In fact, they are close to the size of the phenocrysts ($\psi \sim 1$). The rest of the bubble population in these samples consists of small (i.e. $\psi << 1$), usually spherical bubbles. Our experiments indicate that small spherical bubbles, which are often interpreted to have formed during a late stage of nucleation, could also have been formed by splitting of larger bubbles. These small bubbles are then enriched in the system relative to larger ones because of their slower rise velocity and tendency to stagnate beneath the particles. Figure 3.9. shows additional examples of deformed bubbles in SEM images.

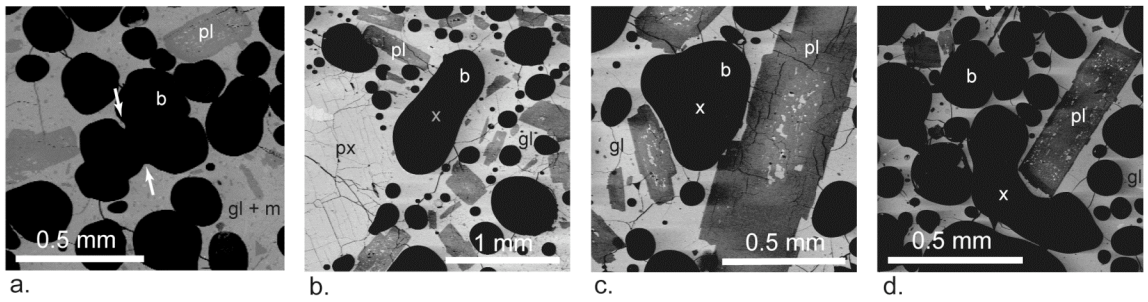

Figure 3.8. SEM (scanning electron microscope) images of tephra from Stromboli volcano. b = bubble; pl = plagioclase crystal; px = pyroxene crystal; m = microlites; gl = glass. See text for discussion.

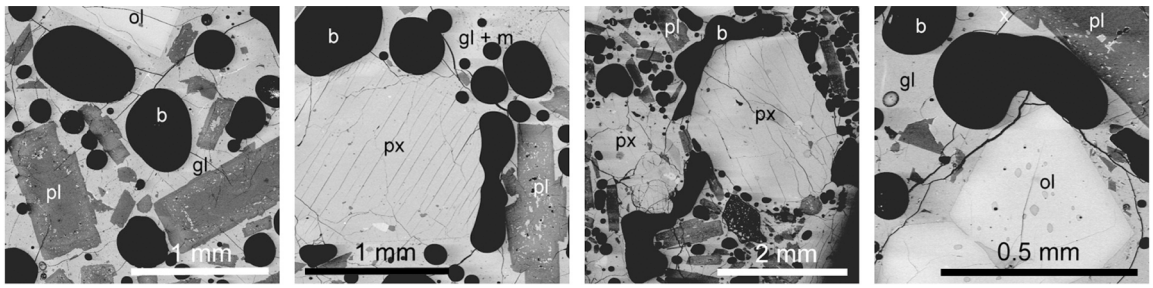

Figure 3.9. SEM (scanning electron microscope) images of tephra from Stromboli volcano. b = bubble; pl = plagioclase crystal; ol = olivine crystal; px = pyroxene crystal; m = microlites; gl = glass. Additional examples of bubble shapes in tephra. See text with Figure 3.8. for discussion.

These results show that bubble populations in our experimental system and in Stromboli tephra compare qualitatively. To make a better comparison of the two systems, we use dimensional analysis.

4. Comparison of experimental and volcanic conditions

Table 3.1. compares fluid properties in our experiments and in natural systems. Both viscosity and surface tension are higher in magmatic systems than in our experiments. Higher viscosity implies that both bubble rise and the rate of liquid drainage out of thin films between bubbles or a bubble and a crystal will be slower, increasing time scales for gas movement, bubble splitting and coalescence. Higher surface tension between the bubble and the liquid means that bubbles will be less deformable, and we consequently expect less bubble deformation and breakup in magma than in our analogue experiments. As noted above, wetting angles between bubbles and particles in our experimental system are small; a thin layer of glass is also present between bubbles and crystals in our thin section images, indicating that the liquid preferentially wets the particles in both systems.

Table 3.2. compares our experimental system and Stromboli magma in terms of bubble and particle sizes and the ratios of forces acting on the bubbles. The size ratio ψ of bubble to particle widths in our experiments falls within the range found in the 2007 Stromboli samples. Note that bubble and particle widths are calculated from three-dimensional data in our experiments whereas they are calculated from two-dimensional bubble and crystal areas observed in Stromboli thin sections, and that we use only the most abundant bubble and crystal sizes occurring in the tephra in our comparison. Bubbles for which $\psi<0.3$ do exist at Stromboli but are always spherical. Since we are making a comparison with experiments in which all bubbles except the smallest ones deform, we can justify neglecting these smallest size classes. Large bubbles in Stromboli

samples deform primarily around larger crystals. The abundance of large bubbles and crystals decreases rapidly with size (Figure 3.7.a) and for the sake of comparison we ignore this larger tail to the distribution as well.

The other dimensionless parameters shown in Table 3.2. measure the relative importance of buoyancy, inertia forces, viscous forces and surface tension forces acting on the bubbles. Velocities used to calculate Re and We are measured for our experiments (particle free) and calculated using Stokes flow ($u = r^2\rho g / 3\eta$) for Stromboli magma. The values of the Reynolds number Re, which describes the ratio of inertial forces to viscous forces, and the Weber number We, which is the ratio of inertia to surface tension, show that inertial forces are unimportant in both our experiments and in magmatic systems.

If we compare buoyancy to surface tension forces (the Bond number B), we see that buoyancy dominates slightly in our experiments ($B>1$) but that surface tension clearly dominates in magma ($B<<1$). This means that bubbles rising freely in the liquid will deform more easily in our setup, whereas we expect that freely rising bubbles in magma will be spherical unless they are very large. The capillary number Ca, which is the ratio of viscous forces to surface tension forces (note that $Ca = We/Re$), is similar in magnitude to the Bond number. This can be expected based on the fact that inertia forces are small in both systems and buoyancy forces and viscous forces therefore balance each other. In our experiments $Ca \approx 1$, indicating that both viscous and surface tension forces are important. Ca increases with bubble size, and this is reflected in our observation that larger bubbles deform more than smaller ones. Surface tension is more important in Stromboli magma, where $Ca<<1$, and we therefore expect bubbles to deform less easily in magma than in our experimental setup.

	definition	Analogue (light syrup)	Stromboli
ψ	d/w	0.8-1.8	0.3-3
Re	$\rho ru/\eta$	0.0053-0.036	10^{-11}-10^{-9}
We	$\rho ru^2/\sigma$	0.002-0.038	10^{-15}-10^{-12}
B	$\rho gr^2/\sigma$	1.5-7.0	10^{-5}-10^{-2}
Ca	$\eta u/\sigma$	0.33-1.06	10^{-5}-10^{-3}

Table 3.2. Comparison of dimensionless parameters for our analogue system and Stromboli magma. d, w, ρ, η, σ: see Table 1; g: acceleration of gravity; r: bubble radius (d/2); u: bubble velocity. See text for discussion.

From this comparison, we infer that most of the bubble deformation observed in our tephra samples probably results from bubble expansion caused by rapid decompression on eruption, hindered by crystals present in the magma, rather than during bubble rise prior to eruption. The bubble marked by an x in Figure 3.8.c, for example, could have been spherical and positioned centrally between the three crystals, and could then have expanded outwards against the crystals on eruption. In this case, the observed deformation would indicate restricted lateral crystal movement, consistent with the high crystallinity and rapid magma quenching. In some cases, however, the observed bubble deformation appears too extensive to result entirely from crystal-hindered expansion. The bubble marked by an x in Figure 3.8.d, for example, could presumably have expanded more easily into the now glassy area towards the bottom of the figure instead of deforming around the plagioclase crystal. Bubble textures such as these suggest that, although most of the deformation probably happened on eruption, some could have happened in the conduit by processes similar to those in our experiments, although over longer time scales. We expect that, even though the deformability of bubbles is small in

magma, some bubbles are rising through the magma and deforming, as discussed in the next section.

5. The role of gas in Strombolian eruptions

5.1. Gas migration through magma

Bubbles seen in tephra from Stromboli either nucleated in situ or migrated to their current location from deeper in the magmatic system. As the gas flux far exceeds the amount of magma ejected (Harris and Ripepe, 2007), a large volume of gas has to pass through the upper part of the magma column with only minimal entrainment of the magma. Several conceptual models exist for how this gas moves through. For example, Burton et al. (2007) suggest that permeable pathways may begin to develop at several km depth and enable gas to be transported directly to the surface. In this model, small bubbles result from late-stage nucleation, and deformed bubbles result from coalescence that ultimately produces a 3D permeable network all the way through the crystal-rich magma. Lautze and Houghton (2006) assume that small spherical bubbles result from late-stage nucleation, and larger deformed bubbles result from coalescence of smaller bubbles. They notice that these larger bubbles can be aligned along boundaries between parts of their samples with different textures and conclude that these bubbles may be able to migrate through the melt phase. They also hypothesize that mixing of the different magmas represented by the different textures in their samples is aided by migration of small bubbles from one magma to the other. In all models, some gas is expelled as large

gas slugs during Strombolian eruptions. These bubbles, which are several orders of magnitude larger than the crystals, will have to push the liquid-crystal mixture aside to rise through. The effect of crystals in this case will be to increase the effective viscosity of the mixture relative to the viscosity of the liquid phase alone. Such large bubbles cannot be studied from eruptive products as they are larger than the tephra or pumice clasts and are therefore not preserved in the samples. Here, we study the effect of crystals on bubbles that are similar in size to the crystals, such as those found in thin sections from Stromboli (e.g. Figure 3.7.).

If bubbles are small and if the crystal concentration is high, which is the case for the bubble populations preserved in Stromboli tephra, bubbles rise primarily by displacing the liquid rather than the liquid-crystal mixture. In this case, the viscosity to consider is the actual liquid viscosity rather than the effective viscosity of the mixture. Because the crystals occupy space that is unavailable for the bubbles to move into, bubbles must deform or not move at all. At Stromboli, passive degassing is widespread, indicating that gas is percolating through the crystal-rich system. Unless permeable networks are formed all the way down through the crystal-rich magma, some bubbles will have to migrate through the system, and, if they are larger than the size of the pores between the crystals, these will have to deform to move through. Persistent percolating pathways are most likely to occur in shallow crystal-rich magma, which approaches conditions of porous media flow. The discrete nature of the active degassing (puffing) activity at Stromboli implies that permeable pathways may not stay open continuously, even at shallow depth. We envisage a model in which a transient permeable network may exist in the very upper part of the conduit (the opening and closing of which may give

rise to puffing activity), but gas percolating through the deeper regions must be rising as bubbles. In addition, we expect that small bubbles will accumulate in near-surface, crystal-rich magma. This may explain the anomalously high small bubble population in Stromboli scoria compared to its low mass eruption rate (Mastin, 1997 and Figure 16 in Houghton and Gonnermann, 2008).

5.2. Bubble populations as a proxy for gas flux

We have shown that bubble populations are influenced by particles in suspensions with high concentrations of solids. Splitting of large bubbles around particles causes enrichment of small bubbles at the expense of larger ones in our experiments, although this effect might not be as important in magmatic systems, where bubbles deform less easily. Trapping of small bubbles by particles will also increase the number of small bubbles in the suspension. Chemical engineering experiments show that gas holdup increases with increasing gas flux, even in the absence of particles (e.g. Aslan et al., 2006). An increase in gas holdup can be manifested as an increase in bubble size or an increase in the number of bubbles present at any one level in the system. We use literature data to demonstrate the linkage between gas flux and explosivity at Stromboli volcano and investigate how bubble size distribution data might contribute to understanding the role of gas flux in light of our analogue experiments.

As discussed above, at Stromboli, three types of gas-driven activity occur simultaneously: Strombolian eruptions, active degassing (puffing) and passive degassing. As gas flux far exceeds magma flux, we can conclude that gas flux is the main factor

driving normal activity. Ripepe et al. (2002) distinguish two phases of explosive degassing with different intensities, based on thermal and infrasonic data. During higher-intensity phases, Strombolian explosions are frequent and puffing is rapid but individual puffs are short. During lower-intensity phases, Strombolian explosion frequencies are lower and puffs are longer but less frequent. Different delay times between infrasonic and thermal signals during these two phases indicate higher gas jet velocities and/or elevated magma free surface levels during the higher-intensity phases.

Volcanic clasts are formed during gas-driven, normal Strombolian activity when fragments of magma are expelled by gas bubbles as they burst at the magma free surface. Ripepe et al. (2002; 2008) report correlations between the frequency of explosions, the gas jet velocity, and the magma free surface level. Ripepe et al. (2008) interpret these correlations to reflect changes in gas flux into the shallow system. Addition of gas into the shallow system would raise the level of the magma free surface in the conduit. Changes in eruption frequency (and resulting mass ejection rates) would reflect this increase in gas flux (e.g. Chadwick et al., 2008). This model could be tested by examining bubble populations in tephra erupted during periods of different eruptive intensity. Tephra erupted during periods of high gas supply rate should record an increase in gas holdup in the system, similar to the change in gas holdup with gas flux observed in chemical engineering studies (e.g. Aslan et al., 2006).

The only published study that provides detailed data on bubble populations in tephra as a function of eruption intensity is that of Colò et al. (2010), who show that bubble number densities vary inversely with infrasonic amplitude (a measure of eruptive intensity). These data are interesting as this trend is the opposite of that predicted by

vesiculation models, where an increase in eruption intensity would be expected to cause an increase in the effective pressure driving vesiculation, which in turn should increase rates of bubble nucleation over bubble growth (e.g. Mastin et al., 2004). Colò et al. (2010) explain this relationship by suggesting that higher gas contents in the rising magma would allow more efficient coalescence and hence larger and more frequent explosions. They do not address the source of changing gas contents within the column, nor do they report the bulk vesicularity of the samples, which would be the most direct measure of gas holdup. Since gas holdup should increase with increasing gas flux, finding a proxy for gas holdup in volcanic samples would allow us to extract information on the gas flux at the time the samples were erupted, unless other factors, unrelated to gas flux, also affect holdup.

Factors that might affect gas holdup in the absence of a change in gas flux are crystal concentration and crystal size. Our experiments suggest that an increase in crystal concentration could facilitate trapping of small bubbles within the suspension and thus increase gas holdup. Likewise, increasing crystal size might enable larger bubbles to stagnate, and increase gas holdup. However, crystal size distributions for Stromboli tephra (Armienti et al., 2007; Cigolini et al., 2008) show no obvious correlation between vesicularity and crystal concentration or number-referenced dominant crystal size (both calculated from crystal size distributions according to Cashman and McConnell, 2005). Thus it appears that changes in the bubble population with eruptive intensity at Stromboli must be explained either by changes in bubble nucleation and growth rates (Ripepe et al., 2002) or by changes in gas flux from depth (Ripepe et al., 2008; implied by Colò et al., 2010). Our data support the latter interpretation, and suggest that the high crystallinity of

the shallow Stromboli magma plays a critical role in modulating gas flux through the system. Gas flux is an important parameter driving volcanic eruptions. Establishing links between gas flux and bubble populations could provide a way of tracking changes in gas flux in crystal-rich systems through their deposits and improve our understanding of the mechanisms of gas migration that give rise to passive degassing.

6. Conclusions

We have performed analogue experiments to determine the effect of solid particles on bubble shapes and sizes as they rise through a suspension with high (~50%) solids concentration, and have used our experimental results to interpret bubble populations in crystal-rich tephra from Stromboli volcano, Italy. We find that particles can cause bubbles to deform and split, providing alternative interpretations to coalescence and late-stage nucleation (e.g. Lautze and Houghton, 2006; Polacci et al., 2006a; Shimano and Nakada, 2006) for large deformed bubbles and small spherical bubbles observed in crystal-rich tephras. Relative enrichment of small bubbles due to trapping within particle-rich suspensions implies that bubble number densities may not be direct representations of bubble nucleation rates in crystalline magmas. Instead, bubble splitting around particles could increase the relative abundance of small bubbles in the system, as could accumulation of small bubbles within the magma because of trapping. A comparison of the relative importance of the forces acting on the bubbles in our experiments and in Stromboli magma indicates that most of the bubble deformation observed in tephra probably results from bubble expansion on eruption, although bubble

textures (e.g. Figure 3.8.d) suggest that some deformation occurred in the magma prior to eruption.

Other low viscosity, crystal-rich magmas to which our experimental results could be applied include Mount Etna, Italy (where Polacci et al., 2006b, report vesicle-free phenocryst crystallinities of 25-40%) and Villarrica, Chile (where Gurioli et al., 2008, report vesicle-free phenocryst crystallinities up to 56.4%). In addition to volcanic systems, our experiments may provide useful insights into mechanisms of gas transport in other particle-rich systems, such as crystallizing plutons and marine sediments.

7. Bridge

In the previous chapter, I have investigated the influence of crystals on the shapes and sizes of bubbles observed in tephra from Stromboli volcano. Most importantly, I have shown that small bubbles become enriched in crystal-rich systems due to both splitting of large bubbles around the crystals and trapping of small bubbles underneath crystals. Bubble splitting, and thus small bubble accumulation, increases with increasing gas flux, so that bubble number densities should increase with gas flux. This trend is opposite from that observed by Colò et al. (2010), who show that bubble number densities decrease with increasing eruptive intensity and attribute this to an increase in coalescence during periods of increased gas flow. I have shown in Chapter II that vesicularities in tephra samples from Stromboli locally decrease with crystallinity, but are overall higher during higher intensity ("major") explosions. The implications of Colò et al. (2010)'s and my data for degassing at Stromboli are discussed in Chapter V. In the

following chapter (Chapter IV), I make a brief detour to focus on rise velocities of small bubbles moving through Stromboli's crystal-rich magma. I take an approach motivated by the treatment of reservoir rocks in hydrology and the petroleum industry, and treat the crystal-rich magma as a porous medium through which I model bubble rise velocities. Although I have shown in Chapter III that the bubble population observed in tephra may not be directly representative of the bubble population at depth, I start by modeling the rise of bubbles with this measured size distribution through the crystal-rich magma. I then use literature data for the non-eruptive degassing flux at Stromboli to calculate the dominant bubble size necessary to account for the measured fluxes. In Chapter V I tie these results back to my findings from Chapters II and III and formulate a new model for the Strombolian eruption mechanism that takes the crystallinity in the upper magma into account.

CHAPTER IV

THE RISE SPEED OF A BUBBLE THROUGH A VISCOUS LIQUID IN A NARROW TUBE AND APPLICATION TO BUBBLE PERCOLATION THROUGH CRYSTAL-RICH MAGMA AT STROMBOLI

This work is co-authored by committee members Drs. Alan Rempel and Katharine Cashman, and is being prepared for submission to Earth and Planetary Science Letters. All the work was done by me. Drs. Rempel and Cashman advised me on this project.

1. Introduction

Fluid migration through porous media occurs in many geological systems. Some important examples are groundwater flow, the migration of hydrocarbons from source area to reservoir, methane migration through seafloor sediments, volatile escape from crystallizing plutons and hydrothermal fluid migration through fractured rock. In volcanic systems, gas bubbles sometimes migrate through crystal-rich magmas. A notable example is Stromboli volcano in Italy, where the upper plumbing system contains magma with a phenocryst concentration of 45-55 vol.% (e.g. Métrich et al., 2001; Landi et al., 2004). Degassing is abundant at this volcano and 90% of the escaping gas is non-eruptive (Harris and Ripepe, 2007), indicating that the gas apparently migrates through an essentially static crystal-rich system. Chemical signatures of the escaping gasses have been used to derive depths of degassing and degassing mode (open vs. closed system), as

well as gas fluxes and degassed magma volumes (e.g. Allard et al., 1994; Burton et al., 2007b; Aiuppa et al., 2010), but the physical mechanism of gas migration through the magma remains unclear. The development of permeable networks through the crystal-rich magma has been proposed as a method of gas migration (Burton et al., 2007; Polacci et al., 2008). Crystal-rich tephra erupted at Stromboli is vesicular, however (~35-70% of the space between the crystals is gas), indicating that large quantities of gas may be migrating through the magma in the form of bubbles (see also Belien et al., 2010 (Chapter III)). The migration of gas bubbles through crystal-rich magma is the focus of the current study.

In sedimentary systems the fluid phase is generally connected, and its migration through the pore space can be modeled with (multiphase) Darcy flow, flow path analysis, or invasion-percolation, all methods widely used in the petroleum industry (see e.g. Hantschel and Kauerauf, 2009, for an overview). The pore space itself can be approximated as a bundle of capillary tubes. When there is more than one fluid phase present, e.g. water and air in the vadose zone, water, oil, and/or gas in petroleum reservoirs, water and steam in geothermal systems, and liquid magma and gas in volcanic magma chambers and conduits, we can consider a buoyant fluid phase rising through a surrounding liquid that fills the pore space. For gas bubbles rising through magma, the buoyant fluid phase is not connected, and migration velocities and gas fluxes in this case differ from those of a connected fluid because the buoyancy pressure that drives flow is much smaller than for a large connected fluid column.

To address the specific problem of bubble rise through crystal-rich magma, we develop a new migration model based on the rise of individual bubbles through a porous

medium with a viscous surrounding liquid. We model the medium as a network of narrow tubes. In the first part of this study, we use analogue experiments to investigate the rise velocity of bubbles in narrow tubes in two situations: 1) the tube is partially submerged in the liquid so that bubble rise is limited by flow through the liquid film between the bubble and the tube walls (assuming the height of the liquid in the tube reaches a steady state), and 2) the tube is fully submerged in liquid and the liquid phase can flow freely from one end to the other around the outside of the tube. An extensive body of literature exists on the case where bubble rise is limited by film flow (similar to situation 1); in fact, the flow of long bubbles in capillaries that are sealed on one end forms the basis for many models of bubble flow through porous media (e.g. Wooding and Morel-Seytoux, 1976; Olbricht, 1996; Stark and Manga, 2000). We show, however, that bubble rise velocities are markedly different when the tube is fully submerged and argue that this case is more applicable to bubble percolation through fluid-saturated porous media.

In the second part of this study, we develop a MATLAB® (The MathWorks, Natick, MA, USA) numerical model for gas migration through a network of tubes, using an empirical relationship between our experimental rise velocities in fully submerged tubes (for which no literature predictions exist) and a literature prediction for velocities in sealed tubes. We use bubble size, crystal spacing and crystal length distributions measured on thin sections of tephra from Stromboli volcano, Italy, to represent bubble sizes, tube widths and tube lengths in our model, and use it to calculate gas velocities in Stromboli's crystal-rich magma. We combine our modeling results with gas fluxes measured at Stromboli and vesicularities from our tephra samples to draw inferences

about the pre-eruptive bubble population in the magma and the mechanism of gas migration at this volcano.

2. Background

For modeling purposes, porous media are often treated as a bundle of (usually cylindrical) capillary tubes. The tubes represent the pore space, and the area between them represents the solid portion of the medium (e.g. sand grains in a sandstone or, in our case, crystals in magma). In the simplest case, all tubes are parallel, vertical and have the same radius R and length L. If a single, connected fluid phase is present in the pore space, its discharge velocity can be described with Darcy's law ($Q_{linear} = -\frac{k}{\mu}\nabla P$, where Q_{linear} is the linear fluid flux (m/s), k is the permeability of the porous medium (m^2), μ is the fluid dynamic viscosity (Pa s), and ∇P = pressure gradient driving fluid flow (Pa/m)). Darcy's law is widely used in hydrology to describe groundwater flow. If the fluids are immiscible, this model can be extended to multi-phase fluid flow by including the relative permeabilities of the separate phases, as long as each phase is internally connected (no bubbles). Multi-phase Darcy flow models are used in the petroleum industry to describe flow to production wells; they can also be used to model hydrocarbon migration in the subsurface on geological timescales, although these models are computationally intensive (Hantschel and Kauerauf, 2009).

Instead of considering a bundle of capillary tubes with equal radii, we can also think of the pore space in a porous medium as a network of intersecting capillary tubes with different radii, or as a network of pores with large radius, connected by narrower

pore throats. When the geometry of all capillary tubes or pores is heterogeneous, a rising liquid follows a path through the porous medium that depends on the balance between its buoyancy pressure and the capillary pressure of the tubes. Capillary pressure P_c is the pressure difference across the interface between two immiscible fluids in a capillary. If the capillary is cylindrical, then $P_c = \frac{2\sigma}{R}\cos\alpha$, where σ is the interfacial tension between the two fluids (N/m), α is the contact angle between the two fluids and the solid (tube), and R is the tube radius (m). The displacing fluid can rise in a capillary tube when its buoyancy pressure becomes larger than the capillary pressure: $\Delta\rho gl > \frac{2\sigma}{R}\cos\alpha$, where $\Delta\rho$ is the density contrast between the two fluids (kg/m^3), g is the acceleration of gravity (m/s^2) and l is the height of the displacing liquid column. When buoyancy pressure equals capillary pressure, the interface between the two fluids will not move and the displacing fluid will not advance. A modeling technique that is widely used in the petroleum industry, and is based on this pressure balance, is the invasion-percolation method. In this method, the porous medium is modeled on a grid as a series of nodes or bonds that represent pores or pore throats, each with its own capillary pressure. The displacing fluid phase starts at the bottom of the grid and enters adjacent nodes or bonds when the buoyancy pressure overcomes the appropriate capillary pressure. Since P_c is smallest for the largest nodes, the fluid will enter these first. In this way, the interface advances until it reaches the top of the grid, at which point the fluid has percolated all the way through the porous medium. If the buoyancy pressure of the fluid is not sufficient to overcome the capillary pressure, it will not be able to percolate all the way through the volume. The pressure necessary for the fluid to find a connected pathway through the volume is called

the threshold pressure P_{th}. The pressure necessary for significant fluid entry into the pore space is called the capillary entry pressure. Both can be inferred from mercury injection capillary pressure (MICP) analysis of rock samples.

Models describing the migration of individual bubbles in porous media, rather than a connected fluid, are typically based on the motion of long (Taylor) bubbles in tubes (e.g. Wooding and Morel-Seytoux, 1976; Olbricht, 1996; Stark and Manga, 2000). The velocity of Taylor bubbles can be calculated in one of three ways. The first approach is to solve the Navier-Stokes equations numerically, while tracking the bubble interface (e.g. Taha and Cui, 2004; Feng, 2008; Kang et al., 2010). These models are useful for exploring a wide range of parameter space but are computationally intensive. The second approach is to derive analytical relationships between velocity and key parameters controlling bubble rise (e.g. buoyancy, viscosity and surface tension) (e.g. Harmathy, 1960; Marchessault and Mason, 1960; Bretherton, 1961; Bendiksen, 1985). These relationships are typically valid only for a specific range of conditions, as they require simplifying assumptions and approximations, and are usually validated against physical experiments. Finally, experimental data can be used to derive empirical relationships between velocity and parameters controlling bubble rise (e.g. Viana et al., 2003; Liu et al., 2005).

A common characteristic of all these studies is that – unless the surrounding liquid has a non-zero flow rate – the modeled tubes are assumed to be sealed on one end, so that bubble rise is controlled by the rate of liquid return flow through the thin liquid film between the bubble and tube walls. However, this situation might not be applicable to porous media with pore space that is connected in multiple directions. In such media,

the liquid displaced by the rising bubble can flow freely around the particles and is therefore not restricted to downward flow in the liquid film.

We use our findings on bubble rise in tubes to develop a numerical model to predict bubble rise velocities in natural systems. Our ultimate goal is to estimate bubble velocities through the crystal-rich magma at Stromboli volcano, where gas flows through an essentially stagnant, crystal-rich, magma in the upper plumbing system. At this volcano, three methods of degassing are distinguished. Gas release during Strombolian eruptions accounts for ~10% of total gas escape (Harris and Ripepe, 2007) and is modeled as the rise of a large Taylor bubble (slug) through the volcanic conduit and its bursting at the free magma surface (see Chapter II, section 2.2.). Active and passive degassing each account for half of the remaining gas (Harris and Ripepe, 2007). Active degassing, also called puffing, consists of rhythmic gas bursts from the vents; puffing occurs every ~2 s and is not usually accompanied by eruption of volcanic material. It is explained as bubby flow in the conduit, with bubbles slightly smaller than the slugs involved in Strombolian eruptions (Ripepe et al., 2002; Ripepe et al., 2007; Harris and Ripepe, 2007). Passive degassing has been proposed to occur through the development of permeable networks in the crystal-rich magma (Polacci et al., 2008), an interpretation based on the observation of long, deformed bubbles in erupted tephra. Since numerous bubbles are preserved in erupted clasts, and since the connected bubble pathways imaged by Polacci et al. (2008) are unlikely to be present at depth within the conduit, we propose that passive degassing might occur directly by the rise of these bubbles through the magma. We model rise velocities of these bubbles and compare our results to measurements of the non-eruptive degassing flux at Stromboli.

3. Experimental methods

To determine bubble rise velocities through crystal-rich liquids, we first explore bubble rise through viscous fluid within narrow tubes. We measure the rise velocities of bubbles both in partially submerged tubes, where the top end extends above the free liquid level so that liquid return flow can only occur through the liquid film between the bubble and the tube wall, and in fully submerged tubes, where the liquid pushed out of the tube by the rising bubble can flow around the outside of the tube back into its base (Figure 4.1.). The bubbles in our experiments are nonwetting, such that a liquid film always separates the bubble from the tube. The tubes are vertical, and the surrounding liquid moves only due to buoyant bubble rise through the tube. We use both light Karo corn syrup (density 1320 kg/m^3; viscosity 4.12 Pa s; air-liquid surface tension 0.071 N/m) and glycerin (density 1261 kg/m^3; viscosity 1.41 Pa s; air-liquid surface tension 0.063 N/m) as the surrounding liquids, although we focus our discussion on the Karo syrup experiments, and use the glycerin to validate our results. The internal tube diameters are 1/8, 2/8, 3/8 and 4/8 inch (3.2, 6.35, 9.5 and 12.7 mm). The tubes are 20 cm in length, with the bottom end placed 1 cm above the base of the tank. The top of the partially submerged tubes extends 3 cm above the liquid level, which is 18 cm above the base of the tank. The top of the fully submerged tubes is 2 cm below the liquid height of 23 cm. In all experiments, a single air bubble is injected with a syringe into the base of the tube. Bubble volumes are varied between 0.1 and 1 ml in increments of 0.1 ml, covering a range of bubble equivalent radius (R_{eq}) / tube radius (R) between 0.45 and 3.9. We measure the velocity of the bubble over 5 cm increments, as it rises in the tube.

Experiments were performed at least three times for each bubble size – tube size combination. Because the very slow rise velocities in the narrowest tubes require slower bubble injection than we can attain with our current equipment, measurements for partially submerged tubes were made only in the three widest tubes. Bubble rise velocities are measured between 5 and 10 and 10 and 15 cm in the partially submerged tubes, and between 5 and 10, 10 and 15 and 15 cm and the top of the tube in the fully submerged tubes. The top of the 3/8 inch fully submerged tube was slightly bent, so that we only use measurements between 5 and 15 cm. This is justified because bubble rise velocities in our experiments do not change detectably over the length of the tube.

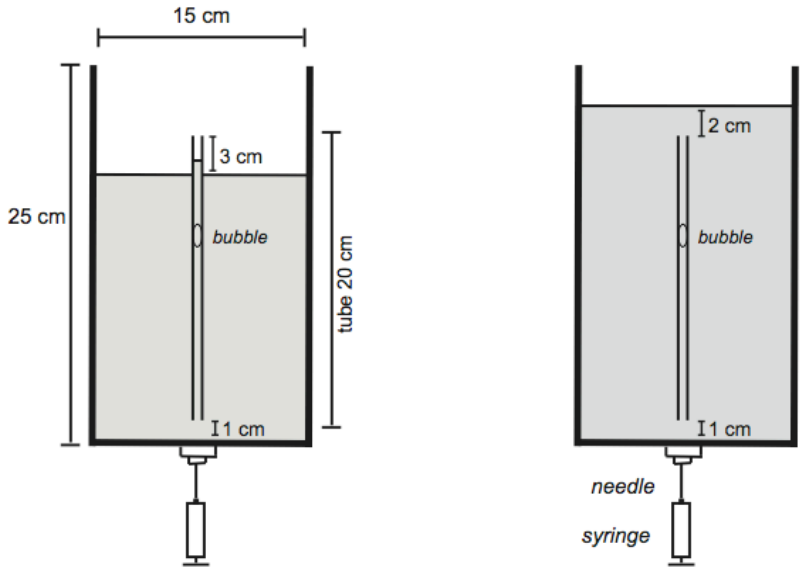

Figure 4.1. Experimental setup used to measure bubble rise velocities in a partially submerged tube (left) and a fully submerged tube (right).

A liquid film is present between the bubble and tube walls in all our experiments. The geometry of the film depends on the bubble geometries, which can be divided into three classes: long bubbles (Taylor bubbles), here defined as $R_{eq}/R > 1.5$, sub-spherical bubbles with $R_{eq}/R < 1$, and transitional bubbles with $1 < R_{eq}/R < 1.5$ (Figure 4.2.). For long bubbles, the film thickness is fairly constant over the entire length of the bubble. For sub-spherical and transitional bubbles the thickness varies from the center to the top and bottom of the bubble.

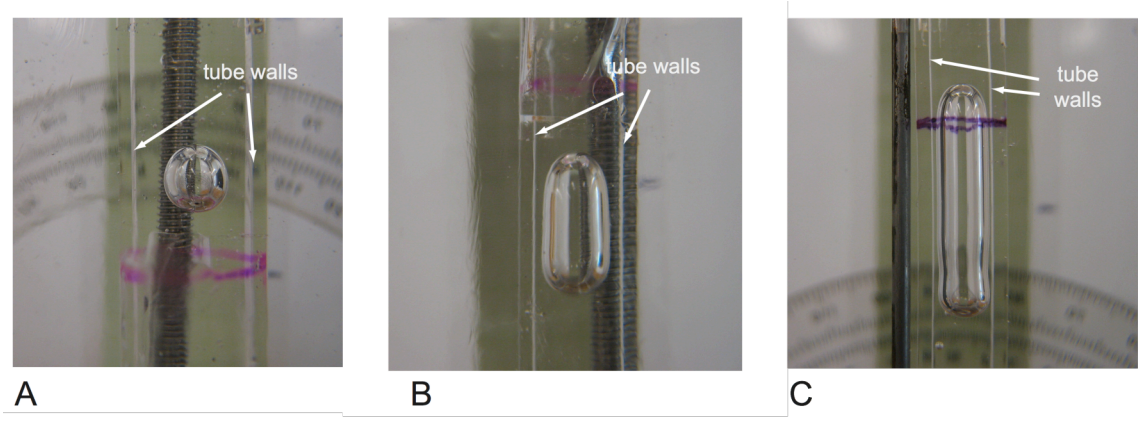

Figure 4.2. Typical examples of (A) a sub-spherical bubble with $R_{eq}/R < 1$, (B) a transitional bubble with $1 < R_{eq}/R < 1.5$ and (C) a Taylor bubble with $R_{eq}/R > 1.5$. White arrows indicate the location of the inner tube walls.

We measured film thicknesses on three separate photographs for each experiment, except in the narrowest tube size, where they were too thin to be measured. Film thicknesses were always measured at the narrowest point. To minimize errors due to refraction, we measured the ratio x of film thickness to tube radius rather than the absolute film thickness. We also estimate the error due to refraction from photographs of

a narrow rod of constant thickness inserted diagonally into the tubes (Figure 4.3.). Distortion is limited to the very end of the rod, close to the walls of the tube. The effect of refraction should be largest in the narrowest tube in which x is measured (2/8 inch diameter), for which we estimate an error of 8% in Karo syrup and 11% in glycerin.

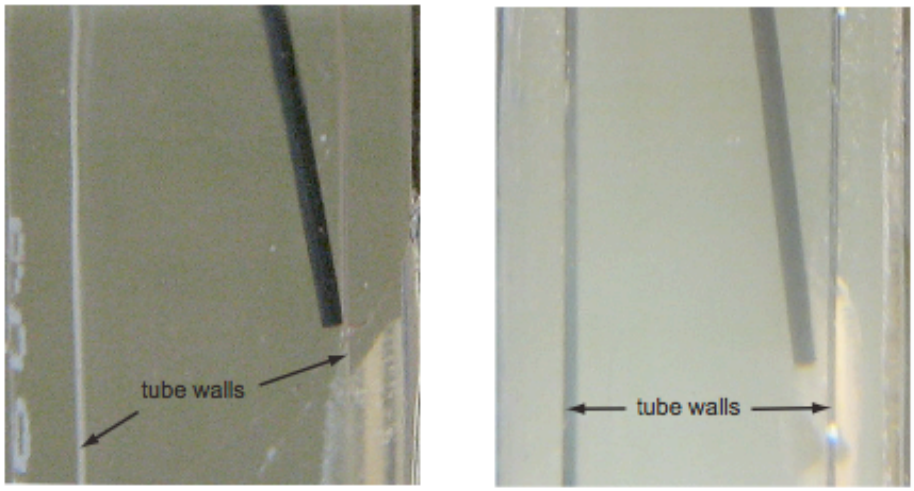

Figure 4.3. Distortion of a 0.5 mm diameter cylindrical rod in a tube with 2/8 inch internal diameter due to light refraction in Karo syrup (left) and glycerin (right).

Other factors contributing to experimental error are changes in liquid viscosity and density due to temperature fluctuations or dehydration (in the case of corn syrup), inaccuracy of height readings due to parallax, and deviations of the tube from vertical. Dehydration was minimized by covering the setup with clingfilm between each experiment. We assume that the temperature dependence of Karo syrup viscosity is similar to that of the more viscous Tate & Lyle's golden syrup, where viscosity varies by ~50% (~100-50 Pa s) and density varies by ~0.2% (1442-1440 kg/m^3) between 18 and 22

^{o}C (our experimental conditions) (Llewellin et al., 2002). Under similar conditions, the viscosity and density of glycerin vary between 1.7 and 1.2 Pa s (~30%) and between 1262 and 1259 kg/m^3 (0.2%) respectively (www.dow.com). Parallax errors were minimized by moving eye level or the height of the camera lens with the bubble to keep the line of sight as close as possible to horizontal. Deviations of the tube from vertical were no more than 2 degrees (~2%). The change of viscosity with temperature is thus by far the largest contributor to experimental variability. Since velocity is generally an inverse function of viscosity, this could introduce a relative error on the velocity measurements of up to ~50% in corn syrup, and ~30% in glycerin.

4. Experimental results

4.1. Partially submerged tubes

In partially submerged tubes, liquid displaced by the rising bubble can either move up, into the subaerial part of the tube, or down through the liquid film between the bubble and tube wall. As the bubble in our experiments is injected into the tube and starts to rise, the displaced liquid initially rises to a level roughly corresponding to the bubble volume. Once this level is reached, the liquid level in the tube stabilizes, indicating that liquid return flow through the film controls bubble rise velocity, similar to the sealed tubes of the literature (section 2). The results of experiments in Karo syrup are summarized in Table 4.1.

Bubble volume (ml)	Avg. velocity (10^{-3} m/s) in partially submerged tubes in corn syrup														
	Tube diameter 2/8”			Tube diameter 3/8”						Tube diameter 4/8”					
0.1	0.08	0.09	0.06	1.40	1.41	1.40	1.05	1.10	1.03	2.92	2.89	2.89	2.59	2.55	2.52
0.2	0.05	0.06	0.06	0.97	0.96	0.96	0.73	0.74	0.76	3.00	2.97	2.96	2.65	2.61	2.58
0.3	0.04	0.05	0.05	0.82	0.83	0.83	0.62	0.62	0.62	2.85	2.84	2.81	2.61	2.47	2.44
0.4	0.05	0.05	0.05	0.83	0.86	0.88	0.63	0.67	0.66	2.80	2.75	2.74	2.44	2.43	2.37
0.5	0.05	0.05	0.05	0.97	0.90	0.91	0.65	0.68	0.67	2.77	2.76	2.74	2.44	2.35	2.42
0.6	0.05	0.05	0.05	0.97	0.92	0.93	0.67	0.66	0.69	2.82	2.81	2.79	2.46	2.37	2.42
0.7	--	--	--	0.97	0.96	0.96	0.69	0.69	0.68	2.89	2.85	2.84	2.43	2.63	2.52
0.8	--	--	--	1.01	1.00	1.00	0.71	0.69	0.71	2.92	2.94	2.91	2.53	2.46	2.58
0.9	--	--	--	0.99	1.05	1.04	0.75	0.75	0.73	3.01	3.01	3.01	2.59	2.57	2.58
1.0	--	--	--	1.07	1.11	1.09	0.76	0.77	0.75	3.14	3.13	3.09	2.65	2.49	2.66

Table 4.1. Bubble rise velocities in partially submerged narrow tubes in light Karo corn syrup. Listed values are averages of measurements between 5 and 10 cm, and 10 and 15 cm. Results are shown for 3 repeat experiments for each bubble size in the 2/8” tube, and for 6 experiments per bubble size in the 3/8 and 4/8” tubes.

Rise velocities are shown in Figure 4.4. Tube-filling (Taylor) bubbles are shown in black, transitional bubbles are shown in gray, and (sub)spherical bubbles are shown as open symbols. Experiments in the 2/8, 3/8 and 4/8 inch tubes are shown as diamonds, triangles and squares respectively. Rise velocities of tube-filling bubbles ($R_{eq}/R > 1$) in each tube remain relatively constant with bubble size. As anticipated, the velocity of smaller bubbles decreases as R_{eq} approaches R.

The dimensionless film thickness x (defined as absolute film thickness / R) is reported in Table 4.2. and shown in Figure 4.5. x decreases with bubble size when $R_{eq}/R < 1$; x remains constant for $R_{eq}/R > 1$ at a value that increases with increasing tube radius.

Bubble vol. (ml)	Dimensionless film thickness x		
	2/8" tube	3/8" tube	4/8" tube
0.1	0.158	0.382	0.545
0.2	0.163	0.283	0.450
0.3	0.158	0.261	0.425
0.4	0.133	0.258	0.364
0.5	0.148	0.239	0.336
0.6	0.142	0.249	0.326
0.7	--	0.243	0.324
0.8	--	0.223	0.324
0.9	--	0.235	0.317
1.0	--	0.243	0.306

Table 4.2. Measurements of film thickness expressed as a fraction x of the tube radius in Karo syrup in partially submerged tubes with diameter 2/8, 3/8 and 4/8 inch.

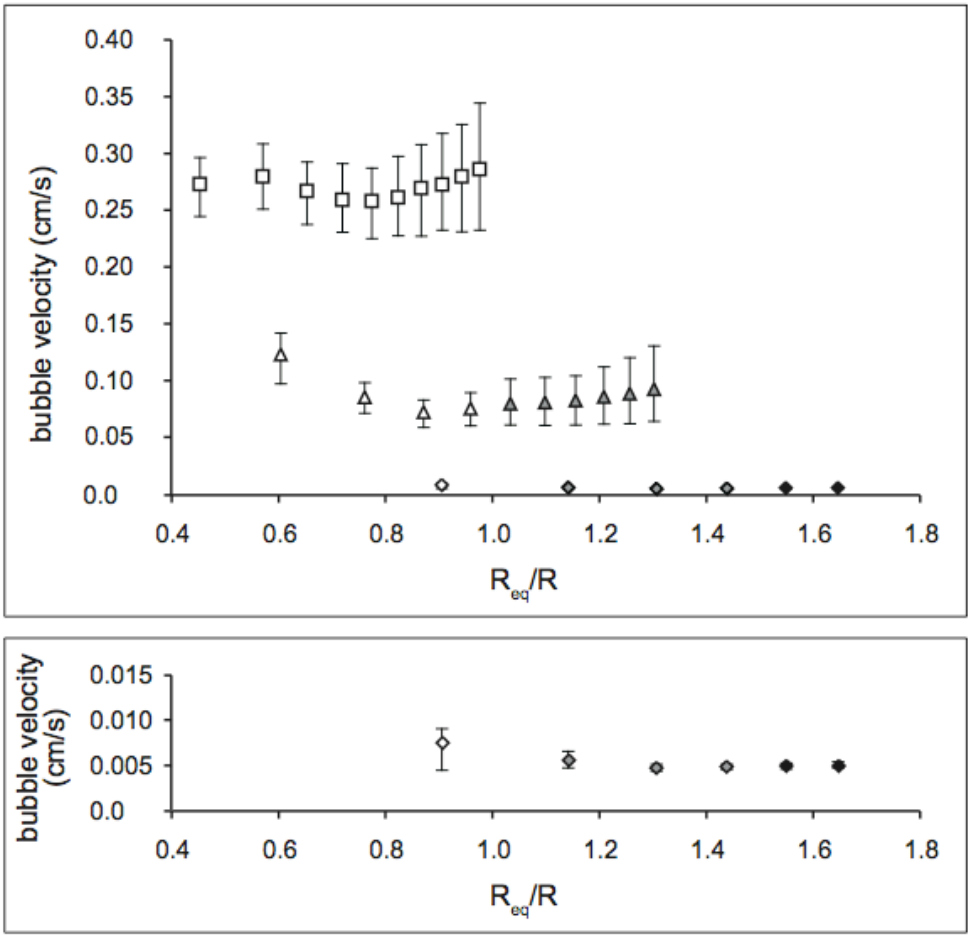

Figure 4.4. Top: experimental bubble velocities in partially submerged tubes in light Karo corn syrup as a function of bubble equivalent radius / tube radius. Diamonds: 2/8 inch tube; triangles: 3/8 inch tube; squares: 4/8 inch tube. Open symbols: subspherical bubbles ($R_{equiv}/R < 1$); gray symbols: transitionary bubbles: ($1 < R_{equiv}/R < 1.5$); black symbols: Taylor bubbles ($R_{equiv}/R > 1.5$). Symbols show the average of measurements in Table 4.1. for each bubble size-tube size combination. Error bars show the spread of the measured values around the average. Bottom: values for the 2/8 inch tube on a larger scale.

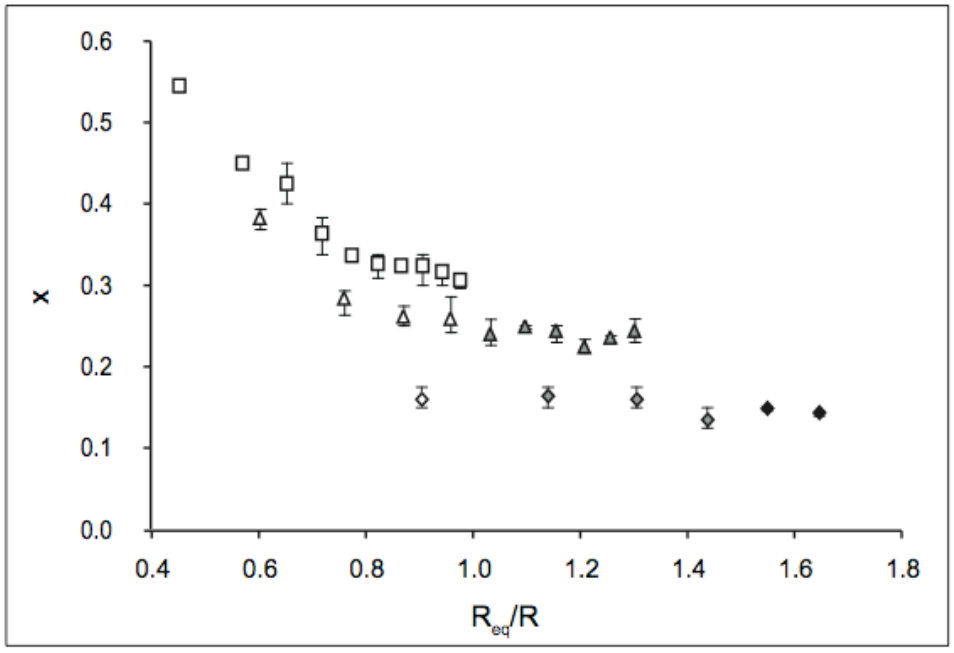

Figure 4.5. Variation of measured dimensionless film thickness x with bubble size relative to tube size in partially submerged tubes of different width in corn syrup. Symbols and shades are the same as on Figure 4.4. Symbols represent the averages of three measurements and error bars show the spread of the data.

Many literature predictions, developed for various ranges of fluid properties and bubble-tube size combinations, exist for the rise velocity of Taylor bubbles in tubes that are sealed on one end. In Figure 4.6. we plot the measured velocities in our experiments normalized to velocities predicted with several of these literature equations versus R_{eq}/R for the three tube sizes in which our experimental measurements were made. All literature predictions are constants that depend on tube radius but not on bubble size. The slope in the predicted lines on Figure 4.6. is due to the variability in our experimental measurements, which do not remain strictly constant with bubble size (Figure 4.4.). Figure 4.6. shows that most literature equations predict velocities that are (sometimes several orders of magnitude) too high ($U_{bubble}/U_{prediction} << 1$). Although these predictions

are for Taylor bubbles ($R_{eq}/R > 1$), the overprediction is worse in the smaller tubes. The predictions of Viana et al. (2003) and of Wallis (1969, in Viana et al., 2003) match the data well in the two largest tubes and reasonably well in the smaller tube. Viana et al. (2003)'s prediction is empirical and based on a large dataset of experiments with viscosities up to 3.9 Pa s, close to the viscosity in our Karo syrup experiments (~4 Pa s). Wallis (1969)'s equation includes an adjustable variable that depends on the liquid viscosity. All other predictions are valid only at viscosities much lower than those used in our experiments, which may account for the dramatic overprediction of the velocities in these cases.

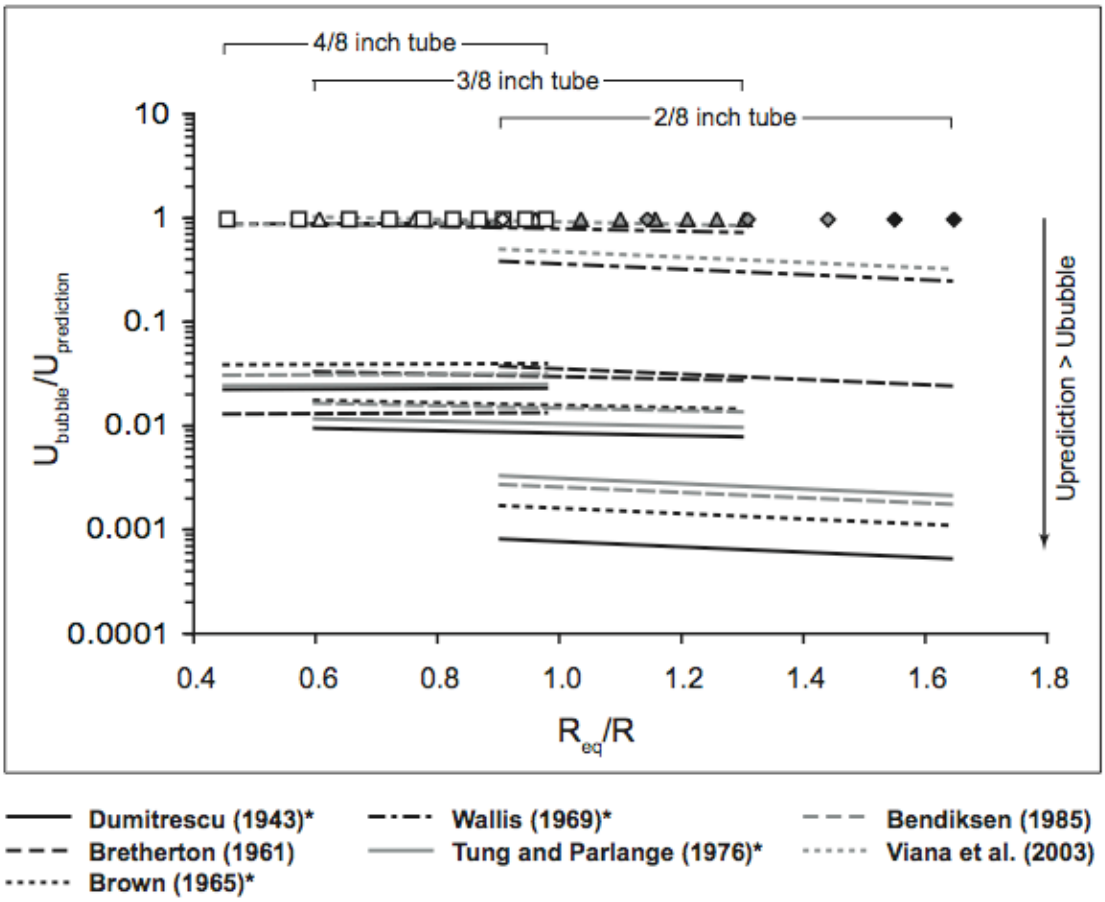

Figure 4.6. Comparison of measured bubble rise velocities in partially submerged tubes in Karo syrup with literature predictions for bubbles in sealed tubes. Measured velocities are shown normalized to the predictions, so that values of $U_{bubble}/U_{prediction} < 1$ indicate the predictions are too high. Measured velocities (symbols) are shown normalized to themselves ($U_{bubble}/U_{bubble} = 1$) for reference. Predictions marked with an asterisk in the legend are from the literature review in Viana et al. (2003). See text for discussion.

4.2. Fully submerged tubes

In tubes that are fully submerged, liquid can flow out the top of the tube as well as through the liquid film between the (nonwetting) bubble and inner tube wall. Table 4.3. summarizes results of experiments in Karo syrup for the different tube sizes. The

relationship between rise velocity and R_{eq}/R is shown in Figure 4.7. The symbols represent the averages of the three runs for each experiment in Table 4.3. Results from partially submerged tube experiments are shown in light gray for comparison. Rise velocities increase with bubble size and with tube diameter for $R_{eq}/R > 0.8$. The increase is faster in the wider tubes. At $R_{eq}/R > 0.8$, velocities in fully submerged tubes are higher that those in partially submerged tubes, although velocities in all cases are lower than the Stokes free rise velocity in absence of a tube ($U_{bubble} = R_{eq}^2 \Delta\rho g/3\mu$; Figure 4.7., bottom). For $R_{eq}/R < 0.8$, U_{bubble}/U_{Stokes} increases rapidly with decreasing bubble size, and should reach $U_{bubble}/U_{Stokes} = 1$ when $R_{eq} << R$ and the wall effects become negligible.

Bubble volume (ml)	Avg. velocity (10^{-3} m/s) in fully submerged tubes in corn syrup											
	Tube diameter 1/8”			Tube diameter 2/8”			Tube diameter 3/8”			Tube diameter 4/8”		
0.1	0.04	0.05	0.04	0.17	0.17	0.17	1.33	1.26	1.27	2.34	2.06	2.08
0.2	0.13	0.13	0.13	0.24	0.25	0.24	1.09	1.05	1.07	2.52	2.27	2.31
0.3	0.24	0.23	0.25	0.37	0.36	0.41	1.13	1.11	1.11	2.51	2.32	2.36
0.4	0.39	0.42	0.43	0.49	0.49	0.56	1.32	1.30	1.31	2.55	2.45	2.46
0.5	0.67	--	--	0.63	0.63	0.74	1.49	1.48	1.48	2.66	2.60	2.62
0.6	--	--	--	0.86	0.81	0.96	1.68	1.70	1.70	2.79	2.79	2.80
0.7	--	--	--	1.07	0.97	1.19	1.87	1.90	1.91	2.97	2.98	2.98
0.8	--	--	--	1.30	1.17	1.45	2.07	2.12	2.14	3.16	3.18	3.22
0.9	--	--	--	1.65	1.24	1.76	2.30	2.34	2.37	3.35	3.40	3.44
1.0	--	--	--	1.93	1.56	2.16	2.53	2.58	2.62	3.56	3.61	3.69

Table 4.3. Bubble rise velocities in fully submerged narrow tubes in light Karo corn syrup. Listed values are averages of measurements between 5 and 10 cm, 10 and 15 cm and 15 and 20 cm (the end of the tube), except for the 3/8 inch diameter tube, where the very top was slightly bent, so that we only use measurements between 5 and 15 cm (justified because bubble rise velocities in our experiments do not change detectably over the length of the tube). Results are shown for 3 repeat experiments for each bubble size in each tube.

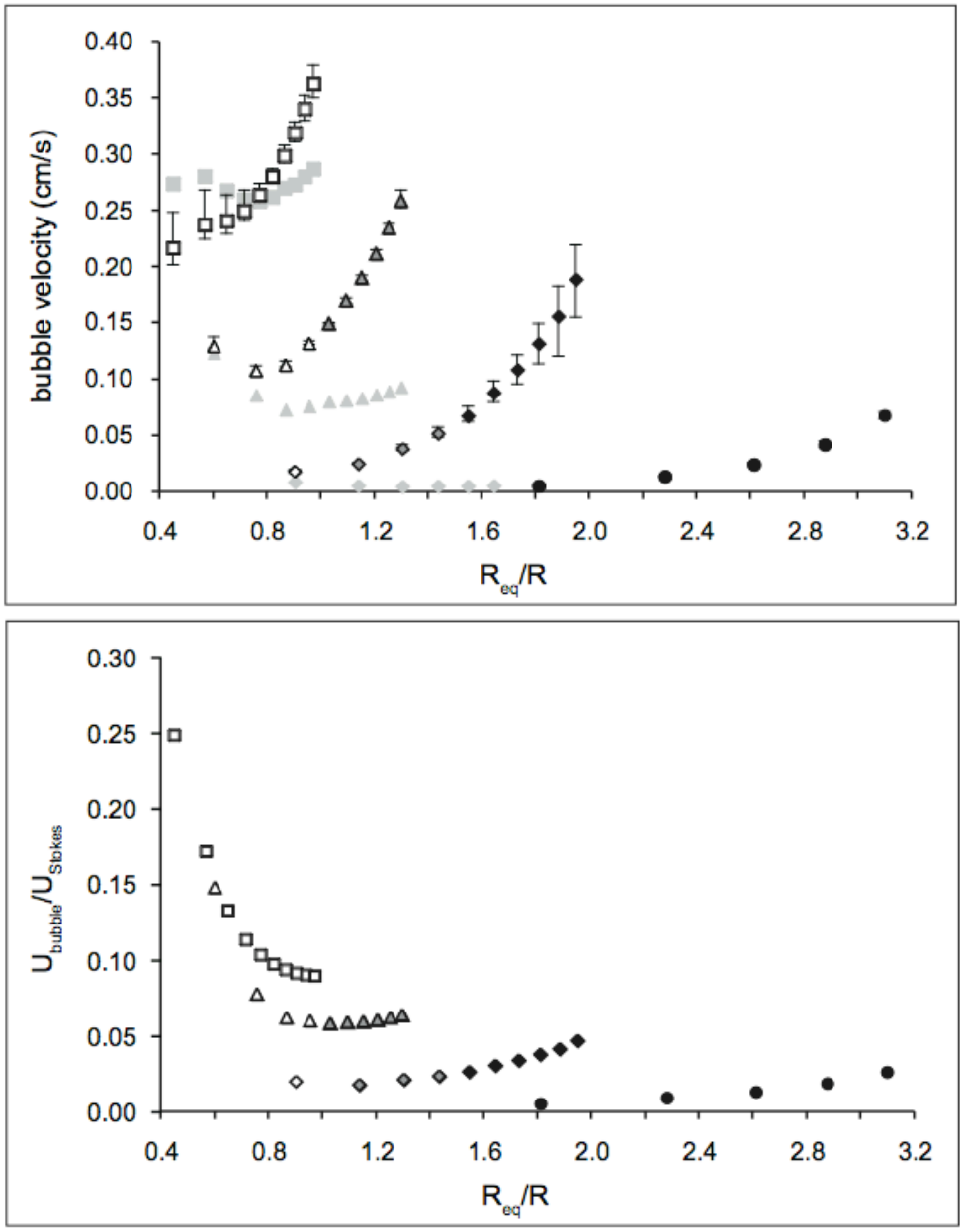

Figure 4.7. Top: experimental bubble velocities in vertical tubes fully submerged in light Karo corn syrup versus R_{eq}/R. Light gray symbols show measurements in 2/8, 3/8 and 4/8 inch partially submerged tubes for comparison. Bottom: bubble velocities normalized to the Stokes free rise velocity for viscous liquids in absence of a tube ($U_{bubble} = R_{eq}^2 \Delta\rho g/3\mu$). Symbols represent averages of three runs for each experiment. Circles: 1/8 inch tube diameter; diamonds: 2/8 inch tube diameter; triangles: 3/8 inch tube diameter; squares: 4/8 inch tube diameter. Open symbols: sub-spherical bubbles; dark gray: transitional bubbles; black: Taylor bubbles.

The variation of dimensionless film thickness x with bubble volume is listed in Table 4.4. and shown in Figure 4.8. Again, values of x in partially submerged tubes are shown in light gray for comparison. At $R_{equiv}/R < 1$, the film thickness is similar in fully and partially submerged tubes. For $R_{equiv}/R > 1$, however, x tends towards a constant value that is slightly larger in fully submerged tubes than in the partially submerged tubes.

Bubble vol. (ml)	x in fully submerged tubes		
	2/8”	3/8”	4/8”
0.1	0.180	0.403	0.564
0.2	0.149	0.281	0.459
0.3	0.173	0.262	0.460
0.4	0.193	0.257	0.370
0.5	0.191	0.264	0.347
0.6	0.207	0.268	0.339
0.7	0.216	0.266	0.334
0.8	0.224	0.275	0.324
0.9	0.226	0.273	0.323
1.0	0.229	0.274	0.329

Table 4.4. Measurements of film thickness expressed as a fraction x of the tube radius in light Karo corn syrup in fully submerged tubes with internal diameter 2/8, 3/8 and 4/8 inch. In the 1/8” tube the film thickness is too small to measure.

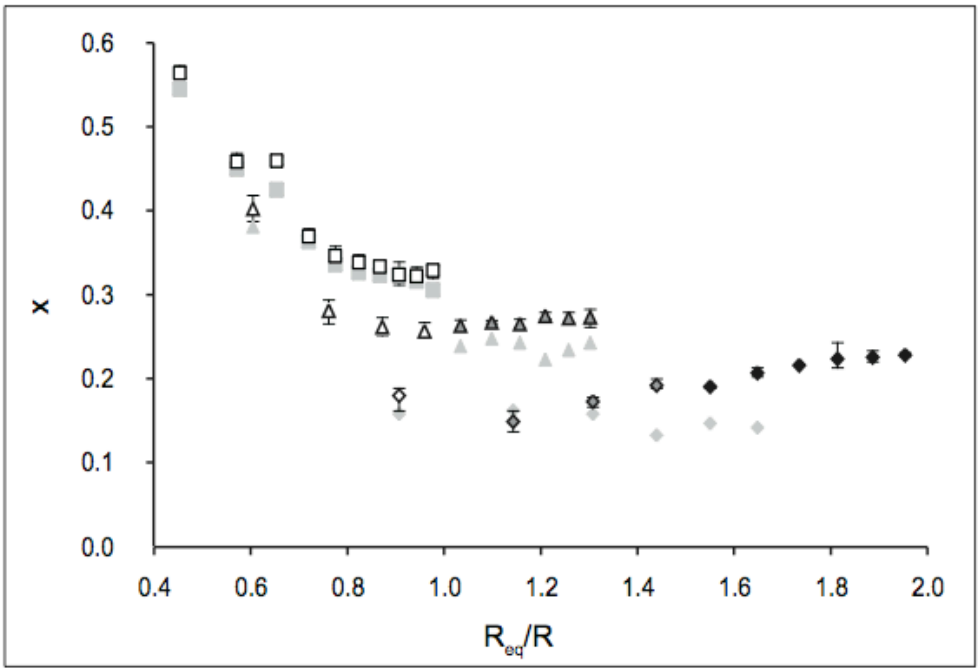

Figure 4.8. Dimensionless film thickness x as a function of normalized bubble size for bubbles rising in fully submerged tubes with different widths in light Karo corn syrup. Symbols are averages of three measurements, with error bars representing the spread in the data. Circles: 1/8 inch tube diameter; diamonds: 2/8 inch tube diameter; triangles: 3/8 inch tube diameter; squares: 4/8 inch tube diameter. Open symbols: sub-spherical bubbles; dark gray: transitional bubbles; black: Taylor bubbles. Measurements in partially submerged tubes are shown in light gray for comparison.

4.3. Comparison with porous media

To investigate the applicability of models for bubble rise in a tubes to porous media, we compare our experiments to experiments performed in a porous medium consisting of corn syrup and square plastic beads (data from Supplementary figure 2 in Belien et al. (2010) (Chapter III of this dissertation, Figure 3.6.)). Particles have widths of ~7mm and are spaced approximately 3-7 mm apart, which corresponds to the inner diameter of our two smallest (1/8 and 2/8 inch) tubes. Figure 4.9. shows a comparison of

the measured velocities in this particle suspension to our measured data in 1/8 and 2/8 inch tubes. Measured velocities in fully submerged tubes (black symbols) are similar to bubble velocities in the suspension (small gray circles), although the increase in velocity with bubble volume is steeper in the tubes. It should be noted, however, that the flattening of the trend for larger bubbles in the suspension is due to splitting of bubbles around the particles, so that many of the velocity values listed for large bubbles are actually those of smaller bubbles derived from these large ones (see Chapter III). The highest velocities shown, for the largest daughter bubbles, correspond well with the velocities measured in the 2/8 inch tube. For small bubble sizes, velocities in tubes are on the low end of those measured in the suspension. This is possibly due to the fact that the particle network in the suspension is not completely rigid and passing bubbles can push the particles aside a bit, thereby essentially widening the pores and allowing faster bubble rise. Overall, bubble velocities in fully submerged tubes correspond well to bubble velocities measured in the suspension, while bubbles in partially submerged tubes (open symbols close to velocity = 0) yield velocities that are too low. This confirms our hypothesis that liquid return flow can occur around the particles and that fully submerged tubes are a better analogue for bubble rise through porous media than rise through tubes in which liquid flow is restricted to the thin film between the bubble and tube wall. We conclude that bubble rise in sealed tubes is not a satisfactory analogue for bubble flow through porous media. In the next section, we use a simple theory to investigate the forces controlling bubble rise in fully submerged tubes. We compare our measurements in fully submerged tubes to rise velocities in partially submerged tubes, using the prediction from Viana et al. (2003) as a proxy for the latter (see section 4.1.), to develop

an equation that we can use in a numerical model to calculate bubble rise velocities in natural porous media.

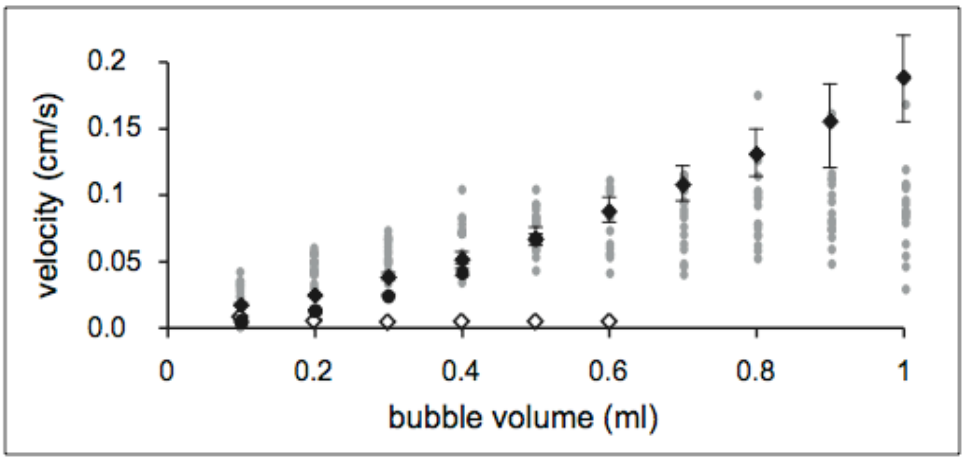

Figure 4.9. Comparison of measured bubble velocities in Karo syrup in fully and partially submerged tubes to velocities measured in a suspension of plastic particles in corn syrup from Belien et al. (2010), Supplementary figure 2. Small gray circles: bubble velocities in the suspension; black circles: experimental velocities in a fully submerged tube with 1/8 inch internal diameter; black diamonds: experimental velocities in a fully submerged tube with internal diameter 2/8 inch; open diamonds: experimental velocities in a partially submerged tube with internal diameter 2/8 inch. Diameters of these tubes correspond approximately to the particle spacing in the suspension. Error bars show the spread of measured values around the mean of the velocities measured in the tubes.

5. Predicting bubble velocities in fully submerged tubes

Our experimental results show that bubble rise velocities in fully submerged tubes are better suited to modeling bubble rise through porous media than those in partially submerged or sealed tubes in which rise is restricted by the rate of liquid return flow through the thin film between the bubble and tube walls. Although many predictions exist

in the literature describing the latter case, we have been unable to find predictions for buoyant bubble rise in tubes fully submerged in an otherwise stagnant liquid, as in our experiments. In this section, we first investigate the factors controlling bubble velocity in fully submerged tubes by developing a simple theoretical description of this situation. Because our simple model does not fully explain the observed bubble rise behavior, we then compare our experimental results to a literature prediction for sealed tubes to find a relationship that we can use in a numerical model.

5.1. Theory

To describe bubble velocities in fully submerged tubes, we derive a simplified equation based on buoyancy and viscous forces. Since the liquid is viscous, we assume as a first order approximation that these two effects dominate and that surface tension is negligible. The bubbles in our experiments are non-wetting, so we ignore wetting effects as well. We approximate the bubble shape by a cylinder with length l_{bubble} and radius R-h, where h is the thickness of the liquid film separating the bubble and tube wall and R is the tube radius (Figure 4.10.). P_{above} is the pressure directly above the bubble, at distance l_{above} below the top of the tube, which is a distance l_{free} below the liquid level. The pressure at the base of the bubble is P_{below}. The pressures at the top and base of the tube are P_L and P_0 respectively. The bubble rises due to buoyancy at velocity U_{bubble}, causing flow in an otherwise stagnant liquid with density ρ and viscosity μ. The liquid is incompressible and flows by Poiseuille flow out the top of the tube at average velocity U_{out}. Some liquid moves downward in the fluid film between the bubble and tube walls at

velocity U_{film}. As the bubble rises, a return Poiseuille flow brings liquid back into the base of the tube at velocity U_{in}.

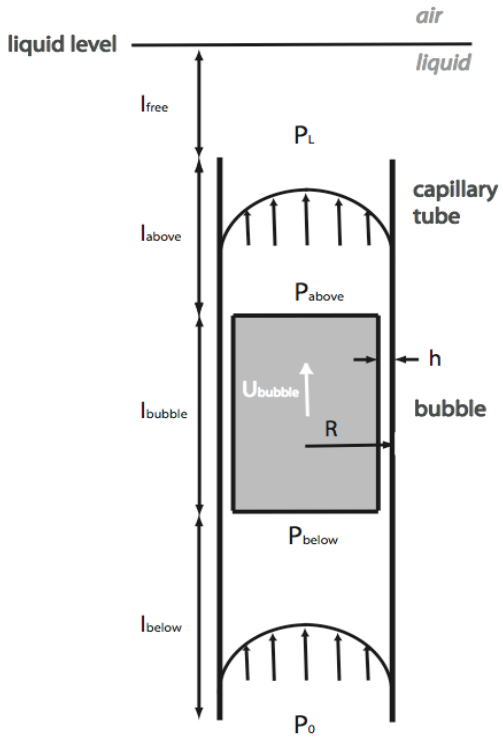

Figure 4.10. Simplified schematic of a bubble rising in a fully submerged tube showing parameters and notation used in the derivation of the equation for bubble rise velocity.

To conserve mass in the tube, the volume flux Q_{out} out must balance Q_{in}, and both must equal the combined flux in the bubble and in the liquid film between the bubble and tube wall (which is negative as flow in the film is downwards):

$$Q_{out} = Q_{in} = Q_{bubble} + Q_{film} \qquad \text{or} \qquad Q_{bubble} = Q_{out} - Q_{film}\,. \tag{4.1}$$

Since $Q = AU_{average}$, with A the cross-sectional area of fluid flow,

$$\pi(R-h)^2 U_{bubble} = \pi R^2 U_{out} - \left[\pi R^2 - \pi(R-h)^2\right] U_{film}\,. \tag{4.2}$$

The average Poiseuille velocity U_{out} is

$$U_{out} = \frac{R^2}{8\mu}\left(\frac{P_{above} - P_L}{l_{above}} - \rho g\right), \tag{4.3}$$

and the average film flow U_{film} in the liquid film between the bubble and tube wall is

$$U_{film} = -\frac{h^2}{3\mu}\left(\frac{P_{above} - P_{below}}{l_{bubble}} + \rho g\right). \tag{4.4}$$

Since the liquid in the tube is connected to the liquid reservoir outside the tube and the liquid is stagnant apart from flow induced by bubble rise, the pressure at the top of the tube is approximately hydrostatic

$$P_L \approx \rho g l_{free}. \tag{4.5}$$

We approximate the pressure above the bubble by the hydrostatic pressure plus the buoyancy pressure of the rising bubble

$$P_{above} \approx \rho g\left(l_{free} + l_{above}\right) + \Delta\rho g l_{bubble}. \tag{4.6}$$

Similarly, the pressure below the rising bubble is approximately

$$P_{below} \approx \rho g\left(l_{free} + l_{above} + l_{bubble}\right) - \Delta\rho g l_{bubble}. \tag{4.7}$$

In our case, the bubble (air) density is much smaller than the density of the surrounding liquid and $\Delta\rho \approx \rho$, so that

$$P_{above} \approx \rho g\left(l_{free} + l_{above} + l_{bubble}\right), \qquad \text{and} \tag{4.8}$$

$$P_{below} \approx \rho g\left(l_{free} + l_{above}\right). \tag{4.9}$$

Inserting Equations 4.3-4.9 into Equation 4.2 gives

$$U_{bubble} \approx \frac{\rho g}{8\mu}\frac{R^4}{\left(R-h\right)^2}\left(\frac{l_{bubble}}{l_{above}}\right) + \frac{2\rho g}{3\mu}\frac{h^3\left(2R-h\right)}{\left(R-h\right)^2}. \tag{4.10}$$

This equation can be simplified if we express the film thickness as a fraction $\bar{x}$ of the tube radius ($\bar{x} = h/R$)

$$U_{bubble} \approx \frac{\rho g R^2}{\mu(1-\bar{x})^2}\left[\left(\frac{l_{bubble}}{8l_{above}}\right)+\frac{4}{3}\bar{x}^3\left(1-\frac{\bar{x}}{2}\right)\right] \quad \text{for } 0 < \bar{x} < 1. \qquad (4.11)$$

The bubble velocity in Equation 4.11 varies as a function of the position l_{above} of the bubble in the tube. In our experiments, we do not detect a measurable variation with l_{above}, probably because the variation is negligible until the bubble reaches the very top of the tube (Figure 4.11.), where the assumption of Poiseuille flow breaks down. Figure 4.11. also shows that it does not matter what value we choose for l_{above} in the equation, as long as we stay away from the sharply increasing part of the curve. The point at which the curve starts to increase is not dependent on the total tube length, but varies with fluid density and viscosity.

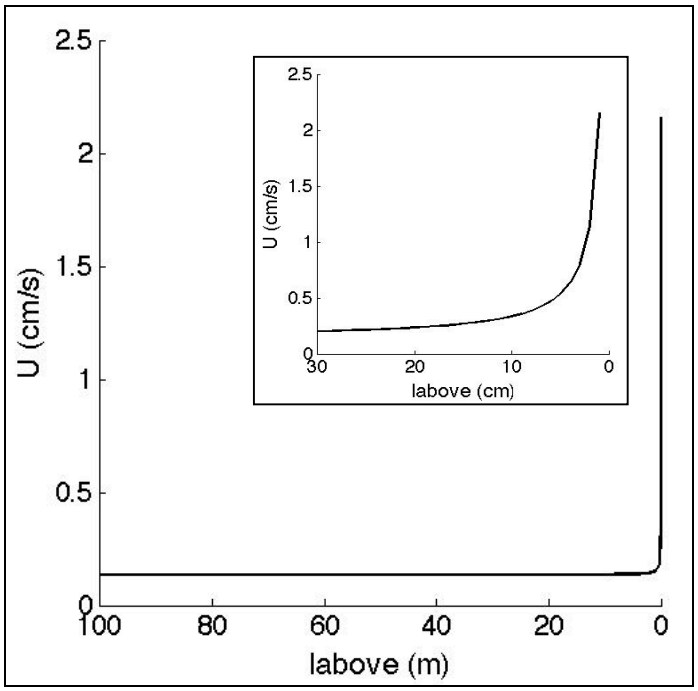

Figure 4.11. Variation in bubble rise velocity in a fully submerged tube with position of the bubble in the tube, calculated with Equation 4.11. All parameters except l_{above} are kept constant at the experimental values for Karo syrup. Tube length L = 20 cm; ρ = 1320 kg/m^3, μ = 4.12 Pa s; R = 4 mm (experimental average); bubble volume V = 0.55 ml (experimental average); l_{bubble} = 1.66 cm (calculated from V and R), x = 0.24 (calculated from experimental variation of x with bubble and tube radius in Karo syrup). Note that the x-axis scale on the inset is in cm while the full image is in m.

A comparison of our experimental data with the prediction from Equation 4.11, using measured values of x for $\bar{x}$, is shown in Figure 4.12. for $R_{eq}/R > 1$. The equation gives the right trend but consistently overpredicts the velocities, indicating that our assumptions are not completely justified. A more rigorous theoretical model, which should also take the effects of surface tension into account, is needed to directly predict bubble rise velocities in open tubes.

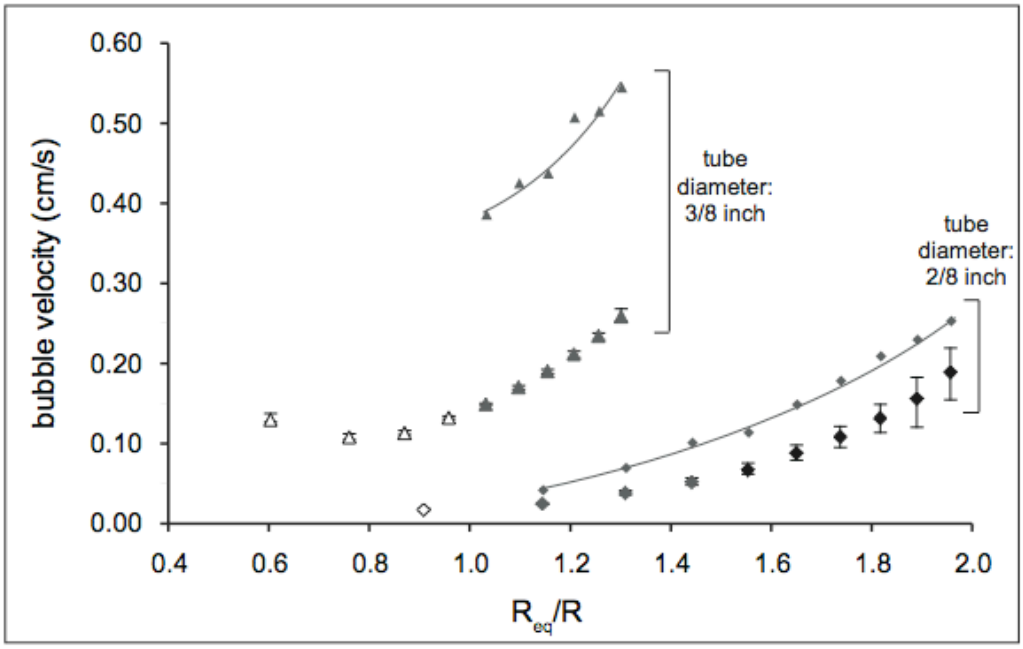

Figure 4.12. Comparison of experimental bubble velocities in light Karo syrup in fully submerged tubes (isolated symbols with error bars) with predictions from Equation 4.11 (small symbols and line) for $R_{eq}/R > 1$. Measured values of x are used for $\bar{x}$ in the equation; l_{above} is set at 20 cm (the length of the experimental tubes). Results shown for tubes with internal diameter 2/8 and 3/8 inch ($R_{eq}/R < 1$ and Equation 4.11 is not valid in the 4/8 inch tube; x was not measured in the 1/8 inch tube). Averages of three experimental measurements are shown, with error bars representing the spread in the data. Diamonds: 2/8 inch tube diameter; triangles: 3/8 inch tube diameter. Open symbols: sub-spherical bubbles; dark gray: transitional bubbles; black: Taylor bubbles.

5.2. An empirical prediction

The theory derived in the previous section can reproduce the observed increase of bubble rise velocity with R_{eq}/R in fully submerged tubes, but overpredicts the velocities themselves. To predict bubble rise velocities though porous media where we do not have measurements, we need another way of calculating velocities that is not dependent on the simplifications of our theory. In addition, our theory requires known film thicknesses, which vary with bubble and tube size (see section 4.2.) in a way that is generally unknown in the system of interest. We are unaware, however, of any alternative predictions for buoyancy-driven flow in open tubes in the literature.

Literature predictions do exist, however, for the velocity of bubbles in narrow tubes sealed on one end (our partially submerged tube case, see section 4.1.). We can use these predictions to calculate the bubble velocity in our system if the tubes (representing the pore space) were sealed, and then derive the velocity in the case where the tubes are open on both ends (fully submerged tubes; more analogous to porous media) from the calculated sealed tube velocity if we know the relationship between them. We assume as a first order approximation that the closed and open tube cases have similar dependences on liquid density, viscosity and surface tension, so that all these effects will be accounted for as long as they are present in the equation we use to calculate the sealed tube velocities. If this is the case, the method described below should yield the same equation (within error) for different fluids.

To determine the relationship between the closed and open tube velocities, we compare our measured velocities in open (fully submerged) tubes to the velocities in

closed tubes predicted according to Viana et al. (2003). Out of all the literature predictions in Figure 4.6. (section 4.1.), this prediction best describes the velocities in partially submerged tubes in our experimental system, with experimental $U_{bubble,\ partially\ submerged}$ / predicted $U_{Viana\ et\ al.\ (2003)}$ ~1. Viana et al. (2003)'s equation is an empirical relationship, based on a large compilation of experimental data, that does not depend on a specific theoretical model with its associated assumptions. The resulting equations include gravitational, viscous and surface tension forces in the form of the dimensionless buoyancy Reynolds number $Re_b = \frac{\left[(2R)^3 g(\Delta\rho)\rho\right]^{1/2}}{\mu}$ and Eötvös number $Eo = \frac{g\rho(2R)^2}{\sigma}$. The velocity is expressed as the Froude number $Fr = \frac{U_{bubble}}{(2gR)^{1/2}}$. For $Re_b < 10$ (viscous liquids), which is the case in all our experiments and at Stromboli,

$$Fr = \frac{9.494 \times 10^{-3}}{\left(1 + 6197/Eo^{2.561}\right)^{0.5793}} Re_b^{1.026}.$$

When we normalize our experimental velocities in fully submerged tubes in Karo syrup to this prediction, the normalized values follow an exponentially increasing trend with R_{eq}/R (Figure 4.13., black symbols). Viana et al. (2003)'s prediction is a constant that depends on tube radius but is independent of bubble size, so that the normalized velocity trend represents the deviation of the velocities in fully submerged tubes away from this constant. The prediction for bubble rise velocities in fully submerged tubes obtained in this way is $U_{bubble,\ fully\ submerged} = U_{Viana\ et\ al.\ (2003)}\left(0.22e^{2.12\frac{Req}{R}}\right)$. Inserting Viana et al. (2003)'s equation gives

$$U_{bubble} = 0.22e^{2.12\frac{Req}{R}}(2gR)^{1/2}\frac{9.494\times10^{-3}}{\left(1+6197/Eo^{2.561}\right)^{0.5793}}Re_b^{1.026} \qquad \text{for } Re_b < 10,$$

which allows us to calculate bubble velocities in open (fully submerged) tubes from the tube and bubble sizes and the fluid properties.

If our assumption that liquid properties are eliminated by the normalization is true, this relationship should also hold for different fluid types, as long as the bubble density and viscosity remain negligible compared to those of the surrounding liquid. We test this with the results from our experiments in fully submerged tubes in glycerin (gray symbols on Figure 4.13.). The trends are similar within the error introduced by the temperature-dependent viscosity variation of the liquids (see section 3.1.). Experiments with a larger number of fluids should be done in the future to ascertain whether this assumption holds over a wider range of fluid properties.

Surface tension effects are included in this analysis via the normalization equation. In addition, this method does not depend on our theoretical model assumptions. We therefore consider this method to be more accurate than Equation 4.11, and use it in the next section to develop a predictive numerical model for bubble rise through crystal-rich magma at Stromboli, keeping in mind that our assumption that fluid properties cancel out in the normalization has not been tested at properties relevant for Stromboli. It should also be noted that, although applicable to fluids more viscous than most other predictions, Viana et al. (2003)'s equation is calibrated only for liquid viscosities up to 3.9 Pa s (~μ of Karo syrup). At Stromboli, liquid viscosities are two orders of magnitude higher and thus outside the tested range, which should also be kept in mind when evaluating the results from our numerical model.

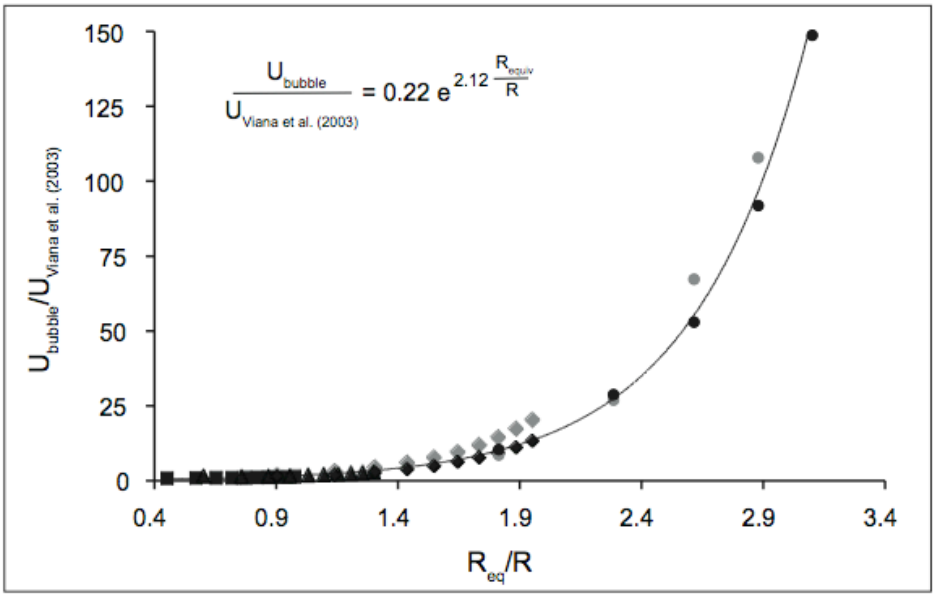

Figure 4.13. Measured velocities in fully submerged tubes in Karo syrup (black) and glycerin (gray) normalized to the corresponding velocity in a sealed tube calculated according to Viana et al. (2003). Circles: 1/8 inch tube; diamonds: 2/8 inch tube; triangles: 3/8 inch tube; squares: 4/8 inch tube. The equation for the best-fit exponential is given ($r^2 = 0.965$).

6. A numerical model for bubble percolation through porous media

We create a MATLAB® model to predict the rise velocity of a bubble through a porous medium based on the rise of bubbles in narrow tubes that are open on both ends. Tubes correspond to the pore space between particles, and begin and end at the bottom and top of a particle, where the liquid can move sideways either away from or into the pore. The tube length thus corresponds to the particle length, and the tube width to the particle spacing.

6.1. Model geometry

In our model, the code for which is given in Appendix C, the pore space is a series of vertical tubes with widths and lengths randomly chosen from a pre-defined distribution. Fluid density, viscosity and surface tension, and total thickness of the porous medium are pre-defined input variables. The bubble size is chosen from a pre-defined distribution as well and remains constant throughout the entire traverse of the porous medium. As the bubble rises, we grow the network of tubes ahead of it. The bubble starts at the base of the model porous medium in a tube with length L and radius R. If bubble equivalent radius / tube radius $\geq$ 0.45, the velocity is calculated with the normalization method described above. The cutoff is chosen at 0.45 since we know from our experiments that the exponential relationship holds at least to that value. For smaller bubbles the velocity is calculated according to the Stokes equation for free bubble rise, using the Hadamard-Rybczynski modification for viscous liquids ($U_{bubble} = R_{equiv}^2 \rho g / 3\mu$). Note that in reality bubbles of this size might still be influenced in their rise by the proximity of the tube walls, so that the velocity calculated by the Stokes equation is a maximum value. In addition, our model addresses the rise of individual bubbles through the porous medium, although multiple bubbles are typically present in the system. It has been shown that multiple bubbles in a porous medium influence each other's rise and decrease the rise velocities (Roosevelt and Corapcioglu, 1998).

When the bubble reaches the top of each tube, we generate a new tube with new random L and R pulled from the distribution. We keep track of bubble rise times ($t = L/U_{bubble}$) and vertical distances and calculate the average bubble rise velocity at the

end of the model run. The model run is complete when the total distance traversed by the bubble (the sum of all tube lengths L) reaches the thickness of the porous medium. Note that we model only the part of the porous medium that the bubble is rising through. What the rest of the porous medium looks like is irrelevant as long as tubes are somehow connected so fluid can flow from the top of a tube back in to the bottom without being forced through the liquid film. The random selection of tube properties ensures that the pathway geometry is different in each model run and introduces a degree of randomness representing the multitude of possible pathways a bubble could take through a natural system. The tube properties can be pulled from real distributions of particle length (L) and spacing (R) in the porous medium of interest.

The model is run 100 times for each bubble size in a Monte Carlo-type simulation to determine the bubble's mean travel time through the model space. The total gas velocity through the medium is then the weighted average of all mean velocities for all bubble sizes in the distribution. Because it is computationally slow to run 100 simulations for every bubble size in the distribution and then weight them, we instead estimate the total gas velocity by running 100 simulations in which we vary both tube size (length and radius) and bubble size whenever a new tube gets created.

In the next section, we apply this model to calculate gas velocities through the crystal-rich magma at Stromboli volcano.

7. Application to bubble percolation at Stromboli volcano

7.1. Modeling parameters

The fluid properties for Stromboli's magma used in our model are the same as those used in Chapter III (Belien et al., 2010) and are listed for reference in Table 4.5. These properties are for the liquid phase in the pore space between the crystals.

Fluid properties for Stromboli melt		Reference
Density	2690 kg/m^3	Métrich et al. (2001), Bertagnini et al. (2003) Glass in melt inclusions in pumice
Viscosity	330 Pa s	Calculated from compositional data for glassy matrices in crystal-rich scoria in Landi et al. (2004) using the method of Shaw (1972) with 0.1 weight% H_2O and T=1115 ^oC (Landi et al., 2008). Not corrected for crystal content.
Surface tension	0.1-0.4 N/m	Khitarov et al. (1979)

Table 4.5. Fluid properties for Stromboli magma used in our numerical model, cf. Belien et al. (2010) (Chapter III).

Bubble and crystal sizes as well as crystal spacing are measured on thin section scans from crystal-rich tephra collected during different periods of normal Strombolian activity in 2007, 2008 and 2009. Twenty-one representative sections of the scans were analyzed to obtain distributions of these parameters (Figure 4.14.). Our image analysis methods are discussed in Appendix B. The measured distribution of crystal long axis lengths is used as model input for the tube lengths. The distribution of crystal spacings is

used as input for tube width, and the distribution of equivalent radii, calculated from the area of bubbles in the images, is the input for bubble radii. It should be noted that these measurements were made on two-dimensional sections of a three-dimensional rock, and are biased relative to the real population (e.g. Mangan et al., 1993). In particular, small bubbles and crystals might be underrepresented because the probability of being cut by a two-dimensional plane in a random orientation increases with object size. Conversely, objects could seem smaller in 2D than they really are because of the cut effect (random slices through a sphere yield apparent radii smaller than the actual radius of the sphere). Following Mangan et al. (1993), we correct for this latter effect for individual spherical objects (~bubbles) by dividing all bubble sizes by 0.85 (this corrected, 3D distribution is the one we use in our model). Measured bubble sizes may be larger than those present in the magma, because syn-eruptive gas expansion causes bubbles to expand on eruption before being trapped in the cooling rock. This effect was minimized by avoiding the interiors of the tephra clasts, where cooling is slowest and expansion largest, in the analysis. In addition, very large bubbles will not be preserved in the volcanic rocks and therefore not measured at all. Crystal spacings are likewise approximate, both due to the cut effect and due to the way in which they are measured (see Appendix B).

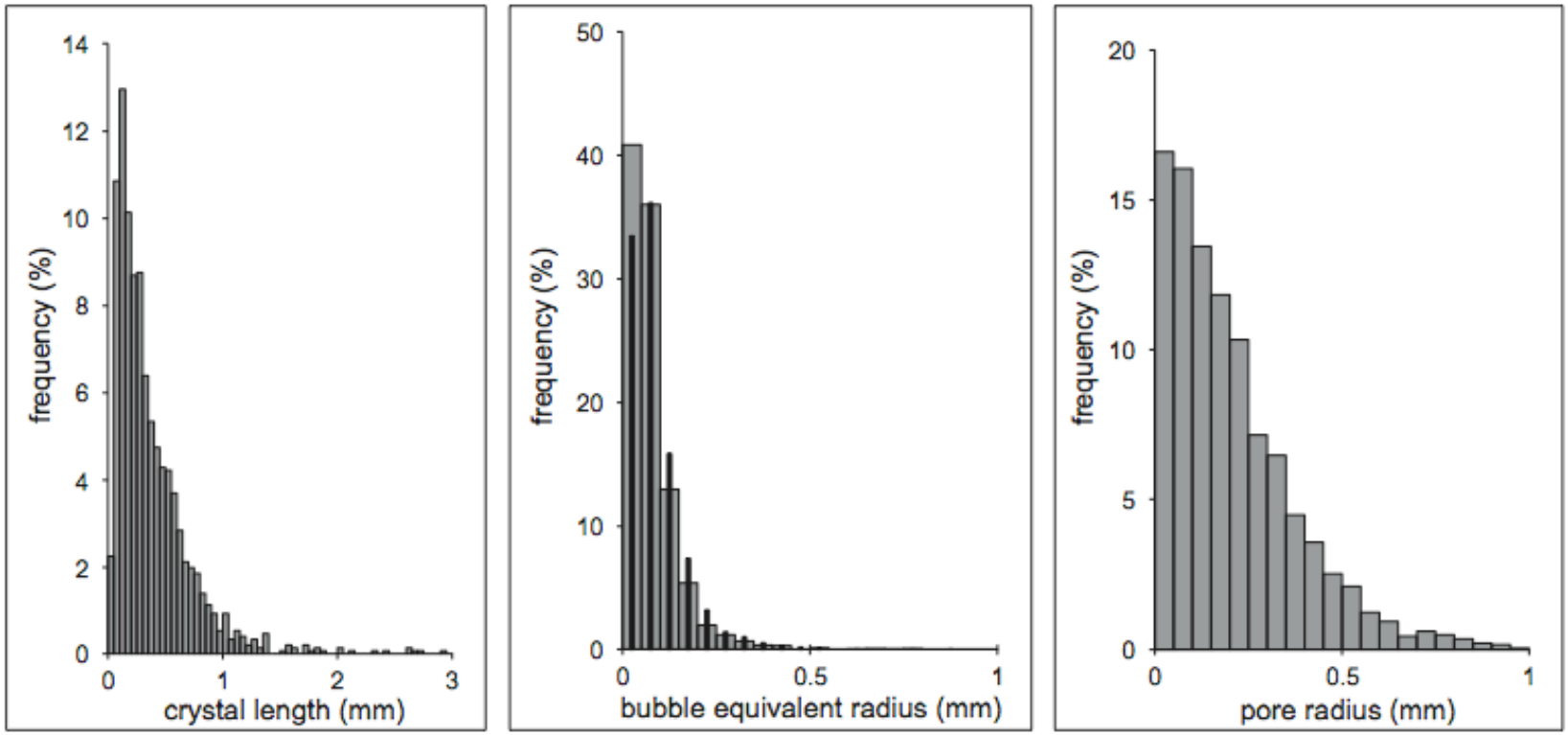

Figure 4.14. Distributions of (left to right) crystal long axis lengths (tube lengths), bubble area equivalent radii (bubble radii), and half of the intercrystal distances (pore radii) at Stromboli volcano, measured on thin section scans of tephra collected during periods of normal activity. See Appendix B for methodology. Gray bins are two-dimensional distributions; narrow black bins show the bubble size distribution corrected for the cut effect (3D). Bins are equally spaced on all plots (0.05 mm width). Few bubbles are larger than the range of sizes shown.

Keeping this in mind, we see on Figure 4.14. that all three distributions are skewed towards the smallest sizes. The bubble radii show the narrowest distribution, with all bubble sizes on the small end of the distribution of pore radii, but small bubbles relatively more abundant than small pores. This means that most bubbles are small relative to the pore size they are in, and that the velocities in our model are likely dominated by the Stokes free rise velocity of these small bubbles rather than the (relatively slower) velocities of the larger bubbles in tubes. Figure 4.15. shows the bubbles and crystals in some of our thin section images, highlighting the abundance of bubbles that are small relative to the crystal spacing. Bubbles in general are abundant, taking up on average 53% of the pore space in our images. The average area taken up by the pore space (melt + bubbles) is 78%, making the overall gas content 41% of the total area (including crystals).

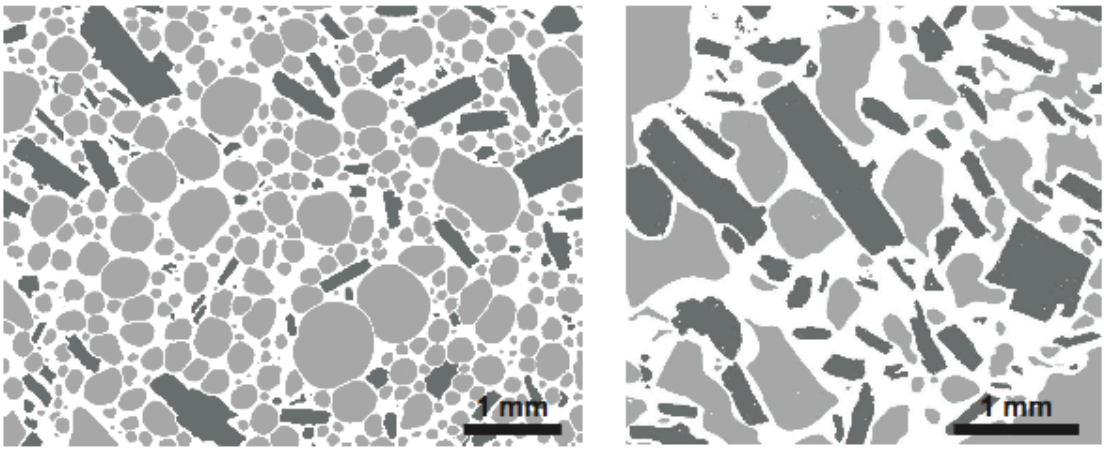

Figure 4.15. Bubbles (light gray) and crystals (dark gray) in two of the thin section images from crystal-rich tephra from Stromboli volcano, used to obtain the distributions in Figure 4.14.

7.2. Model results

We use our model to calculate velocities of bubbles of different sizes, spanning the size distribution observed at Stromboli. We use the fluid properties from Table 4.5. with the minimum, maximum and average surface tension value (0.1, 0.4 and 0.25 N/m). A porous medium thickness of 10 m, which is more than 2000 times the largest crystal length in the distribution, was used to ensure that enough tubes were included in each model run to obtain a representative average velocity through the medium. Average modeled bubble velocities are several orders of magnitude lower in all cases than the Stokes free rise velocities (Figure 4.16.), the difference being largest for the smallest bubbles. This may indicate that, although the smallest bubbles should rise via Stokes flow in our model in most tubes in the distribution, they encounter enough of the very smallest tubes that their average velocity in the porous medium as a whole is significantly delayed. (Note again that this average velocity in the porous medium is a maximum estimate since even the smallest bubbles are likely slowed by wall effects relative to their Stokes velocity). The velocities increase steeply with bubble size below $R_{equiv} \approx 0.1$, after which the increase flattens. In all cases though, the increase of modeled velocity with bubble size is faster than the increase of Stokes free rise velocity with bubble size. This is due to the exponential increase with bubble size of the bubble rise velocity in the tubes, which, for very long bubbles, overtakes the corresponding Stokes free rise velocity, and indicates that the contribution of rise in tubes ($R_{equiv}/R > 0.45$) to the overall velocity becomes increasingly important with bubble size.

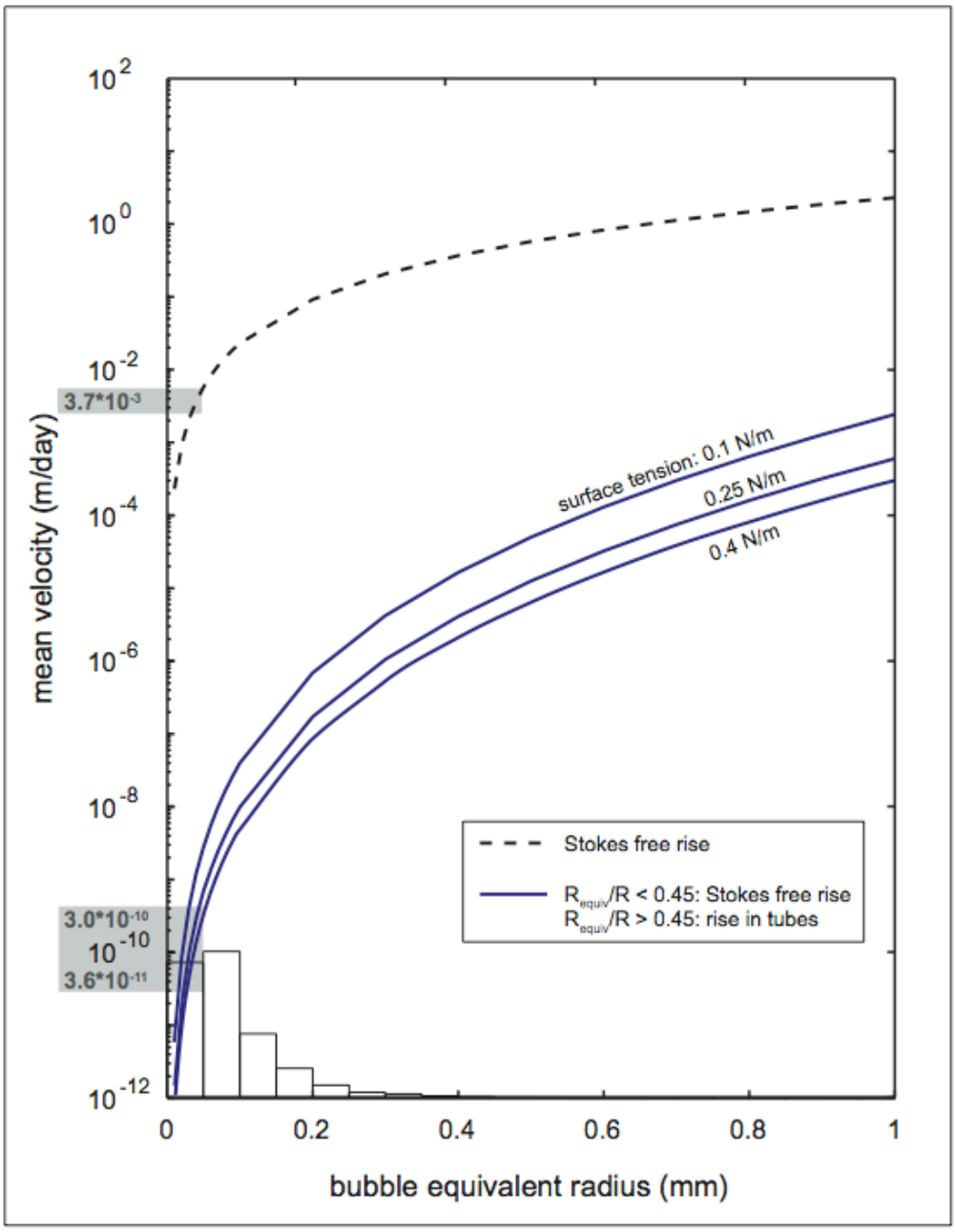

Figure 4.16. Comparison of Stokes free rise velocities and modeled velocities through Stromboli's crystal-rich magma obtained from our model for the range of bubble sizes observed in thin sections. For each bubble size, tube lengths and widths are randomly selected from the distribution of crystal lengths and spacings observed in thin sections from Stromboli (Figure 4.14.). The relative abundance of the different bubble sizes is shown by the histogram at the bottom of the image (3D bubble distribution). Dashed line: Stokes velocity; solid lines: modeled velocity through the porous medium for the range of interfacial tensions in Table 4.5. The gray shaded area shows the modeled average velocity of the whole bubble population at Stromboli, corresponding to the average Stokes and porous media velocities in Figure 4.17.

We obtain an estimate of the overall gas velocity through Stromboli's crystal-rich magma by pulling a new bubble size as well as tube length and width from the distributions every time a new tube is created. The cumulative distribution of average bubble rise velocities in all model runs is shown in Figure 4.17. We use the average surface tension (0.25 N/m) and again model a porous medium thickness of 10 m. The spread of the values in all runs is narrow, confirming that the porous medium thickness used is sufficient to obtain representative velocities. The average velocity of each model run varies between approximately $5*10^{-11}$ and $1.5*10^{-10}$ m/day with a mean of $8.2*10^{-11}$, eight orders of magnitude lower than the velocity calculated for the same system bubble size distribution in absence of crystals (only Stokes rise) (Figure 4.17.). Using surface tension values of 0.1 and 0.4 N/m, the average gas velocity becomes $3.0*10^{-10}$ and $3.6*10^{-11}$ m/day respectively. Figure 4.16. shows that these velocities (gray shaded areas) are associated with bubbles with $R_{equiv} < 0.05$ mm, indicating that the smallest bubble sizes dominate the average bubble rise velocity of this population. The very low modeled gas velocity through Stromboli's crystal-rich magma indicates that bubbles of the sizes observed in tephra are almost stationary.

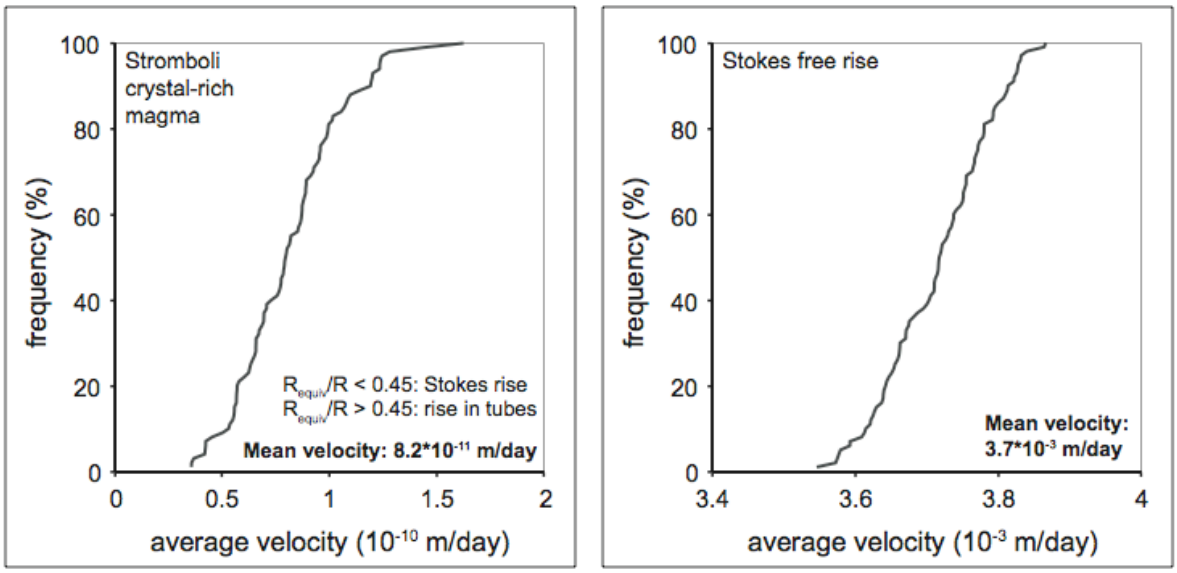

Figure 4.17. Distribution of modeled average gas velocities (of the bubble population as a whole) through Stromboli's upper magma in 100 model runs, in the presence of crystals (left) and assuming no crystals are present (right, only Stokes rise). The modeled bubble population is the 3D corrected bubble size distribution observed in Stromboli tephra (Figure 4.14.). The means of these distributions are highlighted by the gray shaded area on Figure 4.16. (on the middle solid line and the dashed line respectively), showing that the rise velocities of bubbles in the smallest bin size dominate the average velocity of the whole population (shown here).

7.3. Implications for Stromboli's shallow plumbing system

We can compare our estimate of the gas velocity through the crystal-rich magma at Stromboli volcano to gas fluxes measured at this volcano. Degassing is abundant at Stromboli, and occurs throughout the crater terrace, but mostly from the three main vent areas located within this terrace. Three types of degassing can be distinguished: passive degassing, occurring continuously between eruptions, active degassing, occurring as discrete gas bursts, approximately 1-2 seconds apart, mostly from the central vent (McGreger and Lees, 2004; Johnson, 2005, Landi et al., 2011), and gas release during

Strombolian explosions. The total degassing flux measured at Stromboli is ~6600 tons/day (calculated from the 200 tons/day average SO_2 flux from Burton et al. (2007) using the average composition of the degassing plume from Aiuppa et al. (2010)). Non-eruptive degassing accounts for most of the gas output and has been measured at 6.1-12.3*10^3 tons/day (Allard et al., 1994). Of this non-eruptive degassing, about half is attributed to active degassing (puffing) and half is completely passive (Harris and Ripepe, 2007). Gas fluxes measured during Strombolian eruptions are higher, measured at 24-30 kg/s (Chouet et al., 1974; Allard et al., 1994) and 360-960 kg/explosion (Mori and Burton, 2009), which corresponds to 45-192 kg/s using the 5-8 s duration of the explosions observed by Chouet et al. (1974). However, these high fluxes only occur during the short time intervals of the explosions. Since the majority of the degassing is not accompanied by eruption of volcanic rock, but does occur from the open vents, the gas must be rising passively through the crystal-rich magma. It is the migration of this non-eruptive gas that our model addresses.

The non-eruptive gas flux measured by Allard et al. (1994) corresponds to approximately 5*10^6-3*10^8 m^3/day at atmospheric pressure, when a gas density of 0.05-0.3 kg/m^3 is assumed (measured for the eruptive gas plume at Stromboli by Chouet et al., 1974). At a pressure of 5 MPa, corresponding to the lower part of the crystal-rich magma body (cf. Suckale et al., in preparation, Chaper V) the ideal gas law predicts an (isothermal) volume flux of 1*10^5-6*10^6 m^3/day. Taking a cross-sectional area of 33000 m^2 for the magma body (corresponding to the area of the crater terrace, cf. ibid.), and a gas fraction of 0.41 (see section 5.1.; taking observations from tephra as a proxy for the gas fraction at depth), this corresponds to an average gas velocity of 7.5-450 m/day,

orders of magnitude higher than predicted by our model, and much higher even than the average Stokes free rise velocity of the observed bubble population in Stromboli melt (Figure 4.17.). The required gas velocities correspond, however, to the rise of bubbles with radius 3.6-6.1 mm through the crystal-rich magma at Stromboli. The measured flux values can thus be reconciled with a bubble population dominated by mm to cm-sized bubbles instead of the sub-mm bubbles predominant in the tephra. Bubbles of this size are present in the magma (scarce cm-sized bubbles are observed in tephra), but their chance of preservation in the tephra clasts is lower than that of the smaller bubble population and many of the large bubbles are probably lost efficiently from the system. In addition, their apparent under-representation in the thin sections may indicate that our applied conversion from a 2D to a 3D bubble size distribution is insufficient, particularly for the large, and often highly deformed, bubbles. We will test this in the near future by using x-ray microtomography to obtain 3D bubble and crystal size distributions in tephra samples from Stromboli (proposal by I. Belien and Maria Davis (University of Minnesota) accepted for the July-December 2011 running cycle at the Lawrence Berkeley National Laboratory Advanced Light Source Facility (http://www-als.lbl.gov)).

8. Conclusions

We have shown in this study that bubbles rising under buoyancy in narrow tubes of which both ends are submerged, allowing liquid return flow around the outside of the tube, differs significantly from traditional Taylor bubble flow in tubes sealed on one end, and that the former case is more applicable to bubble flow through porous media. The

velocity in these fully submerged tubes varies with bubble size and increases exponentially for bubble equivalent radius / tube radius > 0.45. We derive a simple theory based on a balance of buoyancy and viscous forces, that can predict the correct trend of the velocity increase. However, our theory consistently overpredicts the velocities, suggesting that surface tension forces cannot be ignored and should be included in future theoretical models. Based on an empirical relationship between bubble velocities in fully submerged tubes and literature predictions of bubble rise in sealed tubes, we developed a numerical model to calculate the rise velocity of bubbles through crystal-rich magma at Stromboli volcano. Using bubble and pore size distributions from thin sections of crystal-rich tephra, we calculate a mean velocity of 10^{-10}-10^{-11} m/day, indicating that this population of small bubbles in essentially stagnant. Comparing our modeled velocity with measurements of the non-eruptive degassing flux at Stromboli leads us to conclude that the bubble population is dominated by mm-cm sized bubbles, of which only a small subset is preserved in the erupted tephra. These results illustrate the use of our new model in analyzing the migration of gas bubbles through particle-rich systems.

9. Bridge

In the previous three chapters, I have investigated different aspects of the effect of particles on gas migration. Most recently in Chapter IV, I have shown that bubbles are significantly slowed in the crystal-rich magma relative to their free rise velocity in absence of crystals. I have also shown that the small bubble population observed in tephra is essentially stagnant and cannot account for the gas fluxes measured at

Stromboli, which are instead due to the rise of larger, mm-cm sized bubbles not or less frequently preserved in tephra. Next, in Chapter V, I combine the results from the previous three chapters to formulate a new model for the migration of gas through the crystal-rich magma at Stromboli and the normal Strombolian eruption mechanism that takes the effect of crystals into account.

CHAPTER V

SUMMARY: A NEW MODEL FOR GAS MIGRATION AT STROMBOLI VOLCANO AND THE NORMAL STROMBOLIAN ERUPTION MECHANISM

In this chapter, I bring together the results from Chapters II, III and IV as applicable to Stromboli volcano. I have shown in Chapter II that the slug model for the normal Strombolian eruption mechanism is unlikely considering the high crystallinity of Stromboli's upper magma body, and here propose a new model, developed in conjunction with Dr. Jenny Suckale (MIT, now at Harvard), that is based on my results and more in keeping with the geophysical and petrological data available for Stromboli. The mathematical modeling of stress-strain conditions described in this chapter was done by Jenny Suckale. She also did numerical experiments (Suckale at al., 2010) of gas slugs rising in a conduit with properties relevant to Stromboli volcano, which support the conclusion from my analogue experiments that slug flow is unlikely. Our studies combine to make a strong case for the inadequacy of the current Strombolian eruption mechanism. An in-depth version of our new model, focusing on the stress-strain modeling, is being prepared for submission with Jenny Suckale as first author, myself as second author, and Drs. Katharine Cashman and Bradford Hager (MIT) as co-authors.

1. A new model for normal Strombolian eruptions

In the prevailing model for the normal Strombolian eruption mechanism, explosions are attributed to the rise and bursting of large, conduit-filling gas bubbles

(slugs) at the free magma surface (see Chapter II section 2.2. for a complete discussion). When this slug model was first developed, it provided a convenient, simple explanation for observations, most notably the characteristic periodicity of the eruptions. However, new data indicating, especially, a high crystallinity of the upper magma (see Chapter I section 1) calls for a new model to explain the Strombolian eruption mechanism.

In Chapter II I proposed a new interpretation of the flow regimes occurring in the crystal-rich magma body at Stromboli volcano, in which bubbly flow occurs in the pore space between the crystals, with formation of dynamically opening and closing permeable pathways near the surface. The bubble population rising through the crystal-rich magma becomes enriched in small bubbles, both by splitting of large bubbles around the crystals and by trapping of small bubbles underneath crystals (Chapter III). The velocities associated with these small bubbles are so low that this bubble population can be considered essentially stagnant, and non-eruptive degassing at Stromboli is therefore best explained by the rise of larger bubbles, with dominant radii calculated between 3.6 and 6.1 mm (Chapter IV). Bubbles are slowed in the crystal-rich magma relative to their free rise velocities (Chapter IV) by a value that depends on their size and the bubble:crystal size ratio, which determines the splitting probability of the bubbles around crystals (Chapter III). Since the gas rising through the crystal-rich magma at Stromboli originates deep within the plumbing system (Burton et al., 2007b), this means that gas must accumulate at the interface between the deeper crystal-poor and the overlying crystal-rich magma body.

Jenny Suckale (MIT, now Harvard) has performed a simplified numerical simulation, which treats Stromboli's upper magma as a porous plug and models the stress

and strain on the plug induced by an accumulating gas pocket at its base. The plug has a depth of 300 m, representing the upper, most crystalline portion of the upper magma, and an ellipsoidal cross-section, matching the shape of Stromboli's crater terrace. The thickness of the plug was determined using MELTS software (Ghiorso and Sack, 1995; Asimow and Ghiorso, 1998) to model the crystallinity increase in the magma with decreasing pressure (depth below the free magma surface) at Stromboli (Figure 5.1.). The crystallinity increases gradually from ~30 MPa to the surface, reaching crystallinities > 50% at ~5 MPa, which is ~300 m depth assuming a density of 1500 kg/m^3 for the magma (bubbles + crystals + melt). We take this top part of the magma body, where crystallinities approach the critical packing fraction of Marsh (1981), as the thickness of the porous plug, and assume for simplicity that a sharp interface exists between the plug and a crystal-poor magma underneath it, beneath which rising bubbles accumulate as they encounter the slowing effect of the crystals in the plug. In reality, bubbles probably slow gradually as the crystallinity increases, and accumulate as a foam in the transition area where the crystallinity is increasing gradually, instead of coalescing to form an actual gas pocket. The stress buildup underneath the plug due to gas accumulation should be equal in both cases (Jenny Suckale, pers. comm.).

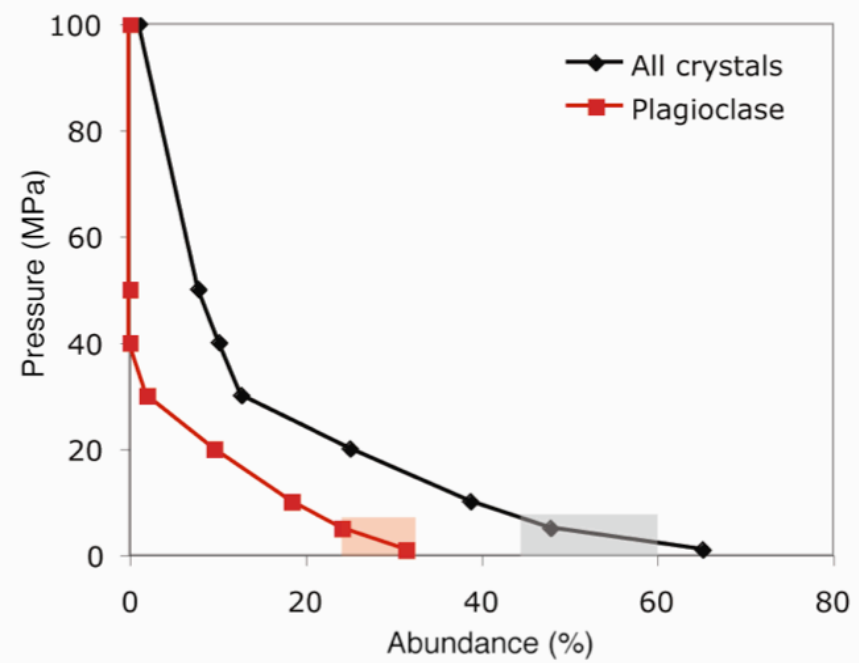

Figure 5.1. The increase of total crystallinity (diamonds) and plagioclase content (squares) with decreasing pressure (decreasing depth below the free magma surface) in the magma at Stromboli, modeled using MELTS (Ghiorso and Sack, 1995; Asimow and Ghiorso, 1998). The shaded areas highlight crystallinities observed in tephra and show the inferred thickness of the porous plug (0-5 MPa corresponds to ~300 m).

The model results indicate that gas will accumulate underneath the plug until the pressure exerted by the gas causes the plug to fail and a fracture forms through which gas can escape. The stress distribution in the plug strongly depends on the boundary conditions of the model. At Stromboli, normal eruptions occur preferentially from the NE and SW craters, while puffing predominates at the central crater (McGreger and Lees, 2004; Johnson, 2005, Landi et al., 2011), a geometry which can be reproduced by including a weak side on one side of the model, corresponding to the Sciara del Fuoco scarp (see Chapter I, Figure 1.1.). When gas is released during an eruption, the pressure drops, the crack heals and the cycle starts over again (Figure 5.2.).

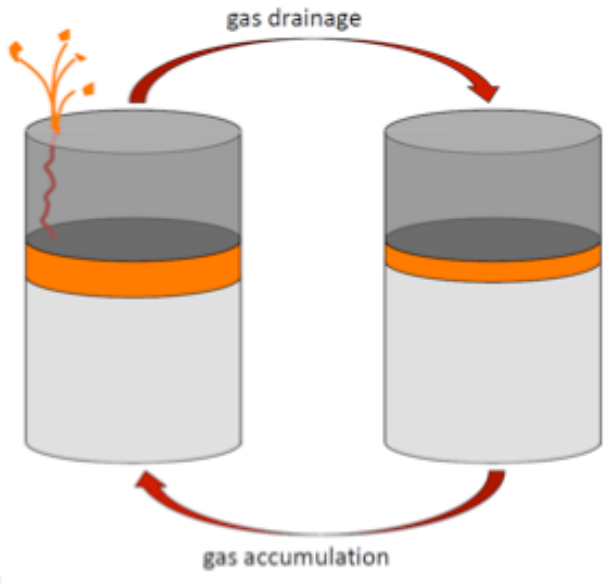

Figure 5.2. Schematic showing gas accumulation and pressure buildup underneath a crystalline plug as a mechanism for Strombolian eruptions. When the gas pressure underneath the plug builds to a critical threshold a fracture forms, releasing gas and expelling magma as a Strombolian eruption. When pressure is released, the crack heals and the cycle starts over. Light gray: crystal-poor magma in the lower plumbing system; dark gray: crystal-rich magma in the upper plumbing system; orange: accumulating gas layer at the base of the crystal-rich magma.

2. Gas accumulation rates

The accumulation rate of the gas pocket depends on the size of the accumulating bubbles. Bubbles of 3.6 mm radius rising through the crystal-rich magma at 7.5 m/day can account for the low end of the measured non-eruptive gas flux (see Chapter IV). The Stokes free rise velocity of bubbles of this size in a magma with the properties of the interstitial melt in Stromboli's upper magma body (Table 4.5.) is ~29.8 m/day. Taking this velocity as the bubble rise velocity in the crystal-poor magma beneath the plug gives that bubbles with a 3.6 mm radius are slowed ~4 times at the interface between the two

magma bodies. Since the system at Stromboli appears to be in a steady state (Armienti et al., 2007), the time-averaged total gas flux at the surface should equal the gas flux through the crystal-poor magma at depth. For the low end of the non-eruptive (passive + puffing) degassing flux at the surface measure by Allard et al. (1994), I calculated an equivalent of ~$1.0*10^5$ m^3/day at 5 MPa (the inferred pressure at the base of the plug) (Chapter IV). This flux accounts for ~90% of the total gas flux, with the other 10% expelled during eruptions (Harris and Ripepe, 2007), so that the total flux at depth should be ~$1.1*10^5$ m^3/day. With a bubble rise velocity of ~29.8 m/day and a total cross-sectional area of 33000 m^2 for the magma body (the approximate area of the crater terrace), this gives a vesicularity of 11.4% in the crystal-poor magma at depth assuming a uniform population of bubbles with 3.6 mm radius. This value is much lower than the 41% gas content in the plug measured on crystal-rich tephra in Chapter IV, which highlights the relative accumulation of bubbles in the crystal-rich system. Mori and Burton (2009) report an explosive gas volume of 1500-4100 m^3/explosion at atmospheric pressure, which corresponds to a gas volume of 30.4-83.1 m^3/explosion at 5MPa, converted with the ideal gas law assuming constant temperature (cf. Chapter IV section 7.3). At a gas flux of ~$1.1*10^5$ m^3/day this volume will accumulate in 0.4-1.1 min. A similar calculation for the high end of the measured non-eruptive gas flux ($6.1*10^6$ m^3/day at 5MPa) gives accumulation times of 0.01-0.02 min (0.4-1.1 s). These second to minute timeframes necessary to accumulate the gas masses expelled during eruptions are much smaller than the 10-20 min repose times between normal Strombolian explosions. According to this calculation, $7.8*10^2$-$9.4*10^4$ m^3 excess gas could build up between eruptions, which may give an indication of the pressure needed to fracture through the

crystal-rich plug, although the limited gas volume expelled during each eruption would indicate that the system is not actually in a steady state on the timescale of Strombolian eruptions but gas is continually accumulating at depth. This excess gas buildup may be released during the large paroxysmal eruptions that occur every ~2-3 years at Stromboli. Another possibility is that significant gas exsolution occurs at shallow depths inside the plug (perhaps driven by crystallization) so that the gas flux in the crystal-poor magma is lower than inferred from measured eruptive and non-eruptive fluxes.

3. Eruptive intensity

Changes in eruptive intensity at Stromboli have been interpreted as resulting from changes in gas flux at depth (Ripepe at al., 2008), a conclusion supported by our analysis in Chapters II and III. In light of the slug model, an increase in gas flux from deeper in the system would increase the accumulation rate of the gas pocket at the base of the plug. If the pressure needed to fracture the plug remains constant, this should cause more frequent Strombolian explosions. Phases of high intensity eruptive activity identified by Ripepe et al. (2002) are indeed characterized by frequent Strombolian explosions and rapid puffing. During these high-intensity phases, Ripepe et al. (2002) identify a change in the time delay between the infrasonic signal (generated when an explosion occurs) and the thermal signal (detected when the eruptive plume ascends into the thermal camera's field of view) that implies either increased gas jet velocities or elevated magma free surface levels. Increased accumulation rates of the gas pocket would lead to increased pressure buildup underneath the plug and could easily give rise to increased velocities of

the gas emanating from the crack during eruptions. An elevated magma free surface level would be the logical result of an increase in gas holdup in the system, which could result from both an increased thickness of the buoyant gas pocket during periods of rapid accumulation, and an increase in the amount of gas contained in the porous plug as a result of increasing gas flux (Chapter III). The latter interpretation is further supported by my observation in Chapter II that, although vesicularity locally varies with crystallinity, tephra clasts emitted during the more intense major explosions have overall higher vesicularities than those erupted during normal levels of activity.

The negative correlation between eruptive intensity and bubble number density in tephra clasts found by Colò et al (2010) begs the question of how bubble number densities relate to vesicularities. Indeed, Colò et al. (2010) interpreted lower bubble number densities as occurring during periods of higher gas contents in the magma (higher vesicularity), which promotes coalescence and leads to larger but fewer bubbles. My experimental results in Chapter III would suggest that bubble number densities (as well as vesicularities) should increase with increasing gas flux, due to increased splitting of larger bubbles and trapping of small bubbles beneath crystals, although the dimensional analysis in that chapter does indicate that these effects might not be as widespread at Stromboli as in my analogue experiments. Colò et al. (2010)'s and my results are reconcilable if coalescence occurs inside or at the base of the plug and splitting has a negligible influence on the resulting bubble population, which may indicate that crystals could actually promote coalescence, as is observed e.g. by Mena et al. (2005) in studies applicable to chemical engineering, but contrary to the experimental results of Chapter III. No clear correlation exists between bubble number density and vesicularity in the

Stromboli tephra samples used to investigate the variation of vesicularity with crystallinity in Chapter II (Figure 5.3.). It should be noted, however, that measurements of bubble number densities are very sensitive to the smallest observable bubble size, since small bubbles are the most abundant, while vesicularities are most sensitive to the largest bubble sizes in the population, which, although scarce, add a large volume of gas to the total. Both measurements are thus very scale dependent, and an in-depth analysis of bubble number densities and vesicularities in Stromboli tephra over a wide range of scales remains to be done. Although there is an apparent discrepancy in the trend of bubble number density with increasing gas flux, both studies agree that an increase in gas flux should lead to an increase in vesicularity, which would increase the gas holdup in the plug.

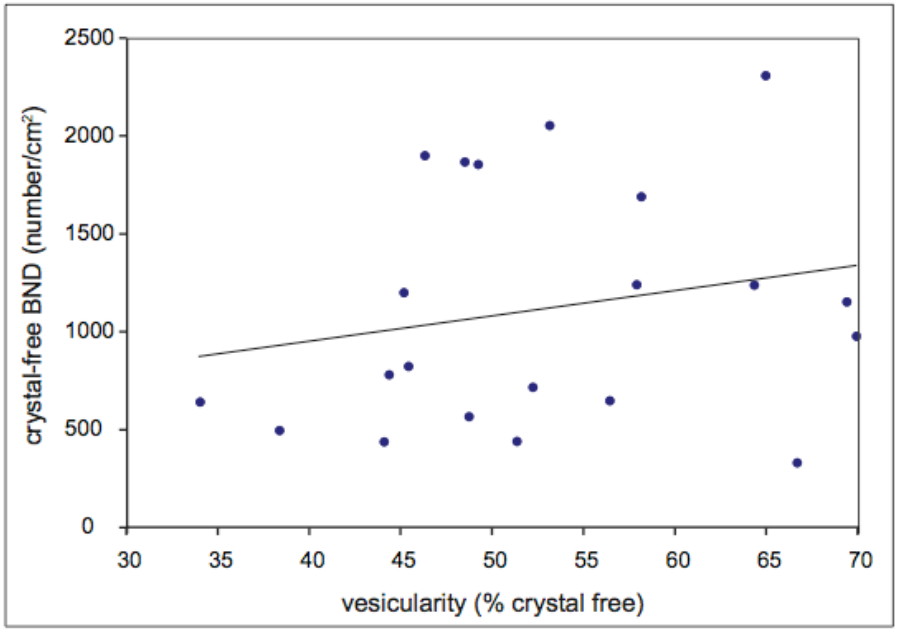

Figure 5.3. Bubble number density (number of bubbles per unit area of liquid+gas) and vesicularity (total amount of gas relative to liquid+gas area) in tephra samples from normal and major Strombolian eruptions. These samples are the same as those of Chapter II, Figure 2.10.

4. Conclusions

In general, the new "plug" model provides a simple and plausible alternative to the slug model as a working hypothesis for the Strombolian eruption mechanism (Figure 5.4.). Both models account for the episodicity of the eruptions; the slug model by the periodic rise and bursting of a gas slug, and the plug model by the buildup and release of gas pressure at the base of the plug. Unlike the slug model, our plug model incorporates the effect of crystals, and is thus reconcilable with petrological observations of high crystal contents in the upper magma body at Stromboli. Our model also explains the overpressure of the gas expelled during eruptions (Ripepe and Marchetti, 2002), and the depth at which the very long period (VLP) earthquake signal, which is associated with Strombolian eruptions, originates (220-290 m; Chouet et al., 2003; Marchetti and Ripepe, 2005; Harris and Ripepe, 2007b) corresponds well with the thickness of our inferred plug. The time delay between the VLP signal, which is thought to represent the formation of a slug at depth, and the infrasonic signal of the explosions requires gas ascent velocities of 10-70 m/s (Harris and Ripepe 2007b), unlikely for the rise velocity of a gas slug, but plausible as gas velocities in an opening crack in the plug model. In addition, the plug model may be able to explain the predominant occurrence of Strombolian eruptions from the NE and SW craters rather than in the center of the crater terrace, which is not addressed by the slug model. Our model also allows concurrent percolation of small bubbles through the porous plug and permeable pathway formation near the surface that is independent of the eruption mechanism, explaining the widespread and eruption-independent passive and active degassing observed at Stromboli. Finally, our

plug model provides a framework for logical interpretation of the effects of changing gas flux on the degassing regimes, that can explain observed correlations between eruptive intensity and both the infrasonic-thermal delay time (Ripepe et al., 2002) and vesicularities observed in tephra samples (Chapter II, and implied by Colò et al., 2010). We conclude that, although conceptually equally simple, our plug model provides a more plausible alternative to the slug model, that is better reconcilable with geophysical and petrological observations at Stromboli and incorporates non-eruptive degassing mechanisms.

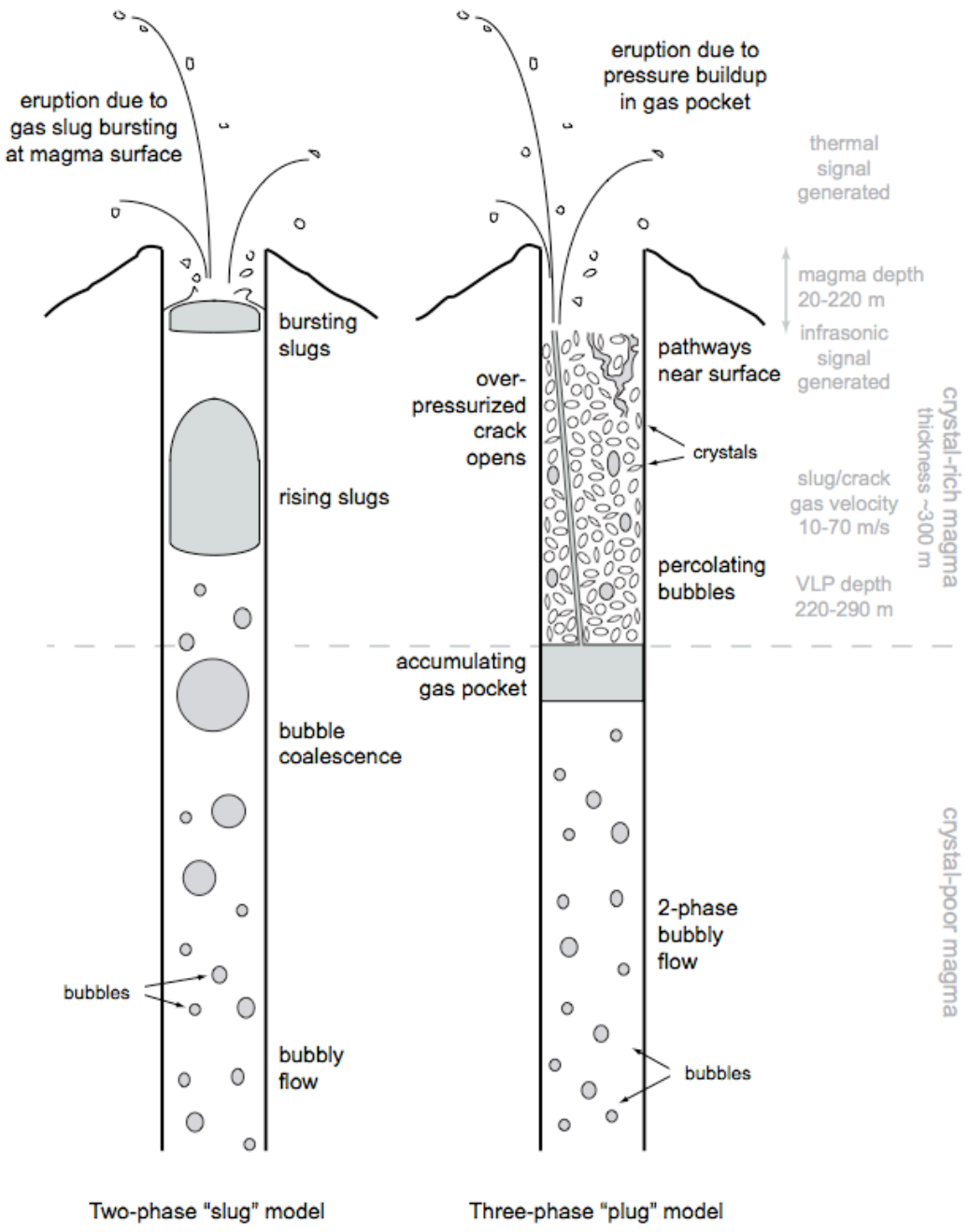

Figure 5.4. Summary schematic comparing the slug model and the plug model for the normal Strombolian eruption mechanism (not to scale). Key geophysical and petrological observations at Stromboli are shown in gray text. Depths are below the crater terrace. The range in depths of the free magma level is from Harris and Ripepe, 2007b. See text for other references. The slug model is based on the rise and bursting of conduit-filling gas slugs. The plug model is based on a cycle of pressure buildup and release due to gas accumulation underneath the crystal-rich magma body. Bubbly flow and pathway formation in the crystal-rich plug give rise to passive degassing and puffing activity respectively.

CHAPTER VI

CONCLUSIONS

This dissertation has addressed questions concerning the influence of crystals on gas migration through low-viscosity magmas. I here briefly look back at the research questions addressed, point out some opportunities for future work, and show how my work contributes to scientific knowledge in volcanology.

In the introduction I posed the questions:

- How do crystals influence gas migration in low-viscosity magmas, where gas can rise independently through the melt? What is the significance of the critical crystal concentration with respect to rising gas bubbles? What fluid properties do the bubbles "feel" as they percolate through the crystal-rich system?
- What are the physical mechanisms of gas percolation through the crystal-rich magma at Stromboli? What is the effect of crystals on the degassing efficiency?
- What is the effect of crystals on bubble populations? Do crystals aid or inhibit coalescence?
- How do crystals in high concentrations influence the eruptive style? How does this relate to the current model for the normal Strombolian eruption mechanism? How would large gas slugs migrate through a magma with ~50 vol.% crystals?

I have shown that crystals in low concentrations increase the bulk fluid properties, leading to flow regimes similar to those observed in two-phase systems at higher viscosities, but that flow regimes are significantly modified at high crystallinities. The transition from the annular flow regime to pathway flow is gradual and occurs at ~40-45% in my experiments. I speculate that this is the point at which the crystals start to touch, but a detailed study of the concentration at which the transition begins and its rheological significance remains to be done and should include particles of different shapes. To better compare experiments to volcanic systems where crystals have a variety of shapes and sizes, populations of particles with a range in sizes should also be used.

I have shown that small bubbles can percolate through the liquid in the pore space between the crystals. This percolation bubbly flow occurs when the packing concentration of the crystals is reached, but a detailed investigation of the crystal content at the transition should again include particles of different shapes and size distributions. These percolating bubbles will "feel" the fluid properties of the interstitial liquid, but are hindered in their rise by the presence of the crystals. Small bubbles can get trapped beneath crystals; bubbles larger than the crystal size can split around crystals. Coalescence is not observed in my experiments but may occur at Stromboli and account for the inverse correlation between bubble number density and eruptive intensity observed by Colò et al. (2010). An investigation of the influence of particles on coalescence should use liquids with Bond and capillary numbers closer to those of magma or at least $<< 1$.

Measurements of gas holdup in a bubbly liquid with varying particle concentration show that crystals increase the degassing efficiency. This is further

supported by image analysis on tephra samples from Stromboli which show an inverse correlation between vesicularity and crystallinity. The physical mechanisms leading to this change in degassing efficiency need further investigation. One possibility is that particle-induced coalescence allows for larger and faster bubbles or the formation of permeable networks through which gas could escape. The need for an investigation of the influence of particles on the coalescence of rising bubbles is mentioned in the previous paragraph. Bubble expansion during rise through the magma may aid in bubble coalescence as well. This is addressed in Appendix A, where I summarize preliminary results from a study investigating the effect of crystals on bubble expansion and gas loss.

One significant contribution of my work to volcanology is the insight that bubble populations in crystal-rich tephra are not simply the result of different stages of bubble nucleation and growth. Syn-eruptive expansion and vesiculation have long been recognized as modifying the bubble populations observed in tephra (e.g. Blower et al., 2002; Klug et al., 2002). I have shown that crystals can influence bubble shapes and size distributions as well. Large deformed bubbles observed in tephra can result from interaction with crystals as well as from coalescence. Small bubbles can result from enrichment due to splitting and bubble trapping beneath crystals as well as from late-stage nucleation. These findings show that bubble populations in crystal-rich systems cannot directly be used to extract information on degassing history and timing of bubble nucleation, as is done for crystal-poor systems (e.g. Toramaru, 1989 and 1990; Blower et al., 2001).

Another important contribution, not just to volcanology but to studies of bubble rise in porous media in general, is the recognition that most current studies of Taylor

bubble rise in tubes, where rise is controlled by the rate of liquid flow in the film between the bubble and tube wall, are not applicable to bubble rise in porous media. Bubble rise through capillaries that are open on both ends so that liquid can flow around the outside of the tube are a better analogue, and I have shown that the rise velocities of bubbles in such systems compares well to measurements of bubble velocities in a particle suspension. An in-depth theoretical description of bubble rise in such open tubes, which includes all relevant forces acting on the bubble (e.g. surface tension) remains to be done. Future studies should also focus on expanding this situation to liquids with different density, viscosity and surface tension, and to bubbles that are smaller than the tube, as well as to very long bubbles ($Req/R > 3$), situations not addressed in Chapter IV.

Possibly the most significant contribution of this dissertation research, however, lies in the new model developed in Chapter V for the normal Strombolian eruption mechanism. I have shown that the rise of large gas slugs through Stromboli's crystal-rich upper magma is unlikely, highlighting the need for a new model that takes crystallinity into account. The current slug model has dominated our understanding of conduit processes in explosive basaltic volcanoes for several decades. I have shown that the high crystallinity at volcanoes exhibiting this eruptive style may not only influence, but actually cause the explosivity of the eruptions. The recognition that crystals can play a crucial role in controlling gas migration and modifying the eruptive style provides a whole new perspective that may enable significant advance in understanding, and predicting, eruptive activity at basaltic volcanoes.

APPENDIX A

PRELIMINARY EXPERIMENTS ON THE INFLUENCE OF PARTICLES ON GAS EXPANSION IN A VISCOUS LIQUID

This work was done in conjunction with Laura Farrell and Drs. Alison Rust and Jeremy Phillips from the University of Bristol, UK. Data collection was done by me with help from Laura Farrell (then MS student at the University of Bristol). All data analysis was done by me. Drs. Alison Rust and Jeremy Phillips provided guidance for this project. This is work in progress; I will continue this work during a 3-month post-doc position at the University of Bristol in Fall 2011. I have started a collaboration with Mattia Pistone (ETH Zurich, Switzerland) to investigate the applications to volcanic processes.

1. Motivation

In the main body of this dissertation, I have studied the rise of bubbles through magma, assuming bubble sizes do not change during rise. In reality, pressure decreases as the bubbles rise from a certain depth within the magma column to the surface, which will drive gas expansion. In low-viscosity magmas such as at Stromboli, bubbles can expand more or less freely to balance the change in pressure. If the bubble rise velocity is fast or the magma viscosity is high, expansion will be impeded, leading to overpressure buildup inside the bubbles. Bubble growth and coalescence in the magma at Stromboli has been proposed to lead to the formation of permeable pathways through which gas can passively escape from the system (Burton et al., 2007; Polacci et al., 2008 and 2009). In

Chapter III I showed that large bubbles rising through a particle-rich system can split into smaller bubbles around the particles, leading to an increase in the bubble number density in the system and enrichment of small bubbles. This effect is opposite from that of coalescence, which would lead to a decrease in the number of bubbles present and an increase in the number of large bubbles relative to smaller ones. Although not observed in the experiments in Chapter III, particle-induced coalescence has been seen in chemical engineering studies (e.g. Mena et al., 2005). Bubble expansion in particle-free systems promotes gas loss both by increasing the bubble size, leading to an increase in bubble rise velocity, and by increasing the probability of coalescence (due to increased proximity of the bubbles) and the formation of permeable pathways. In this study, my collaborators and I address the effect of particles on bubble expansion and gas loss. We use a setup similar to that of Namiki and Manga (2008), who studied decompression-induced fragmentation and the development of permeable networks in a particle-free system. We use a shock tube to decompress a bubbly viscous liquid with varying proportions of solid particles (magma analogue). In addition to particle concentration, we also vary initial bubble content and amount of decompression. We keep track of whether or not gas escape occurs in our experiments and identify which parameters play the largest role in promoting gas loss. This study is work in progress. We here present an overview of our preliminary results.

2. Methods

To investigate the factors influencing gas loss in expanding viscous systems, we perform decompression experiments on a bubbly viscous liquid (Tate and Lyle's Golden Syrup) with varying proportions of solid particles (cane sugar crystals). The sample is inserted into the bottom of a 1-meter long glass tube with 2 cm internal radius, the top end of which is connected to a vacuum chamber (Figure A.1.). The physical properties of Tate and Lyle's Golden Syrup have been described by Llewellin et al. (2002). At our experimental conditions, the consistency of the syrup (the viscosity at a strain rate of $1s^{-1}$) is 60-120 Pa s, the syrup density is 1.46 ±0.06 g/cm^3 (based on four measurements) and the density of the sugar crystals is 1.47 ±0.12 g/cm^3 (based on two measurements). The sugar crystals are chosen because of their similarity in density with the syrup. Two populations are used: large crystals, which are rectangular with aspect ratio ~2:1 and length ~3-5 mm, and small crystals with aspect ratio ~1:1 and length ~0.5-1 mm. Micron to mm-sized bubbles are added to the syrup by aerating (air bubbles) or by reaction with $NaHCO_3$ (baking soda). Golden Syrup is slightly acidic and reacts with the baking soda over time to form CO_2 bubbles. We mixed baking soda with syrup and let is stand for at least 12 hours before using, to ensure that the reaction had completed. Initial crystal and bubble concentrations, sample volume and pressure drop for the experiments used in this study are summarized in Table A.1. In experiments 1 through 8 the pressure in the vacuum chamber and glass tube was lowered gradually, causing the gas bubbles in the syrup to expand gradually as well. In experiments 9 through 61, a gate between the tube and the vacuum chamber was closed before the pressure was lowered (Figure A.1.). Once

the vacuum chamber was at the desired pressure, the gate was opened, allowing the gas in the tube and sample to suddenly decompress from atmospheric pressure down to the vacuum chamber pressure. Experiments were videotaped and pressure was recorded simultaneously for most experiments. Changes of the height (volume) of the sample with pressure were measured on video frames. Crystals were added in experiments 2, 4, 45, 58 and 59 (25% by volume) and experiments 46, 47 and 61 (50% by volume). Experiments not listed in Table A.1., including some with 30 and 40 vol.% crystals, have no pressure data associated with them, either because no data was recorded or (in most cases) data was recorded but the recording was bad. These experiments are not useful for our current analysis.

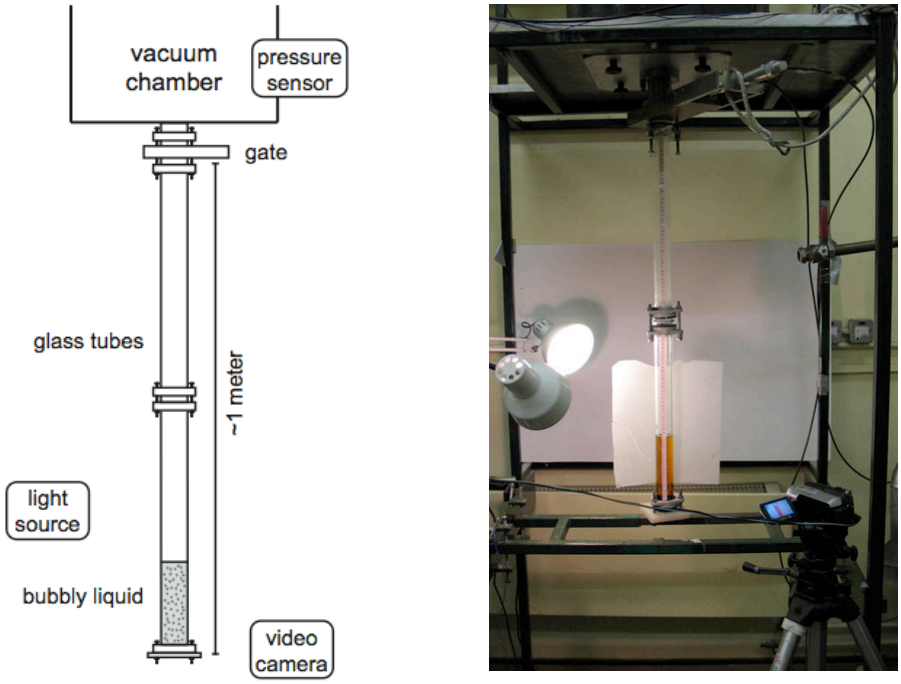

Figure A.1. Schematic (left) and photo (right) of the experimental setup used in this study.

Exp. #	Description	Initial mixture volume cm^3 (±3)	Crystal content % of total (±12)	Initial vesic. % crystal free (±1.5)	Pressure drop mbar (±25)	Decompression rate
1	aerated	194	0	7.2	926	slow
2	aerated	192	25 (large)	2.2	920	slow
3	aerated	183	0	5.9	923	slow
4	aerated	124	25 (large)	6.5	927	slow
5	5 wt% $NaHCO_3$	194	0	28.4	880	slow
6	5 wt% $NaHCO_3$	126	0	24.4	880	slow
8	pure syrup	198	0	0.3	825	slow
9	pure syrup	198	0	0.0	462	fast
10	pure syrup	198	0	0.0	600	fast
11	pure syrup	198	0	0.0	715	fast
12	pure syrup	198	0	0.2	808	fast
38	aerated	225	0	11.7	789	fast
39	aerated	219	0	11.3	898	fast
40	aerated	211	0	10.7	882	fast
41	aerated	222	0	6.4	841	fast
42	aerated	219	0	6.3	885	fast
43	aerated	219	0	5.9	933	fast
45	aerated	228	25 (large)	8.8	871	fast
46	aerated	221	50 (large)	8.1	884	fast
47	aerated	219	50 (large)	7.8	883	fast
51	aerated	204	0	10.9	892	fast
55	aerated	232	0	12.4	887	fast
56	aerated	220	0	11.5	893	fast
57	aerated	218	0	10.1	887	fast
58	aerated	225	25 (small)	6.4	888	fast
59	aerated	222	25 (small)	5.7	884	fast
61	aerated	233	50 (small)	13.0	884	fast

Table A.1. Summary of experimental conditions. Sixty-one experiments were done in total. Experiments not listed are ones for which pressure data is missing.

To establish whether or not gas was lost from the system during decompression, we need a reliable way to measure gas volumes (or volume fraction) at the start and end of our experiments. Due to large uncertainties in liquid and crystal densities, and especially in crystal concentration (25% relative error) in our analogue liquids, large errors will result from the direct calculation of gas volume from the total volume and the weights and densities of the liquid and crystal fraction. To reduce uncertainties we use the following alternative method of calculating the initial gas content in our samples.

If gas expansion occurs according to the ideal gas law, then $P_{initial}V_{gas,initial}$ should equal $P_tV_{gas,t}$ at each time t during the experiment. Since $V_{gas} = V_{total} - V_{liquid} - V_{crystals}$, it follows that $V_{total} = [(P_{initial}/P)V_{gas,initial}] + V_{liquid} + V_{crystals}$, so that all data points for a single experiment should plot on a straight line with slope $V_{gas,initial}$ on a graph of V_{total} versus $P_{initial}/P$. Note that we do not *a priori* need to know V_{liquid} and $V_{crystals}$ to determine the initial gas volume in this way. Most of our experiments do indeed form a straight line, indicating that the assumption of ideal gas is valid (Figure A.2.). The final gas volume is $V_{gas,end} = V_{gas,initial} + (V_{total,end} - V_{total,initial})$ since the increase in total volume during decompression is only due to gas expansion.

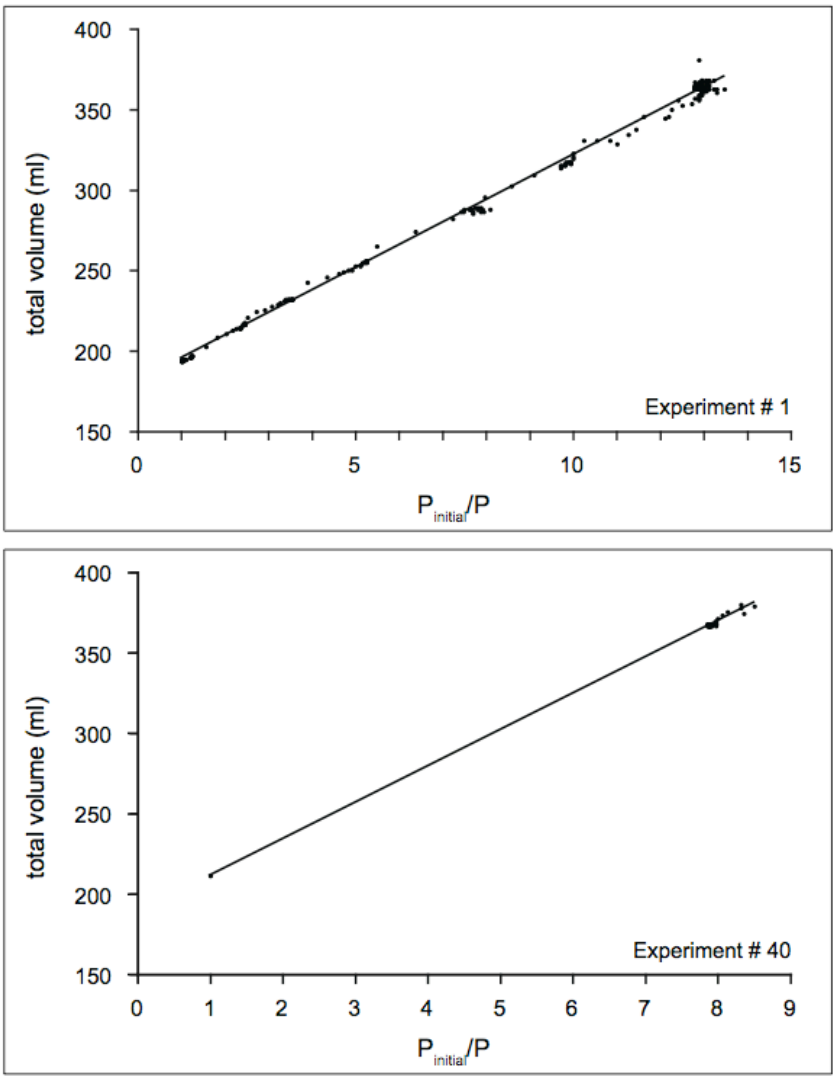

Figure A.2. Most of our experiments follow a straight line on a plot of V_{total} versus $P_{initial}/P$. Examples are shown for experiments 1 and 40. Experiment 1 was decompressed slowly, so that data points were taken for the whole range of pressures from atmospheric ($P_{initial}/P = 1$) to the minimum pressure (maximum $P_{initial}/P$). In experiment 40 we used the gate to suddenly decompress the sample from atmospheric conditions to low pressure, so that data points only exist at these two extremes.

3. Experimental results

Deviations from ideal gas behavior indicate a change in the amount of gas present in the system. If no change in amount of gas occurs, $PV_{gas}/P_{initial}V_{gas,initial} = 1$ at all pressures and thus at all times during the experiment, and a plot of $PV_{gas}/P_{initial}V_{gas,initial}$ versus time should be a horizontal line. If gas loss starts occurring at some point during the experiment, the line should bend downwards towards $PV_{gas}/P_{initial}V_{gas,initial} < 1$. Both of these situations occur in our experiments (Figure A.3.). In some cases, the line curves upwards to $PV_{gas}/P_{initial}V_{gas,initial} > 1$, indicating addition of gas into the system during the experiment. This happens for experiments in which the bubbles were created by reaction with $NaHCO_3$, and indicates continuing chemical reaction with the syrup as pressure decreases. Gas gain is also observed in experiment # 2 and probably indicates a leak in the seal at the base of the tube containing the sample.

If gas loss or gain occur during an experiment, $P_{end}V_{gas,end}/P_{initial}V_{gas,initial}$ at the end of the experiment (at the lowest pressure) will be less than or greater than one respectively. Comparing this end value for all our experiments enables us to investigate the influence of the different parameters varied between experiments on gas escape (Figure A.4.). Propagation of our experimental error shows that the standard error of $P_{end}V_{gas,end}/ P_{initial}V_{gas,initial}$ is 0.27, shown by the gray shaded region around the ideal gas line ($P_{end}V_{gas,end}/ P_{initial}V_{gas,initial} = 1$) on Figure A.4. Although experiments with 50% crystals are systematically low, all symbols are within the gray shaded region, indicating that we cannot conclusively demonstrate gas loss in any of our experiments. We preliminarily conclude that high crystal concentrations might encourage gas loss from the

sample. However, experiments with a wider range in vesicularities and perhaps larger pressure drops need to be done to induce further gas loss and verify this.

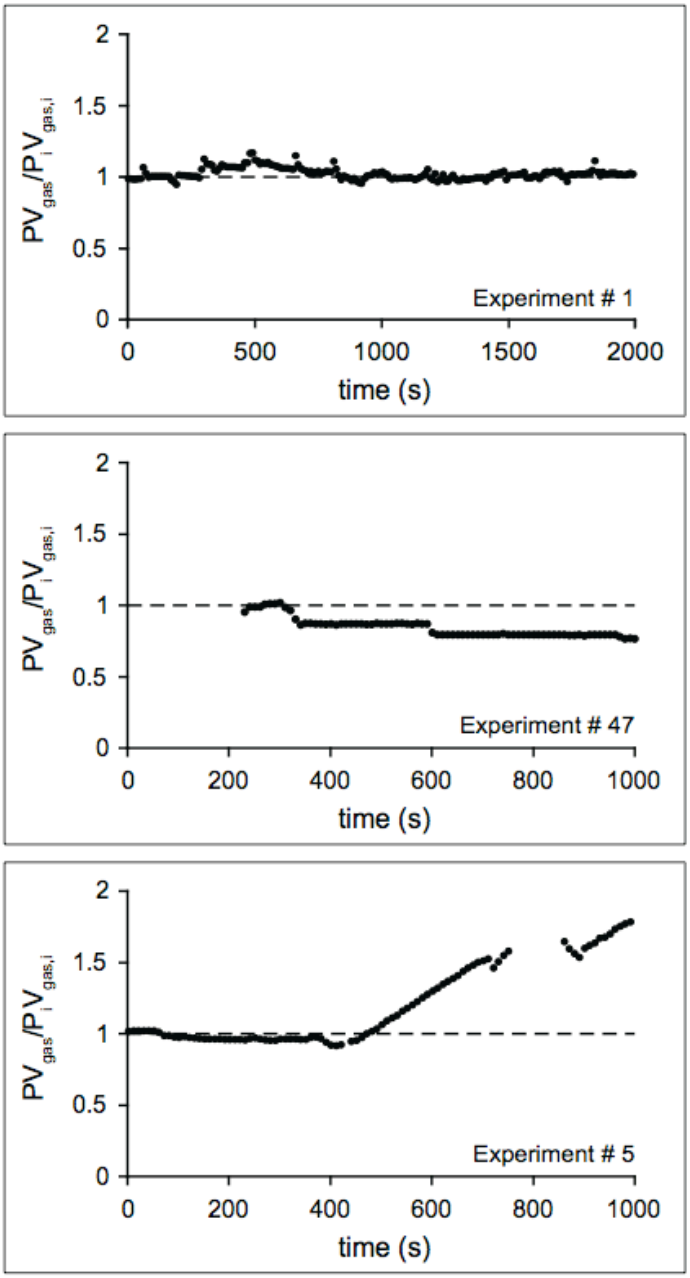

Figure A.3. $PV_{gas}/P_{initial}V_{gas,initial}$ versus time for three experiments showing constant amount of gas (top; experiment # 1), gas loss (middle; experiment # 47) and gas gain (bottom; experiment # 5).

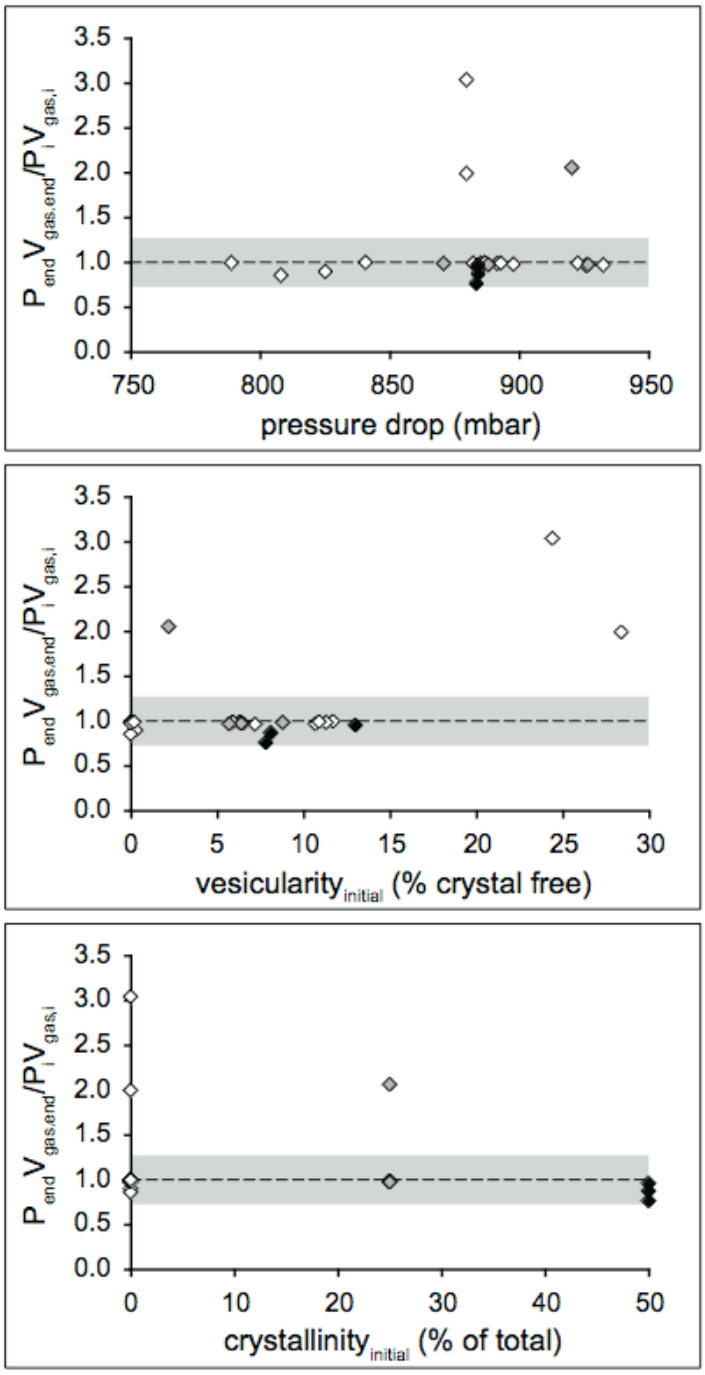

Figure A.4. Variation of PV_{gas}/ $P_{initial}V_{gas,initial}$ at the end of the experiments in Table A.1. with pressure drop, initial vesicularity, and initial crystallinity. White symbols: crystallinity = 0%; gray symbols: crystallinity = 25%; black symbols: crystallinity = 50%. The gray shaded area indicates the experimental error around the ideal gas line, where $P_{end}V_{gas,end}$/ $P_{initial}V_{gas,initial}$ = 1. Experiments within this shaded area do not demonstrate significant gas loss or gain. Symbols plotting above this region indicate addition of gas into the sample during the experiment. Symbols plotting below this region (none in our current study) indicate gas loss from the sample.

4. Future work

Although our preliminary work is inconclusive, an inverse correlation between crystallinity and end vesicularity is observed in experiments on samples with magmatic compositions in which vesiculation is induced in a melt with different starting crystal concentrations (Mattia Pistone, pers. comm.). Crystallization, which would induce further gas exsolution, does not occur during these experiments, so that the change in end vesicularity observed is only a result of the different starting crystallinities. This result gives credence to our preliminary conclusions and provides further motivation for an extension of our current work to higher starting vesicularities and larger pressure drops. The possibility of enhanced gas loss in high crystallinity magmas is interesting since it is opposite from the effect of the velocity reduction in particle-rich systems discussed in Chapter IV, which would lower the gas flux through the system. The next question is then whether gas loss is a result of bubble rise and bursting at the free liquid surface or of coalescence of bubbles to form permeable networks through the sample. This can be addressed by adding a second pressure sensor, measuring pressure at the base of the sample as well as above it, following the method of Namiki and Manga (2008). Another question that should then be addressed is the minimum particle concentration necessary to enhance gas loss, as well as how much gas loss occurs and how this depends on particle concentration for different particle shapes and sizes, aiming to understand the mechanism of gas loss enhancement. I plan to continue this work and address these three questions, and compare my results with the experiments of Mattia Pistone during a three-month post-doctoral position at the University of Bristol in September-December 2011 in

conjunction with Alison Rust and Jeremy Phillips (University of Bristol, UK) and with Mattia Pistone (ETH Zurich).

APPENDIX B

IMAGE ANALYSIS TECHNIQUES

To determine characteristics of the bubble and crystal populations in Stromboli's crystal-rich magma, we analyze images of two-dimensional thin sections through crystal-rich tephra from this volcano, ejected during normal Strombolian eruptions. Images from thin section scans or scanning electron microscopy (SEM) can be used. First, bubbles and crystals are manually outlined and highlighted in different colors in Adobe® Photoshop®. Automated processes do not correctly identify crystals and bubbles since the background (matrix of glass and microlites) is not uniform and often contains colors or shades present in the bubbles and crystals, outlines of the crystals are often fuzzy, and thin bubble walls are not usually preserved completely and need to be drawn in manually. The bubble and crystal populations are then selected and saved with two different grayscale values in a new image. This workflow is illustrated in Figure B.1. for a region from a thin section scan from tephra collected by Livia Colò (University of Florence, Italy) on 2 July 2009. The grayscale image of bubbles and crystals is then thresholded separately for the bubble and the crystal populations, and converted to a binary image from which object sizes and shape characteristics can be extracted.

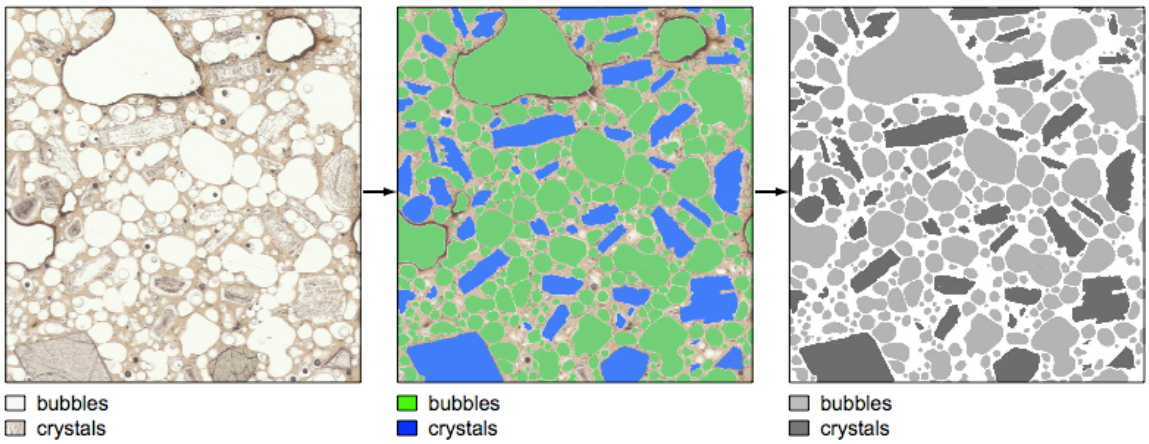

Figure B.1. Extracting bubble and crystal populations from a thin section scan (STR090702a_a_C). See text for explanation.

1. Bubble and crystal size distributions

Shapes and sizes of the bubbles and crystals in our images can be extracted in two different ways. For the analysis in Chapter III, we use the image analysis software ImageJ (Abramoff et al., 2004). In Chapters II and IV, we use the image analysis toolbox in MATLAB® (The MathWorks, Natick, MA, USA) to write a code to extract object properties (given in section 3 of this Appendix). Both methods are equivalent. We extract the two-dimensional areas of the bubbles and crystals and use these to calculate bubble equivalent radii (radius = $\sqrt{(\text{area}/\pi)}$, assuming circular), and crystal equivalent width (width = $\sqrt{(\text{area})}$, assuming square). In Chapter IV, we use the long axis of the best-fit ellipse to approximate the length of each crystal. From the parameters for each object, we can create frequency plots representing the size distributions of these properties for all bubbles and crystals in our images. Many other shape parameters, such as aspect ratio, circularity and circumference can be extracted for each bubble and crystal, but these are

not used in this dissertation. When characterizing object shapes, we exclude bubbles and crystals on the edges of the images, since these are not complete and sizes of these partial objects will bias the distributions. We calculate the crystallinity (crystal content) of each image as the percentage of the total image area taken up by crystals, including the ones on the image edges (crystallinity = $(100*A_{crystals}) / A_{total}$). We calculate the crystal-free vesicularity (bubble content) as the percentage of space taken up by bubbles in the total image area minus the area taken up by the crystals (vesicularity = $(100*A_{bubbles}) / (A_{total}-A_{crystals})$), where the area taken up by bubbles again includes the ones on the image edges.

To convert the two-dimensional bubble size distributions extracted from thin section images to three dimensions, we follow the method of Mangan et al. (1993). We divide all bubble sizes by 0.85 to correct for the fact that random slices through a sphere will yield apparent radii that are smaller than the true bubble radius. We divide the number of bubbles per unit area in each size class by the median bubble radius in that size class to get the number of bubbles per unit volume, which corrects for the fact that small bubbles are less likely to be intersected by a two-dimensional plane than large ones and will be relatively underrepresented in the distribution. Mangan et al. (1993) estimated the error of their method to be no more than ±25%.

2. Crystal spacing

The distribution of approximate distances between crystals in thin section scans from Stromboli tephra is used as the distribution of tube widths for the numerical model in Chapter IV. These distances are extracted in the MATLAB® code given in the next

section. The method is illustrated in Figure B.2. To find the inter-crystal distances, we first find the (carthesian) coordinates of the centroids (center of mass) for each crystal. Using the centroid to describe the crystal locations, we can define an area around each centroid that is closer to it than to any other centroid in the image. The boundaries of these areas define the so-called Voronoi polygons. To find the distances between adjacent centroids, we use a triangulation so that the triangulation lines are bisected perpendicularly by the Voronoi edges. This triangulation, called the Delaunay triangulation, has the additional property that the circumcircle associated with each triangle contains no other centroids. We refer to the MATLAB® help file (R2010b, The MathWorks, Natick, MA, USA) for additional information. Since the triangulation is done between the centroids and not the crystals as a whole, triangulation lines can crosscut crystals in some cases. These crosscutting lines do not connect adjacent crystals and need to be removed from the triangulation, which is done interactively in the MATLAB® code. The lengths of the remaining triangulation lines represent the distances between the centroids, calculated as $\sqrt{[(x_2-x_1)^2 + (y_2-y_1)^2]}$, where (x_1,y_1) and (x_2,y_2) are the coordinates of the begin- and endpoints of the line. Part of these lines is in the crystal interior, between the centroid and crystal edges, and not in the pore space. We estimate this part as the crystal equivalent radius ($\sqrt{(\text{area}/\pi)}$) and subtract this value for the crystals on the begin- and endpoint of each line from the line length to give an estimate of the inter-crystal distance (the diameter of the tubes in Chapter IV). Because this estimate assumes the crystals are spherical, it can be too large for elongated crystals in some directions so that small distances between adjacent centroids can become less than zero when this value is subtracted. We set these negative values to 0.1 micron (a visual

estimate of the smallest crystal spacings, which lies within our smallest bin size) to get the final distribution of tube widths.

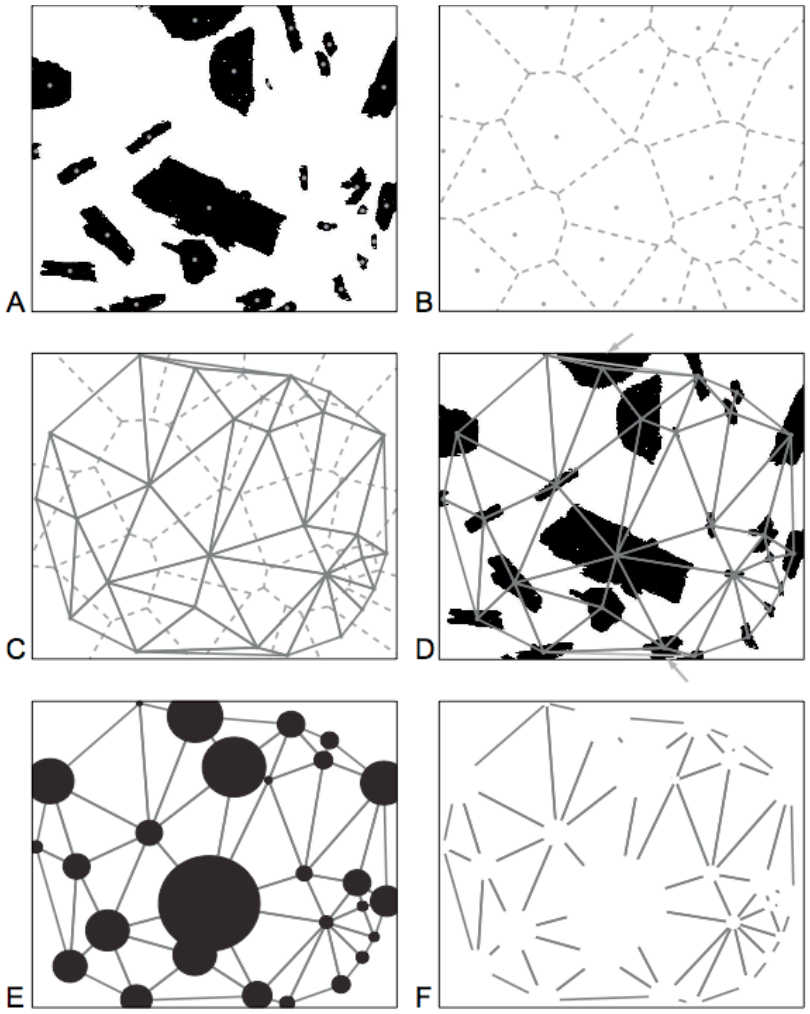

Figure B.2. Figure illustrating how crystal spacings are extracted, shown for sample STR070718-19d_A, collected on the morning of 19 July 2007 by Marco Pistolesi, University of Pisa, Italy. A: crystals with their centroids shown in gray; B: Voronoi polygons around the centroids; C: Delaunay triangulation between the centroids (solid lines) shown in addition to the Voronoi polygons (dashed); D: the Delaunay triangulation shown on the original image of the crystals, with lines that crosscut crystals marked by the gray arrows; E: crosscutting Delaunay lines removed and crystals represented by circles with the same area equivalent radius around the centroids; F: subtracting the equivalent radius for crystals on the start- and endpoint from each triangulation line finally gives the inter-crystal distances.

3. MATLAB® code

This script was coded in MATLAB® version R2010b (The MathWorks, Natick, MA, USA) on a Macintosh computer.

```
% Name:     image_distances.m
% Author:   Isolde Belien
% Date:     May 2011
% Goal:     Find frequency distribution of pore widths and bubble sizes
%           from grayscale images of bubbles and crystals (fotoshopped
%           from thin section scans)
% Input:    A text file called filelist.txt containing the names of the
%           image files. The text file and all the grayscale images and
%           this code need to be present in the current directory
% Output:   Histograms of pore radii (crystal spacing/2), crystal
%           lengths and bubble equivalent radii extracted from all
%           images, plus variables:
%   - porewidths: all pore widths from all images (mm)
%     Widths are calculated as the distances between the crystal
%     centroids reduced by the crystal equivalent radii. Since crystals
%     are in reality non-spherical, widths can end up negative. We set
%     all widths that are =< 0 to 0.1 micron
%   - poreradii: porewidths/2
%   - porearea: crystal-free area in each image, in order listed in
%     filelist.txt (mm^2)
%   - porespace: porearea expressed as a fraction of the total image
%     area, order cf. filelist.txt (fraction)
%   - crystallengths: major axis lengths of the interior crystals in
%     all images (mm)
%   - bubbleradii: equivalent radii of all interior bubbles (not on
%     edges) in all images, cumulatively ordered as labeled on the
%     images (mm)
%   - bubblearea: total area of bubbles (including ones on edges) in
%     each image, in order listed in filelist.txt (mm^2)
%   - bubblespace: fraction of pore space that is taken up by bubbles
%     in each image, order cf. filelist.txt (fraction)
%   - bubblespaceavg: average value of bubblespace in all images
%     (fraction)
%   - mean of the probability density function fit to the histograms
%     (exponential for both distributions)
%
%   Bubble, crystal and pore size distributions are input for code
%   capillary_vertical_new.m (models bubble rise velocity through a
%   porous medium


files = importdata('filelist.txt');
```

```
%% PORE WIDTH AND CRYSTAL SIZE DISTRIBUTION

numxtals = 0; % Number of labels already used for labeling crystals
porewidths = []; % Vector containing all pore widths for all images
% (cumulative)
crystallengths = []; % Vector containing lengths of all interior
% crystals for all images
porearea = zeros(length(files),1); % this vector will get filled in the
% loop
porespace = zeros(length(files),1); % this vector will get filled in
% the loop

for name = 1:length(files)

    % Import image and extract crystals
    image = imread(files{name,1});
    BW = im2bw(image,0.55); % keeps only crystals

    % We need to invert this image so that object pixels = 1 and
    % background pixels = 0
    nonzero = find(BW); % finds all nonzero pixels
    zero = find(BW==0); % zero is black
    BW(nonzero) = 0;
    BW(zero) = 1;

    % Show image (inverted = visally more intuitive)
    figure('Name','crystals','NumberTitle','off')
    imshow(~BW)
    hold on

    % Find the sizes and centroids (center of mass) of the crystals
    [L,num] = bwlabel(BW);
    stats =
    regionprops(L,'Area','Centroid','EquivDiameter','MajorAxisLength');
    % area in pixels; centroid as x and y coordinate
    labels = (1:num)';
    labels = labels+numxtals; % Number objects cumulatively on all
    % images
    centroids = cat(1,stats.Centroid); % coordinates of the centroids

    % Plot the centroids and object numbers on the image and save it
    plot(centroids(:,1),centroids(:,2),'g.')
    hold on
    for count=1:num
        text(centroids(count,1),centroids(count,2),sprintf('\t\t\t%g',
        labels(count,1)),'Color','g','FontSize',12,'FontWeight','b',
        'HorizontalAlignment','left')
    end
    hold on
    filename = files{name,1};
    truncate = regexp(filename,'composite');
    uimagename = filename(1:truncate-1);
    text(5,15,sprintf('%s\t\t%s',uimagename,'crystals'),'Color','g')
    hold on
    input('Please save this image and then hit return (do not close the
    image)');
```

```
% Find the Delaunay triangulation for the set of centroids
% "The Delaunay triangulation of a set of points is a triangulation
% such that the unique circle circumscribed about each triangle
% contains no other points in the set." (from MATLAB help)
DT = DelaunayTri(centroids(:,1),centroids(:,2));
% DT.X(:,:) gives the x and y coordinates of the centroids, in
% order in which labeled on figure
triplot(DT,'g')
hold on

% Remove lines that cross-cut other crystals
% This happens because the triangulation is between the centroids
% and not the objects as a whole. Need to visually check which
% ones, then find and remove them. The edges of the triangulation
% are
e = edges(DT); % lists pairwise indices (as labeled on fig) of the
% points connected by edges
% Find and remove pairs of points; get point pairs from user (read
% off current figure)
numlines = input('How many lines need to be removed?');
if isempty(numlines)
    numlines = 0;
end
if numlines>0
    for line = 1:numlines
        p1 = input(sprintf('%s%g%s','For line ',line,', give number
        of startpoint'));
        p2 = input(sprintf('%s%g%s','For line ',line,', give number
        of endpoint'));
        p1 = p1-numxtals;
        p2 = p2-numxtals;
        [row,col] = find(e(:,1)==p1 & e(:,2)==p2);
        e(row,:)=[];
    end
end

% Find the distances between the remaining pairs of points
% End-points of the lines with these distances are listed in e
first = e(:,1); % start point for distance calculation
last = e(:,2); % end point for distance calculation
distances = sqrt(((centroids(last,1)-
centroids(first,1)).^2)+((centroids(last,2)-
centroids(first,2)).^2));

% Limit these distances to inter-crystal space
% Parts of these lines between centroid and crystal edges are in
% the crystal interior and not in the pore space. Use the crystal
% equivalent radius as estimate for how much of each crystal this
% is.
diameters = cat(1,stats.EquivDiameter); % Get crystal equivalent
% diameter
radii = diameters./2;
distances = distances-radii(e(:,1))-radii(e(:,2)); % Reduced
% distances in pixels

% Convert distances to mm; get image scale from user (can get in
```

```
    % Photoshop > Image > Image Size...
    scale = input('Enter scale of image in px/mm (default is 153.7292
    px/mm)');
    if isempty(scale)
        scale = 153.7292; % px/mm
    end
    distances = distances./scale; % pore widths in mm
    % Set distances < 0 to 0.1 micron
    [row,col] = find(distances<=0);
    distances(row,:)=10^(-4);

    % Find the distribution of lengths of the interior crystals
    intcrystals = imclearborder(BW); % remove crystals on edges for
    % analysis
    [intL,intnum] = bwlabel(intcrystals);
    intstats = regionprops(intL,'MajorAxisLength');
    lengths = (cat(1,intstats.MajorAxisLength)); % crystal lengths in
    % px
    lengths = lengths./scale; % crystal lengths in mm

    % Find crystal-free area
    [m,n] = size(BW); % image dimensions in px
    totalarea = m*n; % image size in px^2
    xtalarea = bwarea(BW); % area of crystals in px^2
    porearea(name) = totalarea-xtalarea; % area of pore space in the
    % image (includes area taken up by bubbles), in px^2

    % Update value for total number of crystals counted
    numxtals = max(labels);

    % Final outputs
    porewidths = cat(1,porewidths,distances); % pore diameters in mm
    crystallengths = cat(1,crystallengths,lengths); % lengths of the
    % interior crystals in all images (mm)
    % Note: crystal lengths are not in positions corresponding to their
    % labels on the figures since crystals on edges are excluded from
    % crystallengths.
    porespace(name) = porearea(name)/totalarea; % fraction of area that
    % is pore space (non-xtals)
    porearea(name) = porearea(name)/(scale^2); % total area of pore
    % space in mm^2
    close all
    clearvars -except files numxtals porewidths porearea porespace name
    crystallengths
end

clearvars name numxtals

poreradii = porewidths./2;


%% BUBBLE SIZE DISTRIBUTION

numbubbles = 0; % Number of labels already used for labeling bubbles
bubbleradii = []; % Vector containing equivalent radii for all interior
% bubbles in all images (cumulative)
```

```
bubblearea = zeros(length(files),1); % this vector will get filled in
% the bubble size distribution loop

for name = 1:length(files)

    % Import image and extract bubbles
    image = imread(files{name,1});
    % imshow(image)
    level = graythresh(image);
    all = im2bw(image,level); % keeps both bubbles and crystals
    crystals = im2bw(image,0.55); % keeps only crystals
    bubbles = crystals-all; % bubbles with noise; object pixels = 1,
    % background pixels = 0

    % Remove noise by eroding and dilating
    SE = strel('square',2); % creates a square structuring element with
    % width 2 px
    bubbles = imerode(bubbles,SE);
    bubbles = imdilate(bubbles,SE);

    % Show image (inverted = visally more intuitive)
    figure('Name','bubbles','NumberTitle','off')
    imshow(~bubbles)

    % Remove bubbles on edges for analysis
    intbubbles = imclearborder(bubbles);
    figure('Name','bubbles not on edges','NumberTitle','off')
    imshow(~intbubbles)
    hold on

    % Find the sizes and centroids (center of mass) of the interior
    % bubbles
    [L,num] = bwlabel(intbubbles);
    stats = regionprops(L,'Area','Centroid','EquivDiameter'); % area in
    % pixels; centroid as x and y coordinate
    labels = (1:num)';
    labels = labels+numbubbles; % Number objects cumulatively on all
    % images
    centroids = cat(1,stats.Centroid); % coordinates of the centroids
    bubblesizes = (cat(1,stats.EquivDiameter))./2; % equivalent radii
    % in px

    % Plot the centroids and object numbers on the image and save it
    plot(centroids(:,1),centroids(:,2),'g.')
    hold on
    for count=1:num
        text(centroids(count,1),centroids(count,2),sprintf('\t\t\t%g',
        labels(count,1)),'Color','g','FontSize',12,'FontWeight','b',
        'HorizontalAlignment','left')
    end
    hold on
    filename = files{name,1};
    truncate = regexp(filename,'composite');
    uimagename = filename(1:truncate-1);
    text(5,15,sprintf('%s\t\t%s',uimagename,'bubbles'),'Color','g')
    hold on
    input('Please save this image and then hit return');
```

```
    % Find total area taken up by bubbles
    bubblearea(name) = bwarea(bubbles); % area of bubbles in px^2,
    % includes bubbles on edges

    % Convert sizes to mm; get image scale from user (can get in
    % Photoshop > Image > Image Size...
    scale = input('Enter scale of image in px/mm (default is 153.7292
    px/mm)');
    if isempty(scale)
        scale = 153.7292; % px/mm
    end
    bubblesizes = bubblesizes./scale; % equivalent radii in mm

    % Update value for total number of bubbles counted (bubbles on
    % edges excluded)
    numbubbles = max(labels);

    % Final loop outputs
    bubbleradii = cat(1,bubbleradii,bubblesizes); % bubbles are in
    % order in which they are labeled on images (cumulatively)
    bubblearea(name) = bubblearea(name)/(scale^2); % total area of
    % bubbles (including on edges) in mm^2
    close all
    clearvars -except files numbubbles bubbleradii bubblearea name
    porewidths poreradii porearea porespace crystallengths
end

clearvars name numbubbles

% Find crystal-free vesicularity
bubblespace = bubblearea./porearea; % fraction of pore space that is
% taken up by bubbles in each image (in order in text file)
bubblespaceavg = mean(bubblespace); % average vesicularity of all
% images


%% Output plots

% PORE SIZE DISTRIBUTION

% Show histogram of the pore size distribution
bins = (0.025):(0.05):(max(poreradii)+0.025); % centers of bins used
for plotting histogram
figure('Name','Pore size distribution','NumberTitle','off')
[n,xout] = hist(poreradii,bins);
npercent = (n.*100)./length(poreradii);
bar(xout,npercent)
xlabel('pore radius (mm)','FontSize',18)
ylabel('frequency (%)','FontSize',18)
xlim([0 1.5])
set(gca,'FontSize',16,'LineWidth',1.5)
axis square
box off
```

```
% CRYSTAL SIZE DISTRIBUTION

% Show histogram of the crystal size distribution
bins2 = (0.025):(0.05):(max(crystallengths)+0.025); % centers of bins
figure('Name','Crystal size distribution','NumberTitle','off')
[n2,xout2] = hist(crystallengths,bins2);
npercent2 = (n2.*100)./length(crystallengths);
bar(xout2,npercent2)
xlabel('crystal length (mm)','FontSize',18)
ylabel('frequency (%)','FontSize',18)
set(gca,'FontSize',16,'LineWidth',1.5)
axis square
box off


% BUBBLE SIZE DISTRIBUTION

% Show histogram of bubble size distribution
bins3 = (0.025):(0.05):(max(bubbleradii)+0.025); % centers of bins
figure('Name','Bubble size distribution','NumberTitle','off')
[n3,xout3] = hist(bubbleradii,bins3);
npercent3 = (n3.*100)./length(bubbleradii);
bar(xout3,npercent3)
xlabel('bubble equivalent radius (mm)','FontSize',18)
ylabel('frequency (%)','FontSize',18)
xlim([0 1.5])
set(gca,'FontSize',16,'LineWidth',1.5)
axis square
box off


%% Save the output variables

save('image_distances_output')
% You can reload the results by typing "load
% image_distances_output.mat" in the command window
```

APPENDIX C

MATLAB® MODEL FOR BUBBLE RISE THROUGH POROUS MEDIA

The code used to calculate velocities through crystal-rich magma at Stromboli volcano in Chapter IV is given below. A discussion of the model can be found in Chapter IV, section 4.2. Parameters in the code are from Table 4.5. This script was coded in MATLAB® version R2010b (The MathWorks, Natick, MA, USA) on a Macintosh computer.

```
% Name:     capillary_vertical_empirical_new.m
% Author:   Isolde Belien
% Date:     May 2011
% Goal:     Model the velocity of a bubble rising through a porous
% medium, modeled as a network of vertical tubes


%% Import variables

load image_distances_output.mat % output from code image_distances.m

% This file contains the variables:
%     - porewidths: all pore widths from all images (mm)
%       Widths are calculated as the distances between the crystal
%       centroids reduced by the crystal equivalent radii. Since
%       crystals are in reality non-spherical, widths can end up
%       negative. We set all widths that are =< 0 to 0.1 micron
%     - poreradii: porewidths/2
%     - porearea: crystal-free area in each image, in order listed in
%       filelist.txt (mm^2)
%     - porespace: porearea expressed as a fraction of the total image
%       area, order cf. filelist.txt (fraction)
%     - crystallengths: major axis lengths of the interior crystals in
%       all images (mm)
%     - bubbleradii: equivalent radii of all interior bubbles (not on
%       edges) in all images, cumulatively ordered as labeled on the
%       images (mm)
%     - bubblearea: total area of bubbles (including ones on edges) in
%       each image, in order listed in filelist.txt (mm^2)
%     - bubblespace: fraction of pore space that is taken up by bubbles
%       in each image, order cf. filelist.txt (fraction)
%     - bubblespaceavg: average value of bubblespace in all images
%       (fraction)
%     - mean of the probability density function fit to the histograms
%       (exponential for both distributions)
```

```
g = 9.81; % acceleration of gravity (m/s2)
rho = 2690; % Stromboli magma density (kg/m3) - (see Belien et al.
% (2010) for references)
mu = 330; % Stromboli magma liquid viscosity (Pa s)
sigma = 0.25; % surface tension (N/m) (range 0.1-0.4 at Stromboli)
thickness = 10; % total thickness of the porous medium (m)
Requivcount = 1;
Requivvalues = [0:(0.01*(10^(-3))):(0.1*(10^(-3))) (0.2*(10^(-
3))):(0.1*(10^(-3))):(1*(10^(-3)))]; % in m
M = zeros(length(Requivvalues),1);
Mean = zeros(length(Requivvalues),1);


%% Simulation

for index = 1:length(Requivvalues)
    Requiv = Requivvalues(index); % bubble equivalent radius in m
    numsim = 100; % number of simulations

    % Preallocate memory
    average_velocity = zeros(numsim,1);

        for sim = 1:1:numsim

            sprintf('%s%g','Simulation # ',sim)
            position = 0; % height of the bubble on entering each new
            % tube (m)
            time = 0; % time of entry into base of each tube (s)
            count = 1;

            while position<thickness % as long as the bubble hasn't
            % reached the top of the porous medium

                % Randomly select R, L and Requiv from the
                % distributions generated in image_distances.m
                poreindex = randperm(numel(poreradii));
                R = poreradii(poreindex(1)); % tube radius (mm)
                xtalindex = randperm(numel(crystallengths));
                L = crystallengths(xtalindex(1)); % tube length (mm)

                % Convert input to m
                R = R/1000;
                L = L/1000;

                if Requiv/R<0.45
                    Ububble = ((Requiv^2)*rho*g)/(3*mu); % Stokes
                    % velocity (Hadamard-Rybczynski modification for
                    % viscous liquids) (m/s)
                else
                    Re_buoyancy = ((((2*R)^3)*g*(rho^2))^(1/2))/mu; %
                    % buoyancy Reynolds #
                    if Re_buoyancy>=10
                        warning('The buoyancy Reynolds number is too
                        large')
```

```
                    Ububble = -1;
                    break
                else
                    Eo = (g*rho*((2*R)^2))/sigma; % Bond number
                    % From Viana et al. (2003)
                    Frclosed = ((9.494*(10^(-
                    3)))/(1+(6197/(Eo^2.561)))^0.5793)*(Re_buoyancy
                    ^1.026); % dimensionless velocity
                    Uclosed = Frclosed*((g*2*R)^(1/2)); % velocity
                    % in a sealed tube (m/s)
                    % Empirical relationship between U/Uclosed and
                    % Requiv/R
                    Ububble =
                    Uclosed*0.216*(exp(2.1198*(Requiv/R))); %
                    % bubble velocity in fully submerged tube (m/s)
                end
            end

            time = time+(L/Ububble); % total time the bubble has
            % been in the tube network (s)
            position = position+L; % height of the bubble when it
            % reaches the top of the tube (m)
            count = count+1;

        end

        if Ububble == -1;
            average_velocity(sim) = -1;
        else
            average_velocity(sim) = position/time; % average
            % velocity for each simulation (m/s)
        end

    end

    average_velocity = average_velocity*60*60*24; % average velocities
    % in m/day
    M(Requivcount) = median(average_velocity); % in m/day
    sprintf('%s%g%s%g%s','The median velocity of a bubble with
    equivalent radius ',Requiv*1000,' mm is ',M(Requivcount),' m/day')
    Mean(Requivcount) = mean(average_velocity); % in m/day
    sprintf('%s%g%s%g%s','The mean velocity of a bubble with equivalent
    radius ',Requiv*1000,' mm is ',Mean(Requivcount),' m/day')

    Requivcount = Requivcount+1;

end

figure
semilogy(Requivvalues*1000,M)
xlabel('bubble equivalent radius (mm)','FontSize',18)
ylabel('median velocity (m/day)','FontSize',18)
set(gca,'FontSize',16,'LineWidth',1.5)
axis square

figure
```

```
semilogy(Requivvalues*1000,Mean)
xlabel('bubble equivalent radius (mm)','FontSize',18)
ylabel('mean velocity (m/day)','FontSize',18)
set(gca,'FontSize',16,'LineWidth',1.5)
axis square
```

REFERENCES CITED

Abramoff, M.D., Magelhaes, P.J., Ram, S.J., 2004. Image Processing with ImageJ. Biophoton. Int. 11 (7), 36-42.

Aiuppa, A., Bertagnini, A., Métrich, N., Moretti, R., Di Muro, A., Liuzzo, M., Tamburello, G., 2010. A model of degassing for Stromboli volcano. Earth Planet. Sci. Lett. 295, 195-204.

Allard, P., Carbonnelle, J., Métrich, N., Loyer, H., Zettwoog, P., 1994. Sulfur output and magma degassing budget of Stromboli volcano. Nature 368, 326-330.

Andronico, D., Scollo, S., Caruso, S., Cristaldi, A., 2008. The 2002-03 Etna explosive activity: tephra dispersal and features of the deposits. J. Geophys. Res. 113, B04209. doi:10.1029/2007JB005126.

Andronico, D., Cristaldi, A., Del Carlo, P., Taddeucci, J., 2009. Shifting styles of basaltic explosive activity during the 2002-03 eruption of Mt. Etna, Italy. J. Volcanol. Geoth. Res. 180, 110-122.

Angeli, P., Hewitt, G.F., 2000. Flow structure in horizontal oil-water flow. Int. J. Multiphase Flow 26, 1117-1140.

Armienti, P., Francalanci, L., Landi, P., 2007. Textural effects of steady state behaviour of the Stromboli feeding system. J. Volcanol. Geoth. Res. 160, 86-98.

Arrighi, S., Principe, C., Rosi, M., 2001. Violent Strombolian and Subplinian eruptions at Vesuvius during post-1631 activity. Bull. Volcanol. 63, 126-150.

Asimow, P.D., Ghiorso, M.S., 1998. Algorithmic modifications extending MELTS to calculate subsolidus phase relations. Am. Mineral. 83, 1127-1131.

Aslan, M.M., Crofcheck, C., Tao, D., Mengüç, M.P., 2006. Evaluation of micro-bubble size and gas hold-up in two-phase gas-liquid columns via scattered light measurements. J. Quant. Spectrosc. Radiative Transf. 101, 527-539.

Bagdassarov, N., Dorfman, A., Dingwell, D.B., 2000. Effect of alkalis, phosphorus, and water on the surface tension of haplogranite melt. Am. Mineral. 85, 33-40.

Belien, I.B., Cashman, K.V., Rempel, A.W., 2010. Gas accumulation in particle-rich suspensions and implications for bubble populations in crystal-rich magma. Earth Planet. Sci. Lett. 297, 133-140.

Bendiksen, K.H., 1985. On the motion of long bubbles in vertical tubes. Int. J. Multiphase Flow 11 (6), 797-812.

Bendiksen, K.H., Maines, D., Moe, R., Nuland, S., 1991. The dynamic two-fluid model OLGA: theory and application. SPE Prod. Eng. 6 (2), 171-180.

Bertagnini, A., Métrich, N., Landi, P., Rosi, M., 2003. Stromboli volcano (Aeolian Archipelago, Italy): An open window on the deep-feeding system of a steady state basaltic volcano. J. Geophys. Res. 108 (B7), 2336. doi:10.1029/2002JB002146.

Bertagnini, A., Métrich, N., Francalanci, L., Landi, P., Tommasini, S., Conticelli, S., 2008. Volcanology and magma geochemistry of the present-day activity: constraints on the feeding system. In: Calvari, S., Inguaggiato, S., Puglisi, G., Ripepe, M., Rosi, M. (Eds.), The Stromboli volcano: An integrated study of the 2002-2003 eruption: AGU Geophysical Monograph Series, Washington D.C., 182, pp. 19-37.

Blackburn, E.A., Wilson, L., Sparks, R.S.J., 1976. Mechanisms and dynamics of Strombolian activity. J. Geol. Soc. London 132, 429-440.

Blower, J.D., Keating, J.P., Mader, H.M., Phillips, J.C., 2001. Inferring volcanic degassing processes from vesicle size distributions. Geophys. Res. Lett. 28 (2), 347-350.

Blower, J.D., Keating, J.P., Mader, H.M., Phillips, J.C., 2002. The evolution of bubble size distributions in volcanic eruptions. J. Volcanol. Geoth. Res. 120, 1-23.

Bretherton, F.P., 1961. The motion of long bubbles in tubes. J. Fluid Mech. 10, 166-188.

Brown, R.A.S., 1965. The mechanics of large gas bubbles in tubes – I. bubble velocities in stagnant liquids. Can. J. Chem. Eng. 43 (5), 217-223.

Burton, M.R., Mader, H.M., Polacci, M., 2007. The role of gas percolation in quiescent degassing of persistently active basaltic volcanoes. Earth Planet. Sci. Lett. 264, 46-60.

Burton, M., Allard, P., Muré, F., La Spina, A., 2007b. Magmatic gas composition reveals the source depth of slug-driven Strombolian explosive activity. Science 317, 227-230.

Caricchi, L., Burlini, L., Ulmer, P., Gerya, T., Vassalli, M., Papale, P., 2007. Non-newtonian rheology of crystal-bearing magmas and implications for magma ascent dynamics. Earth Planet. Sci. Lett. 264, 402-419.

Cashman, K.V., Mangan, M.T., Newman, S., 1994. Surface degassing and modifications to vesicle size distributions in active basalt flows. J. Volcanol. Geoth. Res. 61, 45-68.

Cashman, K.V., Kauahikaua, J.P., 1997. Reevaluation of vesicle distributions in basaltic lava flows. Geology 25, 419-422.

Cashman, K.V., McConnell, S.M., 2005. Multiple levels of magma storage during the 1980 summer eruptions of Mount St. Helens, WA. Bull. Volcanol. 68, 57-75.

Chadwick, W.W., Jr., Cashman, K.V., Embley, R.W., Matsumoto, H., Dziak, R.P., de Ronde, C.E.J., Lau, T.K., Deardorff, N.D., Merle, S.G., 2008. Direct video and hydrophone observations of submarine explosive eruptions at NW Rota-1 volcano, Mariana arc. J. Geophys. Res. 113, B08S10. doi:10.1029/2007JB005215.

Champallier, R., Bystricky, M., Arbaret, L., 2008. Experimental investigation of magma rheology at 300 MPa: from pure hydrous melt to 76 vol.% of crystals. Earth Planet. Sci. Lett. 267 (3-4), 571-583.

Chouet, B., Hamisevicz, N., McGetchin, T.R., 1974. Photoballistics of volcanic jet activity at Stromboli, Italy. J. Geophys. Res. 79 (32), 4961-4976.

Chouet, B., Dawson, P., Ohminato, T., Martini, M., Saccorotti, G., Giudicepietro, F., De Luca, G., Milana, G., Scarpa, R., 2003. Source mechanisms of explosions at Stromboli volcano, Italy, determined from moment-tensor inversions of very-long-period data. J. Geophys. Res. 108 (B1), 2019. doi:10.1029/2002JB001919.

Cigolini, C., Laiolo, M., Bertolino, S., 2008. Probing Stromboli volcano from the mantle to paroxysmal eruptions. In: Annen, C., Zellmer, G.F. (Eds.), Dynamics of Crustal Magma Transfer, Storage and Differentiation: Geological Society, London, Special Publications, 304, pp. 33-70.

Clift, R., Grace, J.R., Weber, M.E., 1978. Bubbles, Drops, and Particles: Academic Press, New York.

Colò, L., Ripepe, M., Baker, D.R., Polacci, M., 2010. Magma vesiculation and infrasonic activity at Stromboli open conduit volcano. Earth Planet. Sci. Lett. 292, 274-280.

Costa, A., 2005. Viscosity of high crystal content melts: dependence on solid fraction. Geophys. Res. Lett. 32, L22308. doi:10.1029/2005GL024303.

Costa, A., Blake, S., Self, S., 2006. Segregation processes in vesiculating crystallizing magmas. J. Volcanol. Geoth. Res. 153, 287-300.

Di Traglia, F., Cimarelli, C., de Rita, D., Gimeno Torrente, D., 2009. Changing eruptive styles in basaltic explosive volcanism: examples from Croscat complex scoria cone, Garrotxa volcanic field (NE Iberian Peninsula). J. Volcanol. Geoth. Res. 180, 89-109.

Divoux, T., Vidal, V., Ripepe, M., Géminard, J.-C., 2011. Influence of non-Newtonian rheology on magma degassing. Geophys. Res. Lett. 38, L12301. doi: 10.1029/2011GL047789.

D'Oriano, C., Bertagnini, A., Pompilio, M., 2010. Ash erupted during normal activity at Stromboli (Aeolian Islands, Italy) raises questions on how the feeding system works. Bull. Volcanol. 73 (5), 471-477.

D'Oriano, C., Cioni, R., Bertagnini, A, Andronico, D., Cole, P.D., 2010b. Dynamics of ash-dominated eruptions at Vesuvius: the post-512 AD AS1a event. Bull. Volcanol. 73 (6), 699-715. doi:10.1007/s00445-010-0432-1.

Dumitrescu, D.T., 1943. Strömung an einer Luftblase im senkrechten Rohr. Zeit. Angew. Math. Mech. 23 (3), 139-149.

Eaton, B.A., Knowles, C.R., Silberberg, I.H., 1967. The prediction of flow patterns, liquid holdup and pressure losses occurring during continuous two-phase flow in horizontal pipelines. J. Petrol. Tech. 19 (6), 815-828.

Edmonds, M., 2008. New geochemical insights into volcanic degassing. Phil. Trans. Royal Soc. London A 366, 4559-4579.

Feng, J.Q., 2008. Buoyancy-driven motion of a gas bubble through viscous liquid in a round tube. J. Fluid Mech. 609, 377-410.

Fornaciai, A., Bisson, M., Landi, P., Mazzarini, F., Pareschi, M.T., 2010. A LiDAR survey of Stromboli volcano (Italy): digital elevation model-based geomorphology and intensity analysis. Int. J. Remote Sens. 31 (12), 3177-3194.

Francalanci, L., Tommasini, S., Conticelli, S., Davies, G.R., 1999. Sr isotope evidence for short magma residence time for the 20th century activity at Stromboli volcano, Italy. Earth Planet. Sci. Lett. 167, 61-69.

Fritz, W., 1935. Berechnung des maximale Volume von Dampfblasen. Physik. Zeit. 36, 379-384.

Ghiorso, M.S., Sack, R.O., 1995. Chemical mass transfer in magmatic processes. IV. a revised and internally consistent thermodynamic model for the interpolation and extrapolation of liquid-solid equilibria in magmatic systems at elevated temperatures and pressures. Contrib. Mineral. Petrol. 119, 197-212.

Gualda, G.A.R., Cook, D.L., Chopra, R., Qin, L., Anderson, A.T., Rivers, M., 2004. Fragmentation, nucleation and migration of crystals and bubbles in the Bishop Tuff rhyolitic magma. Trans. Royal Soc. Edinburgh: Earth Sci. 95, 375-390.

Gurioli, L., Harris, A.J.L., Houghton, B.F., Polacci, M., Ripepe, M., 2008. Textural and geophysical characterization of explosive basaltic activity at Villarrica volcano. J. Geophys. Res. 113, B08206. doi:10.1029/2007JB005328.

Hantschel, T., Kauerauf, A.I., 2009. Fundamentals of Basin and Petroleum Systems Modeling: Springer-Verlag, Berlin, Heidelberg.

Harmathy, T.Z., 1960. Velocity of large drops and bubbles in media of infinite or restricted extent. Am. Inst. Chem. Eng. J. 6 (2), 281-288.

Harris, A., Ripepe, M., 2007. Temperature and dynamics of degassing at Stromboli. J. Geophys. Res. 112, B03205. doi:10.1029/2006JB004393.

Harris, A., Ripepe, M., 2007b. Synergy of multiple geophysical approaches to unravel explosive eruption conduit and source dynamics – a case study from Stromboli. Chem. Erde 67, 1-35.

Houghton, B.F., Gonnermann, H.M., 2008. Basaltic explosive volcanism: constraints from deposits and models. Chem. Erde 68, 117-140.

Ishibashi, H., Sato, H., 2007. Viscosity measurements of subliquidus magmas: alkali olivine basalt from the Higashi-Matsuura district, southwest Japan. J. Volcanol. Geoth. Res. 160, 223-238.

Jaupart, C., Vergniolle, S., 1988. Laboratory models of Hawaiian and Strombolian eruptions. Nature 331, 58-60.

Jaupart, C., Vergniolle, S., 1989. The generation and collapse of a foam layer at the roof of a basaltic magma chamber. J. Fluid Mech. 203, 347-380.

Jeffrey, D.J., Acrivos, A., 1976. The rheological properties of suspensions of rigid particles. Am. Inst. Chem. Eng. J. 22 (3), 417-432.

Ji, S., 2004. A generalized mixture rule for estimating the viscosity of solid-liquid suspensions and mechanical properties of polyphase rocks and composite materials. J. Geophys. Res. 109, B10207. doi:10.1029/2004JB003124.

Johnson, J.B., 2005. Source location variability and volcanic vent mapping with a small-aperture infrasound array at Stromboli volcano, Italy. Bull. Volcanol. 67,1-14.

Kang, C.-W., Quan, S., Lou, J., 2010. Numerical study of a Taylor bubble rising in stagnant liquids. Phys. Review E 81, 066308 1-11.

Khitarov, N.I., Lebedev, Ye.B., Dorfman, A.M., Bagdasarov, N.Sh., 1979. Effects of temperature, pressure, and volatiles on the surface tension of molten basalt. Geochem. Int. 16 (5), 78-86.

Klug, C., Cashman, K.V., Bacon, C.R., 2002. Structure and physical characteristics of pumice from the climactic eruption of Mount Mazama (Crater Lake), Oregon. Bull. Volcanol. 64, 486-501.

Krieger, I.M., Dougherty, T.J., 1959. A mechanism for non-newtonian flow in suspensions of rigid spheres. Trans. Soc. Rheol. 3, 137-152.

Krishna, R., Urseanu, M.I., van Baten, J.M., Ellenberger, J., 1999. Influence of scale on the hydrodynamics of bubble columns operating in the churn-turbulent regime: experiments vs. Eulerian simulations. Chem. Eng. Sci. 54, 4903-4911.

Landi, P., Métrich, N., Bertagnini, A., Rosi, M., 2004. Dynamics of magma mixing and degassing recorded in plagioclase at Stromboli (Aeolian Archipelago, Italy). Contrib. Mineral. Petrol. 147, 213-227.

Landi, P., Métrich, N., Bertagnini, A., Rosi, M., 2008. Recycling and "re-hydration" of degassed magma inducing transient dissolution/crystallization events at Stromboli (Italy). J. Volcanol. Geoth. Res. 174. doi:10.1016/j.jvolgeores.2008.02.013.

Landi, P., Marchetti, E., La Felice, S., Ripepe, M., Rosi, M., 2011. Integrated petrochemical and geophysical data reveals thermal distribution of the feeding conduits at Stromboli volcano, Italy. Geophys. Res. Lett. 38, L08305. doi: 10.1029/2010GL046296.

Lautze, N.C., Houghton, B.F., 2006. Linking variable explosion style and magma textures during 2002 at Stromboli volcano, Italy. Bull. Volcanol. 69. doi:10.1007/s00445-006-0086-1.

Lejeune, A.M., Richet, P., 1995. Rheology of crystal-bearing silicate melts: an experimental study at high viscosities. J. Geophys. Res. 100 (B3), 4215-4229.

Liu, H., Vandu, C.O., Krishna, R., 2005. Hydrodynamics of Taylor flow in vertical capillaries: flow regimes, bubble rise velocity, liquid slug length, and pressure drop. Ind. Eng. Chem. Res. 44, 4884-4897.

Llewellin, E.W., Mader, H.M., Wilson, S.D.R., 2002. The rheology of a bubbly liquid. Proc. Royal Soc. London A 458, 987-1016. doi:10.1098/rspa.2001.0924.

Lucas, D., Krepper, E., Prasser, H.-M., 2005. Development of co-current air-water flow in a vertical pipe. Int. J. Multiphase Flow 31, 1304-1328.

Mangan, M.T., Cashman, K.V., Newman, S., 1993. Vesiculation of basaltic magma during eruption. Geology 21, 157-160.

Mangan, M., Sisson, T., 2005. Evolution of melt-vapor surface tension in silicic volcanic systems: Experiments with hydrous melts. J. Geophys. Res. 110, B01202. doi:10.1029/2004JB003215.

Marchessault, R.N., Mason, S.G., 1960. Flow of entrapped bubbles through a capillary. Ind. Eng. Chem. 52 (1), 79-84.

Marchetti, E., Ripepe, M., 2005. Stability of the seismic source during effusive and explosive activity at Stromboli volcano. Geophys. Res. Lett. 32, L03307. doi:10.1029/2004GL021406.

Marsh, B.D., 1981. On the crystallinity, probability of occurrence, and rheology of lava and magma. Contrib. Mineral. Petrol. 78, 85-98.

Mastin, L.G., 1997. Evidence for water influx from a caldera lake during the explosive hydromagmatic eruption of 1790, Kilauea volcano, Hawaii. J. Geophys. Res. 102 (B9), 20093-20109.

Mastin, L.G., Christiansen, R.L., Thornber, C., Lowenstern, J., Beeson, M., 2004. What makes hydromagmatic eruptions violent? Some insights from the Keanakako'i ash, Kīlauea Volcano, Hawai'i. J. Volcanol. Geoth. Res. 137, 15-31.

Mastin, L.G., Roeloffs, E., Beeler, N.M., Quick, J.E., 2008. Constraints on the size, overpressure, and volatile content of the Mount St. Helens magma system from geodetic and dome-growth measurements during the 2004-2006+ eruption. In: Sherrod, D.R., Scott, W.E., Stauffer, P.H. (Eds.), A volcano rekindled: The renewed eruption of Mount St. Helens, 2004-2006: USGS Professional Paper 1750.

McGreger, A.D., Lees, J.M., 2004. Vent discrimination at Stromboli volcano, Italy. J. Volcanol. Geoth. Res. 137, 169-185.

Mena, P.C., Ruzicka, M.C., Rocha, F.A., Teixeira, J.A., Drahos, J., 2005. Effect of solids on homogeneous-heterogeneous flow regime transition in bubble columns. Chem. Eng. Sci. 60, 6013-6026.

Métrich, N., Bertagnini, A., Landi, P., Rosi, M., 2001. Crystallization driven by decompression and water loss at Stromboli volcano (Aeolian Islands, Italy). J. Petrol. 42 (8), 1471-1490.

Mori, T., Burton, M., 2009. Quantification of the gas mass emitted during single explosions on Stromboli with the SO_2 imaging camera. J. Volcanol. Geoth. Res. 188, 395-400.

Mudde, R.F., 2005. Gravity-driven bubbly flows. Ann. Rev. Fluid Mech. 37, 393-423.

Namiki, A., Manga, M., 2008. Transition between fragmentation and permeable outgassing of low viscosity magmas. J. Volcanol. Geoth. Res. 169, 48-60.

Oddie, G., Pearson, J.R.A., 2004. Flow-rate measurement in two-phase flow. Ann. Rev. Fluid Mech. 36, 149-172.

Oguz, H.N., Prosperetti, A., 1993. Dynamics of bubble growth and detachment from a needle. J. Fluid Mech. 257, 111-145.

Olbricht, W.L., 1996. Pore-scale prototypes of multiphase flow in porous media. Ann. Rev. Fluid Mech. 28,187-213.

Parfitt, E.A., Wilson, L., 1995. Explosive volcanic eruptions – IX. The transition between Hawaiian-style lava fountaining and Strombolian explosive activity. Geophys. J. Int. 121, 226-232.

Parfitt, E.A., 2004. A discussion of the mechanisms of explosive basaltic eruptions. J. Volcanol. Geoth. Res. 134, 77-107.

Pioli, L., Erlund, E., Johnson, E., Cashman, K., Wallace, P., Rosi, M., Delgado Granados, H., 2008. Explosive dynamics of violent Strombolian eruptions: the eruption of Parícutin Volcano 1943-1952 (Mexico). Earth Planet. Sci. Lett. 271, 359-368.

Polacci, M., Baker, D.R., Mancini, L., Tromba, G., Zanini, F., 2006a. Three-dimensional investigation of volcanic tectures by X-ray microtomography and implications for conduit processes. Geophys. Res. Lett. 33, L13312. doi:10.1029/2006GL026241.

Polacci, M., Corsaro, R.A., Andronico, D., 2006b. Coupled textural and compositional characterization of basaltic scoria: insights into the transition from Strombolian to fire fountain activity at Mount Etna, Italy. Geology 34 (3), 201-204.

Polacci, M., Baker, D.R., Bai, L., Mancini, L., 2008. Large vesicles record pathways of degassing at basaltic volcanoes. Bull. Volcanol. 70 (9), 1023-1029.

Polacci, M., Baker, D.R., Mancini, L., Favretto, S., Hill, R.J., 2009. Vesiculation in magmas from Stromboli and implications for normal Strombolian activity and paroxysmal explosions in basaltic systems. J. Geophys. Res. 114, B01206. doi:10.1029/2008JB005672.

Ripepe, M., Harris, A.J.L., Carniel, R., 2002. Thermal, seismic and infrasonic evidences of variable degassing rates at Stromboli volcano. J. Volcanol. Geoth. Res. 118, 285-297.

Ripepe, M., Marchetti, E., 2002. Array tracking of infrasonic sources at Stromboli volcano. Geophys. Res. Lett. 29 (22), 2076. doi:10.1029/2002GL015452.

Ripepe, M., Marchetti, E., Ulivieri, G., 2007. Infrasonic monitoring at Stromboli volcano during the 2003 effusive eruption: Insights on the explosive and degassing process of an open conduit system. J. Geophys. Res. 112, B09207. doi:10.1029/2006JB004613.

Ripepe, M., Delle Donne, D., Harris, A., Marchetti, E, Ulivieri, G., 2008. Dynamics of Strombolian activity. In: Calvari, S., Inguaggiato, S., Puglisi, G., Ripepe, M., Rosi, M. (Eds.), The Stromboli volcano: An integrated study of the 2002-2003 eruption: AGU Geophysical Monograph Series, Washington D.C., 182, pp. 39-48.

Roosevelt, S.E., Corapcioglu, M.Y., 1998. Air bubble migration in a granular porous medium: experimental studies. Water Resources Res. 34 (5), 1131-1142.

Roscoe, R., 1952. The viscosity of suspensions of rigid spheres. Brit. J. Appl. Phys. 3, 267-269.

Saar, M.O., Manga, M., Cashman K.V., Fremouw, S., 2001. Numerical models of the onset of yield strength in crystal-melt suspensions. Earth Planet. Sci. Lett. 187, 367-379.

Sanyal, J., Vásquez, S., Roy, S., Dudukovic, M.P., 1999. Numerical simulation of gas-liquid dynamics in cylindrical bubble column reactors. Chem. Eng. Sci. 54, 5071-5083.

Shaw, H.R., 1972. Viscosities of magmatic silicate liquids: an empirical method of prediction. Am. J. Sci. 272, 870-893.

Shimano, T., Nakada, S., 2006. Vesiculation path of ascending magma in the 1983 and the 2000 eruptions of Miyakejima volcano, Japan. Bull. Volcanol. 68, 549-566.

Sparks, R.S.J., 2003. Dynamics of magma degassing. Geol. Soc. London Special Publications 213, 5-22.

Spera, F.J. (2000). Physical properties of magma. In: Encyclopedia of Volcanoes, Ed.-in-Chief: H. Sigurdsson, Academic Press, 171-190.

Stark, J. and Manga, M., 2000. The motion of long bubbles in a network of tubes. Transp. Porous Med. 40, 201-218.

Streck, M.J., Dungan, M.A., Bussy, F., Malavassi, E., 2005. Mineral inventory of continuously erupting basaltic andesites at Arenal volcano, Costa Rica: implications for interpreting monotonous, crystal-rich, mafic arc stratigraphies. J. Volcanol. Geoth. Res. 140, 133-155.

Suckale, J., Hager, B.H., Elkins-Tanton, L.T., Nave, J.-C., 2010. It takes three to tango: 2. Bubble dynamics in basaltic volcanoes and ramifications for modeling normal Strombolian activity. J. Geophys. Res. 115, B07410. doi:10.1029/2009JB006917.

Taha, T., Cui, Z.F., 2004. Hydrodynamics of slug flow inside capillaries. Chem. Eng. Sci. 59, 1181-1190.

Toramaru, A., 1989. Vesiculation process and bubble size distributions in ascending magmas with constant velocities. J. Geophys. Res. 94 (B12), 17523-17542.

Toramaru, A., 1990. Measurement of bubble size distributions in vesiculated rocks with implications for quantitative estimation of eruption processes. J. Volcanol. Geoth. Res. 43, 71-90.

Tung, K.W., Parlange, J.Y., 1976. Note on the motion of long bubbles in closed tubes – influence of surface tension. Acta Mech. 24, 313-317.

Vergniolle, S. and Mangan, M. (2000). Hawaiian and Strombolian eruptions. In: Encyclopedia of Volcanoes, Ed.-in-Chief: H. Sigurdsson, Academic Press, 447-461.

Vetere, F., Behrens, H., Holtz, F., Vilardo, G., Ventura, G., 2010. Viscosity of crystal-bearing melts and its implication for magma ascent. J. Mineral. Petrol. Sci. 105, 151-163.

Viana, F., Pardo, R., Yánez, R., Trallero, J.L., Joseph, D.D., 2003. Universal correlation for the rise velocity of long gas bubbles in round pipes. J. Fluid Mech. 494, 379-398.

Vona, A., Romano, C., Dingwell, D.B., Giordano, D., 2011. The rheology of crystal-bearing basaltic magmas from Stromboli and Etna. Geochim. Cosmochim. Acta 75, 3214-3236.

Wallace, P. and Anderson, A.T. (2000). Volatiles in magmas. In: Encyclopedia of Volcanoes, Ed.-in-Chief: H. Sigurdsson, Academic Press, 149-170.

Wallis, G.B., 1969. One-Dimensional Two-Phase Flow: McGraw Hill, New York.

Walsh, S.D.C., Saar M.O., 2008. Numerical models of stiffness and yield stress growth in crystal-melt suspensions. Earth Planet. Sci. Lett. 267, 32-44.

Web reference: http://www.ct.ingv.it/stromboli2007/main.htm (description of activity per day (in Italian), accessed 5 January 2010)

Web reference: www.dow.com (fluid properties of glycerin)

Wooding, R.A., Morel-Seytoux, H.J., 1976. Multiphase fluid flow through porous media. Ann. Rev. Fluid Mech. 8, 233-274.